Factors affecting Capacity Retention in Hybrid Lithium-Sulfur Battery

Zur Erlangung des akademischen Grades
eines

Doktors der Ingenieurwissenschaften

der Fakultät für Maschinenbau des
Karlsruher Institut für Technologie (KIT)

genehmigte
Dissertation

von

M. Sc. Jitti Kasemchainan
aus Bangkok, Thailand

Tag der mündlichen Prüfung:	25.03.2015
Hauptreferent:	Prof. Dr. rer. nat. Michael J. Hoffmann
Korreferent:	Prof. Dr. rer. nat. Helmut Ehrenberg

DOI 10.5445/IR/1000048536

Kurzfassung

Eine zusammengesetzte Schutzschicht aus LATP-Glas mit einer 3 µm dicken LiPON-Sputterschicht wurde in Kombination mit einer Lithiummetallelektrode in Zellen der Lithium-Schwefel-Batterien integriert, mit dem Ziel, die Zyklenfestigkeit zu verbessern. Die Gesamtleitfähigkeit der zusammengesetzten Schutzschicht beträgt 10^{-5} S/cm. Da diese Lithium-Schwefel-Zellen einerseits diese Schutzschicht als Festelektrolyt beinhalten und zusätzlich einen herkömmlichen flüssigen Elektrolyten auf Ether-Basis (1 M LiTFSI in 1:1 Volumen DOL:DME), werden sie als Hybrid-Zellen bezeichnet. Verglichen werden die Ergebnisse dieser Zellen mit jenen von Standardzellen, die allein den flüssigen Elektrolyt enthalten. Die Verbundelektrode aus Schwefel, Ruß und Binder wird durch Foliengießen auf einem kohlenstoffbeschichteten Aluminiumstromableiter hergestellt.

Die Entladekapazität der Hybrid-Zellen ist während der ersten fünf Zyklen 20 % höher als die von Standardzellen. Die erste Entladekapazität der Hybrid-Zellen erreicht 500 mAh/g-Elektrode (g-Elektrode ist die Gesamtmasse von Schwefel, Ruß und Binder) im Vergleich zu 350 mAh/g-Elektrode für die Standardzellen. Dennoch wird ab dem zweiten Zyklus die Abnahme der Lade- und Entladekapazität bei Hybrid-Zellen beobachtet. Um die Ursachen für den Kapazitätsverlust zu identifizieren und den Degradationsmechanismus aufzuklären, wurden galvanostatische Zyklisierungstests, elektrochemische Impedanzspektroskopie und mikrostrukturelle Analysen durchgeführt. Hierfür kamen neben den Standard- und Hybrid-Zellen auch anderer Zellenzusammensetzungen zum

Einsatz, wie z. B. symmetrischen Zellen, die entweder nur Schwefel-Ruß-Elektroden oder nur Lithium-Metall-Elektroden enthalten und Halbzellen mit der Schutzschicht und Lithiummetallelektroden.

Ein Hauptgrund für die Abnahme der Kapazität ist der Verlust der Schwefelkapazität aufgrund von parasitären Reaktionen zwischen Ti in LATP und löslichem elementaren Schwefel oder löslichen Polysulfiden im flüssigen Elektrolyt. Diese Reaktionen führen zur Bildung von Ti (III), das durch Röntgen-Photoelektronenspektroskopie (XPS) nachgewiesen wurde. Dieser Effekt ist für den kurzfristigen Rückgang der Kapazitäten in den ersten fünf Zyklen verantwortlich. Ein zweiter Grund für den Kapazitätsverlust über die langfristige Zyklisierung ist die Verschlechterung der Mikrostruktur des Lithium-Metalls an der Grenzfläche mit der Schutzschicht, die durch elektrochemische Impedanzspektroskopie (EIS) und Rasterelektronenmikroskopie (SEM) nachgewiesen wurde.

Abstract

A composite protective layer of LiPON and LATP with the total conductive of 10^{-5} S/cm is installed in combination with a lithium metal electrode into the cells of the lithium–sulfur batteries with the goal to improve the cell cycleability. The lithium–sulfur cells with this protective layer as solid electrolyte and additional conventional ether-based liquid electrolyte (1 M LiTFSI in 1:1 by volume of DOL:DME), named as *hybrid* cells, are compared to the *standard* cells which have only the liquid electrolyte. The composite electrode of sulfur, carbon black, and binder is prepared by tape-casting on a carbon-coated aluminium current collector.

During the first five cycles, the discharge capacity obtained from the *hybrid* cells is 20 % higher than that of the *standard* ones. The first discharge capacity of the *hybrid* cells reaches up to 500 mAh/g-electrode (g-electrode is the total mass of sulfur, carbon black, and binder) compared to 350 mAh/g-electrode of the *standard* cells. However, the capacity fading behavior of the *hybrid* cells is observed from the second cycle. The investigations based on galvanostatic cycling tests, electrochemical impedance spectroscopy, and microstructural analyses, were performed to address the origins of the capacity fading issue. Aside from the *standard* and *hybrid* cells, other cell assemblies such as the symmetrical cells either with only sulfur-carbon electrodes or with only lithium metal electrodes, and half cells containing the protective layer versus a lithium metal electrode, were investigated.

One of the main reasons for the capacity fading is the loss of sulfur capacity owing to the parasitic reactions between Ti in LATP and soluble elemental sulfur or polysulfides in the liquid electrolyte phase. These reactions lead to the formation of Ti (III), which is detected by X-ray photoelectron spectroscopy (XPS). This issue is responsible for the rapid drop in the capacity during the first five cycles. A second reason for the capacity loss over the long-term cycling is the degradation in the microstructure of the lithium metal at the interface to the protective layer, which was proved by electrochemical impedance spectroscopy (EIS) and scanning electron microscope (SEM).

.

Outline

Kurzfassung i

Abstract iii

Outline v

List of Abbreviations vii

1 Introduction 1

2 State-of-the-Art 3

2.1 Lithium-Sulfur Batteries 3

2.2 Protective Layer for Lithium Metal 11

2.3 Electrochemical Impedance Spectroscopy 15

3 Experimental 27

3.1 Cell Components 27

3.2 Cell Assembly 29

3.3 Electrochemical Tests 32

3.3.1 Galvanostatic Cycling 32

3.3.2 Cycling of *SC vs. SC* Cells 33

3.3.3 Cycling of Aged *Hybrid* Cells 34

3.3.4 Cycling of *Protective Layer* Cells 36

3.3.5 Electrochemical Impedance Spectroscopy 37

3.4 Microstructural Analysis 38

4 Results and Discussion 41

4.1 Discharge & Charge Curves of *Hybrid* & *Standard* Cells 41

4.2 Cycleability of *Hybrid* and *Standard* Cells 46

4.3 Capacity Fading Investigations 48
4.3.1 Cycling of *SC vs. SC* Cells 49
4.3.2 Interface between Lithium metal and LiPON 54
4.3.2.1 Impedance measurement of LATP+LiPON 55
4.3.2.2 Cycling & Impedance measurement of *Protective Layer* Cells 67
4.3.2.3 SEM Analysis 75
4.3.3 LATP in Protective Layer 82
4.3.3.1 OCV & Discharge Curve of Aged *Hybrid* Cells .. 83
4.3.3.2 Impedance measurement of Aged *Hybrid* Cells ... 85
4.3.3.3 Cycling of Aged *Hybrid* Cells 98
4.3.3.4 XPS Analysis 100
5 Conclusion and Outlook 105
6 References 107
Appendix 114

List of Abbreviations

A	Area
AC	Alternating-current
C	Capacitance or C-rate
C_{eff}	Effective capacitance
C_{spec}	Specific effective capacitance
CNLS	Complex Nonlinear Least Squares
CPE	Constant phase element
EIS	Electrochemical impedance spectroscopy
d	Thickness of material
δ	Thickness of Li-metal layer
DC	Direct current
DME	1,2-dimethoxyethane
DOL	1,3-dioxolane
E_f	The final voltage measured after the Li-metal deposition or extraction (under the current polarization),

E_{30s}	The open-circuit voltage recorded 30 seconds after terminating the current polarization
ΔE	The difference between E_f and E_{30s}
ESCA	Electron spectroscopy for chemical analysis
f	Frequency
f_c	Characteristic frequency
i	Current as a function of time
I_0	Current amplitude
IC	Internal combustion
LATP	Lithium-aluminium-titanium-phosphate
LiPON	Lithium phosphorous oxynitride
Li_2S_n	Polysulfides (n is an Integer; $2 < n \leq 8$)
LiTFSI	Bis(trifluoromethane)sulfonamide lithium
MH	Metal hydride
NASICON	Sodium super-ionic conductor
NMP	*N*-methyl-2-pyrrolidone
OCV	Open-circuit voltage
p (CPE-p)	A factor of the impedance of CPE
PAN	Polyacrylonitrile

PVdF	Polyvinylidene fluoride
Q	Capacity (mAh/cm^2) obtained during cycling
Q_{Li}	Specific capacity of Li metal (mAh/g)
R	Resistance
R_{AC}	The total resistance from EIS measurement
R_{DC}	Resistance calculated during constant current
RF	Radio-frequency
R//C	R in parallel to C in equivalent circuit
ρ_{Li}	Density of Li metal
σ	Li-ion conductivity
SC	Sulfur-carbon
SEI	Solid electrolyte interphase
SEM	Scanning electron microscope
t	Time
T (CPE-T)	A factor of the impedance of CPE
θ	Phase shift
τ	Time constant
v	Voltage as a function of time
V_0	Voltage amplitude

ω	Angular frequency
XPS	X-ray photoelectron spectroscopy
Z	Impedance in complex-number domain
Z´	Real part of Z
Z´´	Imaginary part of Z

1 Introduction

The worldwide awakening about adverse effects, e.g. global warming, air-pollutions, and energy crises, from limitless exploitation of fossil fuels like petroleum and natural gas has ignited any public or private sectors come forth for alternative energy technologies. Automotive applications currently tightly rely on internal combustion (IC) engines, which take the main responsibility for the immense consumption of the fossil energy. Electric vehicles with new energy storage systems based on an alternative electrical energy have been therefore introduced into the market so that such problematic IC engines could be replaced.

Supercapacitors, fuel cells, and rechargeable batteries are examples of the possible energy storages. Supercapacitors are electrical energy storage and conversion devices. Once charge carriers have been stored in the electrical double layer in high-surface area electrodes in the devices by an external electric field, they can return electricity when they are connected with external loads. Fuel cells involve conversion of oxygen (O_2) from air and hydrogen (H_2) to generate electricity via electrochemical reactions with continuous supply of H_2. However, to produce massive pure H_2 and to store H_2 as compressed gas, liquid, metal hydrides or metal-organic frameworks bring several challenges.

Rechargeable batteries such as lead-acid, nickel-metal hydride (Ni-MH), lithium(-ion), lithium-sulfur, and lithium-air, are similar to fuel cells in the aspect to undergo electrochemical reactions, but they operate as a closed-system without input of new material. The reactions in the batteries are reversed by charging with electricity. As shown in the Ragone plot of different

energy starge technologies in Figure 1.1, supercapacitors deliver high specific power comparable to the IC engine but with a much lower specific energy. Fuel cells and lithium(-ion) batteries have a specific energy in the level close to the IC engine, even though they still have lower specific power.

However, electrical energy is considered as clean and renewable energy. The production can be environmentally friendly sustained from various natural energies, e.g. wind, water, or solar via wind turbines, hydroelectric dams, and photovoltaics, respectively. For this reason, rechargeable batteries, especially lithium(-ion) batteries are among the most promising candidates of electrochemical energy storage and conversion systems for the electric vehicles.

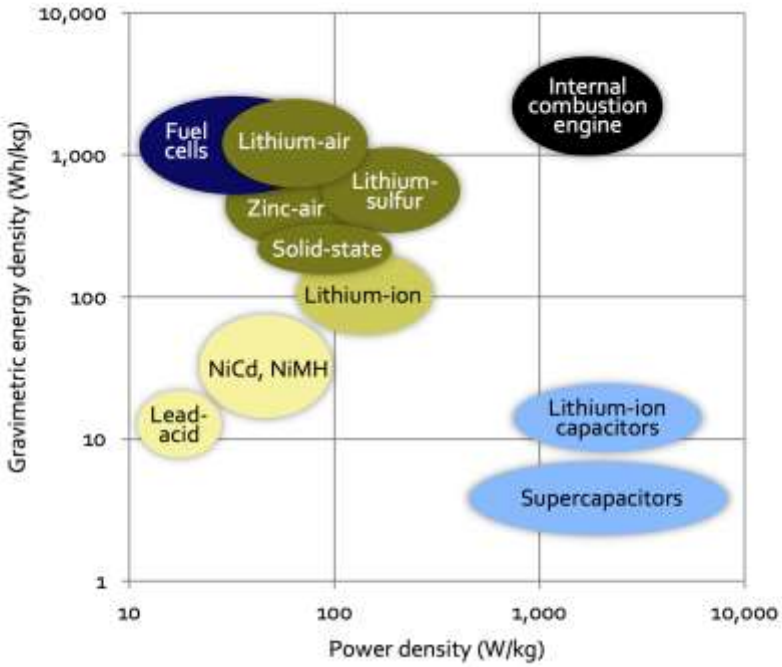

Figure 1.1 Ragone plot of the current and
the next-generation energy storage technologies [Lux 2013]

2 State-of-the-Art

2.1 Lithium-Sulfur Batteries

Lithium-Sulfur batteries have been perceived as one of the most promising energy storage and conversion device for electric vehicles, with a possible driving range of 400 km [Bruce 2012] in comparison to the reachable driving ranges of the other batteries, e.g. nickel-metal hydride, lithium-ion, and zinc-air as shown in Figure 2.1. Sulfur has a high theoretical specific capacity as 1672 mAh/g (Ah/kg), thanks to a maximum uptake of two lithium atoms per one sulfur atom, and the light atomic mass. When an average operating voltage of lithium-sulfur system at 2.2 V is assumed, the theoretical specific energy (also known as gravimetric energy density) can reach up to 2500 Wh/kg. Besides the striking feature of energy storage, sulfur possesses other advantages which include natural abundance, low cost, and relatively low toxicity.

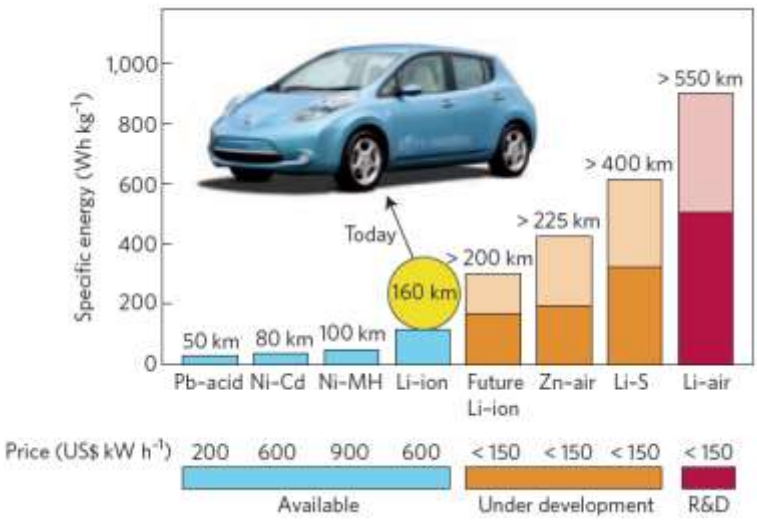

Figure 2.1 Practical specific energies for some rechargeable batteries along with the estimated driving distances and pack prices [Bruce 2012]

In standard lithium-sulfur cells, the positive electrode is composed of sulfur particles embedded in conventionally porous carbonaceous conductive matrices and polymeric binder on carbon-coated aluminum current collector, whereas the negative electrode is simply lithium metal foil. The two electrodes are separated with polymer-based separators soaked with an aprotic and organic liquid electrolyte. The detailed reaction mechanisms of such a lithium-sulfur system are complicated and extensively reported in the literatures [Bruce 2012], [Kolosnitsyn 2008-1], [Akridge 2004], [Kolosnitsyn 2008-2], and [Ji 2010]. The reaction mechansims are summarized as in Figure 2.2 and 2.3, where "Cathode" is the sulfur-carbon electrode, and anode is the lithium metal electrode. The details of the reactions will be briefly given as follows:

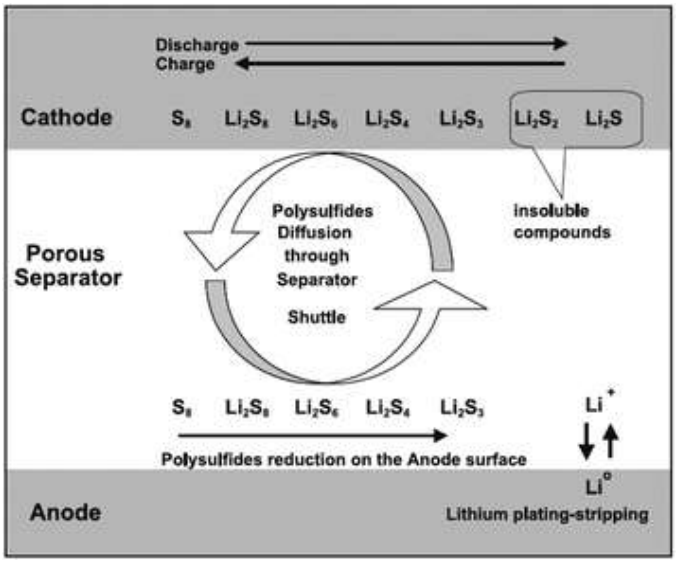

Figure 2.2 Summary of reaction mechanisms during discharge and charge in standard lithium-sulfur batteries [Akridge 2004]

Upon the first discharge at the sulfur electrode, the elemental sulfur, S_8 ring molecule or octet sulfur, starts its electrochemical reduction reaction, see

eq. 2.1, with two lithium-ions and two electrons to form lithium octasulfide, Li_2S_8, one of the polysulfides, subsequently dissolving into the liquid electrolyte. The octasulfide possibly goes through disproportionation reaction to re-form elemental sulfur (eq. 2.2) and/or gets reduced to hexasulfides (eq. 2.3).

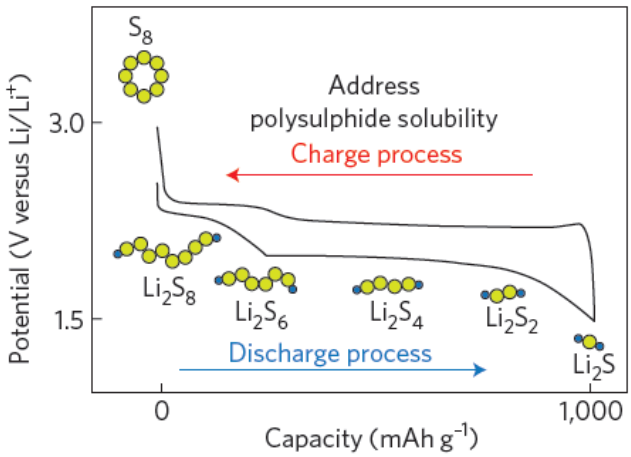

Figure 2.3 Discharge and charge curve (potential as a function of specific capacity) of standard lithium-sulfur batteries [Bruce 2012]

These beginning discharge steps correspond to the upper plateau of the discharge curve in Figure 2.3. At the transition region after the plateau, a further reduction reaction to reduce the chain length of the polysulfides is proposed to be eq. 2.4. Likewise, lithium hexasulfides (Li_2S_6) can also disproportionate as well as dissociate as shown in eq. 2.5 and 2.6, respectively.

$$S_8(s) + 2Li^+ + 2e^- \rightleftharpoons Li_2S_8 \tag{2.1}$$

$$4Li_2S_8 \rightleftharpoons 4Li_2S_6 + S_8 \tag{2.2}$$

$$3Li_2S_8 + 2Li^+ + 2e^- \rightleftharpoons 4Li_2S_6 \tag{2.3}$$

$$2Li_2S_6 + 2Li^+ + 2e^- \rightleftharpoons 3Li_2S_4 \tag{2.4}$$

$$2Li_2S_6 \rightleftharpoons Li_2S_8 + Li_2S_4 \tag{2.5}$$

$$Li_2S_6 \rightleftharpoons 2LiS_3 \tag{2.6}$$

During the lower plateau of the discharge curve in Figure 2.3, solid lithium disulfide and sulfide (Li_2S_2 and Li_2S respectively) are generated via the electrochemical reduction coupling with disproportionation of Li_2S_4 (eq. 2.7 and 2.8, respectively). At the end of the plateau, lithium disulfide should be reduced and transformed to lithium sulfide (eq. 2.9).

$$Li_2S_4 + 4Li^+ + 4e^- \rightleftharpoons Li_2S_2 + 2Li_2S \tag{2.7}$$

$$5Li_2S_4 \rightleftharpoons 3Li_2S_6 + 2Li_2S \tag{2.8}$$

$$Li_2S_2 + 2Li^+ + 2e^- \rightleftharpoons 2Li_2S + 2Li_2S \tag{2.9}$$

The final discharge product of lithium sulfide (Li_2S) is not electronically/ionically conductive and not soluble in the liquid electrolyte. Its precipitation and full coverage with a specific thickness on carbon-based conductive particles would end the discharge as evidenced by the steep voltage drop of the discharge curve in Figure 2.2, regardless of the fact that there are still remaining soluble polysulfides inside the liquid electrolyte.

Meanwhile at the lithium metal electrode, lithium atoms are oxidized to release lithium ions into the liquid electrolyte medium and electrons to the external circuit (eq. 2.10). The direct reactions between metallic lithium and soluble polysulfides without liberation of electron to the external circuit can occur, which produces insoluble Li_2S_2 and/or Li_2S like in eq. 2.11 and 2.12, depositing as a film on the lithium metal surface. This film may, of course,

react with long-chain polysulfides, reforming soluble shorter-chain polysulfides and moving back into the solution of liquid electrolyte, like in eq. 2.13, for example.

$$Li \rightleftharpoons Li^{+} + e^{-} \tag{2.10}$$

$$6Li + 2Li_2S_6 \rightleftharpoons Li_2S_8 + 4Li_2S \tag{2.11}$$

$$2Li + Li_2S_6 \rightleftharpoons Li_2S_4 + Li_2S_2 \tag{2.12}$$

$$Li_2S + Li_2S_6 \rightleftharpoons Li_2S_3 + Li_2S_4 \tag{2.13}$$

The charge process of lithium-sulfur batteries can be simply understood by the reverse procedure of the discharge. The overall charge reaction on the sulfur electrode side is to oxidize insoluble lithium sulfides to soluble polysulfides and finally to solid elemental sulfur, or generally noticed by an increase of the oxidation states of sulfur form -2 to 0. Conversely on the lithium metal side, the oxidation state of lithium reduces from +1 to 0, which marks the circumstance of re-depositing or plating lithium metal.

However, as a special aspect of lithium-sulfur batteries, the shuttle mechanism which is consolidated in Figure 2.2, should be mentioned. In the recharging stage, long chain polysulfides, e.g. Li_2S_6, are once formed by oxidizing the shorter polysulfides, e.g. Li_2S_4 (eq. 2.14) at the sulfur electrode, resulting in an increase of the polysulfide concentration. As a result of this concentration driving force, a diffusion process of polysulfides towards the lithium metal electrode is triggered, where the polysulfide concentration is relatively low. On the lithium metal surface, the diffusing polysulfides react with lithium metal, particularly the highly reactive ones generated after redeposition or re-plating (eq. 2.15), and the shorter polysulfides are thereafter

formed (eq. 2.12). The shorter polysulfides migrate back to the sulfur electrode and re-engage in the reduction process. This phenomenon repeats like an internal loop of the reactions eq. 2.14, 2.15, and 2.12, for instance, and creates an overcharge capacity.

At the sulfur electrode

$$2Li_2S_4 \rightleftharpoons 2Li_2S_6 + 2Li^+ + 2e^- \tag{2.14}$$

At the Li metal electrode

$$Li^+ + e^- \rightleftharpoons Li \tag{2.15}$$

$$2Li + Li_2S_6 \rightleftharpoons Li_2S_4 + Li_2S_2 \tag{2.12}$$

On one hand, this shuttle mechanism partly protects the lithium-sulfur system from parasitically overcharging such as the degradation by oxidizing the organic solvent in the liquid electrolyte, gas evolution, and possible thermal runaway thereafter. On the other hand, it brings drawbacks to the usage of such a system and to the system, itself. That is more external energy needed to perform a complete charge of the batteries. When polysulfides are sustained to have a liberating interaction with lithium metal, one cannot be certain that the consequences are merely reversible.

Undoubtedly, lithium-sulfur batteries occupy considerable advantages over other lithium energy storage systems. The successful commercialization has not been released up to now. Numerous problems directly limiting cycleability, remain to be tackled owing to the intrinsic behaviors of each component:

- Growth of lithium metal dendrites during charging, which potentially leads to short-circuit
- Continual formation of solid electrolyte interphase (SEI) due to the spontaneous reduction reaction of metallic lithium and organic solvent, amplifying internal impedance and losing active lithium metal and liquid electrolyte [Aurbach 2009]
- Irreversible building-up of an insulating surface film of Li_2S and/or Li_2S_2 on lithium metal surface from reactions between lithium metal and polysulfides which increases the impedance and lowers the amount of active lithium metal and its active site [Choi 2008] and [Cheon 2003]
- Agglomeration of Li_2S and/or Li_2S_2 in the sulfur electrode, turning electrochemically inaccessible and high-resistance layer, responsible for poor rate-capability [Cheon 2003] and [Jeon 2002]
- Microstructural degeneration of the carbonaceous conductive matrices of binder and carbon black, loss of electrical contact for insulating sulfur, owing to around 50 % volume change of transformation from solid S_8 to Li_2S, or vice versa [Elazari 2010]
- Shuttle mechanism markedly downscales the coulombic efficiency in the charge process, and diminishes the active sulfur mass utilization in the discharge process [Ji 2010] and [Rao 1981]

To overcome such problems in lithium-sulfur batteries, various electrode modifications have been achieved and reported in literatures, which can be classified as an overview into two main categories:

1) Confinement of sulfur species, e.g. elemental sulfur or polysulfides to remain inside the composite sulfur electrodes,

2) Enhancement of surface film on the lithium metal electrode to be more stable or replacement of the lithium metal electrode with less reactive materials

Examples of the first categories can be the encapsulation of sulfur within mesoporous carbon e.g. CMK-3 which is also coated with polyethylene glycol (PEG) [Nazar 2009] or the sulfur-imprenated disordered carbon nanotubes [Guo 2011] and [Wang 2008], the embedded sulfur in a conductive polymer matrix of polyacrylonitrile (PAN) together with carbon nanotubes [Wang 2003] [Wei 2011], or the addition of nano-sized $Mg_{0.6}Ni_{0.4}O$ to have polysulfides adsorbing effects [Song 2004].

According to Aurbach *et al.*,[Aurbach 2009] the lithium metal electrode is better passivated when an additive lithium nitrate ($LiNO_3$) is added in a conventional ether-based electrolyte, and the shuttle mechanism can be inhibited. To go in the direction of an alternative electrode, silicon was utilized instead of lithium metal on the basis of minimization of parasitic reactions with polysulfides [Elazari 2012] and [Hassoun 2012].

In this work, the standard composite sulfur-carbon electrode will be used and modification will be focused on the lithium metal electrode as an intention to improve the capacity and cycleability of the lithium-sulfur cells.

2.2 Protective Layer for Lithium Metal

As mentioned in the previous section, the major challenges of lithium-sulfur batteries lie strictly on the lithium metal electrode. The high reactivity of metallic lithium induces irreversible parasitic reactions with any component in the batteries, either soluble sulfur, polysulfides, organic solvents, or anions of lithium salts in the liquid electrolyte. Additionally, free formation of dendrite-shaped lithium metal through the liquid electrolyte phase when redepositing lithium atoms on the lithium metal surface is an issue to be taken care of. As a consequence, employing lithium metal as the electrode directly suppresses the cycleability of the batteries. In order to avoid the undesired phenomena, the concept of protecting the metallic lithium electrode from any species in the liquid electrolyte medium and the dendrite growth with a protective layer was chosen to improve the cycleability of lithium-sulfur batteries. In general, the layer must have a function of solid-state lithium-ion conductor. The requirements for this protective layer on the lithium metal based on five main properties, structural, mechanical, electrical, electrochemical, and chemical with details are as follows:

- Structural: no available open porosity in the protective layer for liquid electrolyte to move through directly and lithium metal to percolate as dendrite

- Mechanical: able to maintain the structure and restrain the shear stress during the growth (deposition) of lithium metal, which is 9 GPa [Monroe 2003]

- Electrical: good lithium-ion conductivity, but poor electronic one, considering liquid electrolyte as reference

- Electrochemical: not oxidizable and reduceable in a wide range of potential vs. lithium Li^0/Li^+, at least between 0.0 - 3.0 V in case of conventional lithium-sulfur batteries
- Chemical: non-soluble in liquid electrolyte, inert or compatible with lithium metal and the liquid electrolyte, active sulfur species (elemental sulfur and polysulfides)

Due to their high mechanical strength, ceramic materials have a better potential withstand the growth of lithium-metal dendrite than typical solid polymer electrolytes..Commerically available LATP ceramic plates are structurally dense but not stable against lithium metal, whereby lithium can be inserted into LATP lattices. LiPON is a better material as it is stable with lithium metal, but a substrate like a LATP plate is need for sputtering LiPON. A composite ceramic electrolyte of LiPON and LATP was therefore chosen as a protective layer for lithium-sulfur batteries. The other ceramic electrolytes that could also be used are such as Garnet-type, Perovskite-type, Alumina-composite, etc reported by P. Knauth [Knauth 2009]. Table 2.1 summarizes the properties of both lithium-ion conductors.

LiPON:

Lithium Phosphorous Oxynitride is an amorphous thin-film glass lithium ion conductor. The manufacturing process for LiPON can be achieved by Radio-Frequency (RF) magnetron sputtering of a lithium phosphate (Li_3PO_4) target

in nitrogen (N_2) and argon (Ar) gases onto a substrate [Yu 1997] and [Boukbir 1989]. A resulting LiPON material has a generalized chemical composition of $xLi_2O:yP_2O_5:zPON$ where PON is phosphorousoxynitride [Boukbir 1989]. The normalized compositions to phosphorous of LiPON, as reported in Dudney's work [Dudney 2000], can vary from $Li_{3.3}PO_{3.8}N_{0.24}$ to $Li_{3.6}PO_{3.3}N_{0.69}$.

LATP:

LATP in this thesis is referred to a **L**i-**A**l-**T**i-**P**hosphate lithium-ion conducting glass-ceramic which is purchased from OHARA Corp. It has a NASICON-type (Sodium super-ionic conductor) crystallographic structure and is synthesized by melted and polished processes to obtain a plate. The details of synthesis can be found from the website of OHARA Corp.[OHARA]. The precursor is a combination of Li_2O, Al_2O_3, SiO_2, P_2O_5, TiO_2, and GeO_2. LATP has remarkable specifications such as high lithium-ion conductivity at room temperature, dense (non gas-permeable), and smooth surfaces (necessary for LiPON sputtering). As received, LATP square plates have a dimension of 1 inch x 1 inch x 155 µm. They were cut into four-equal squares with a size of 12.7 mm x 12.7 mm x 155 µm (Figure 2.4) by a diamond-blade saw.

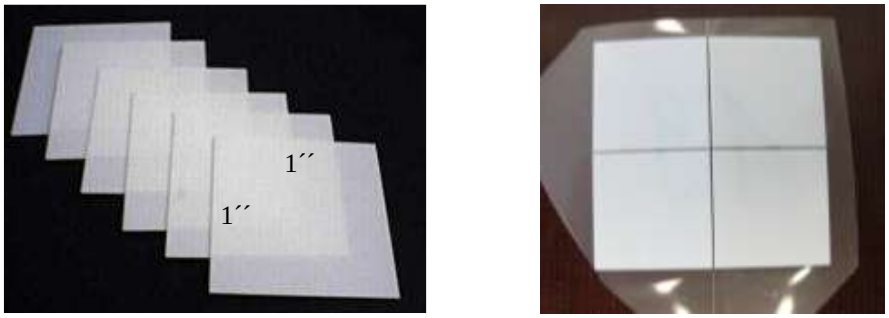

Figure 2.4 LATP plates as received [OHARA] and after cutting.

Table 2.1 Relevant properties of LiPON and LATP

Properties	LIPON [Dudney 2000]	LATP [OHARA]
Thickness, µm	min. 3	155
Conductivity at RT, S/cm	*ca.* 10^{-6}	*ca.* 10^{-4}
Typical Generalized Chemical composition	$Li_xPO_yN_z$	$Li_{1+x}Al_xGe_yTi_{2-x-y}P_3O_{12}$ main crystal phase $Li_{1+x+3z}Al_x(Ti, Ge)_{2-x}Si_{3z}P_{3-z}O_{12}$ sub crystal phase
Electrochemical stability, V vs. Li^0/Li^+	0 – 5.5	> 2.5 [Takada 2009]

2.3 Electrochemical Impedance Spectroscopy

Electrochemical impedance spectroscopy (EIS), also known as alternating-current (AC) impedance spectroscopy, is a powerful technique to analyze and distinguish complex electrochemical processes, so as to acquire relevant information in terms of the electrical properties e.g. resistance, capacitance, and conductances.

Potentiostatic EIS, frequently selected for characterization of batteries, involves a series of frequencies of a small alternating voltage perturbation, $v(t)$ as in (eq. 2.16) on an electrochemical system. Then it measures the alternating current response, $i(t)$ with a phase shift, θ, as in eq. 2.17. This phase shift can be varied when the frequency changes. A commonly recognized frequency, f, has the dimension of Hertz (Hz), yet an angular frequency, ω, is preferably represented in mathematical equations for describing a sinusoidal waveform. .

$$v(t) = V_0 \sin(\omega t) \tag{2.16}$$

$$i(t) = I_0 \sin(\omega t + \theta) \tag{2.17}$$

$$\omega = 2\pi f \tag{2.18}$$

where V_0 and I_0 are the amplitudes of voltage perturbation and of current response, respectively.

The corresponding plots of a voltage perturbation (eq. 2.16) and a current response (eq. 2.17) can be found in Figure 2.5. Analogous to Ohm's Law,

the impedance, Z, is defined by the ratio of the applied voltage to the measured current. From Euler's formula in complex-number domain, the impedance at a frequency can be expressed in eq. 2.19 or simply generalized in eq. 2.20.

$$Z = \frac{v(t)}{i(t)} = \frac{V_0 \sin(\omega t)}{I_0 \sin(\omega t + \theta)} = \frac{V_0 e^{j\omega t}}{I_0 e^{j(\omega t + \theta)}} = |Z| e^{-j\theta} = |Z| (\cos(\theta) - j\sin(\theta)) \tag{2.19}$$

where the magnitude of Z is denoted as $|Z|$ and is equal to $\frac{V_0}{I_0}$,

$e^{-j\theta} = \cos(\theta) - j\sin(\theta)$, and $j = \sqrt{-1}$

$$Z = Z' + jZ'' \tag{2.20}$$

where $Z' = |Z|\cos(\theta)$ is the "real" part or resistance,

and $Z'' = -|Z|\sin(\theta)$ is the "imaginary" part or reactance.

The phase shift can be obtained by the following eq. (2.21).

$$\theta = \arctan(\frac{Z''}{Z'}) \tag{2.21}$$

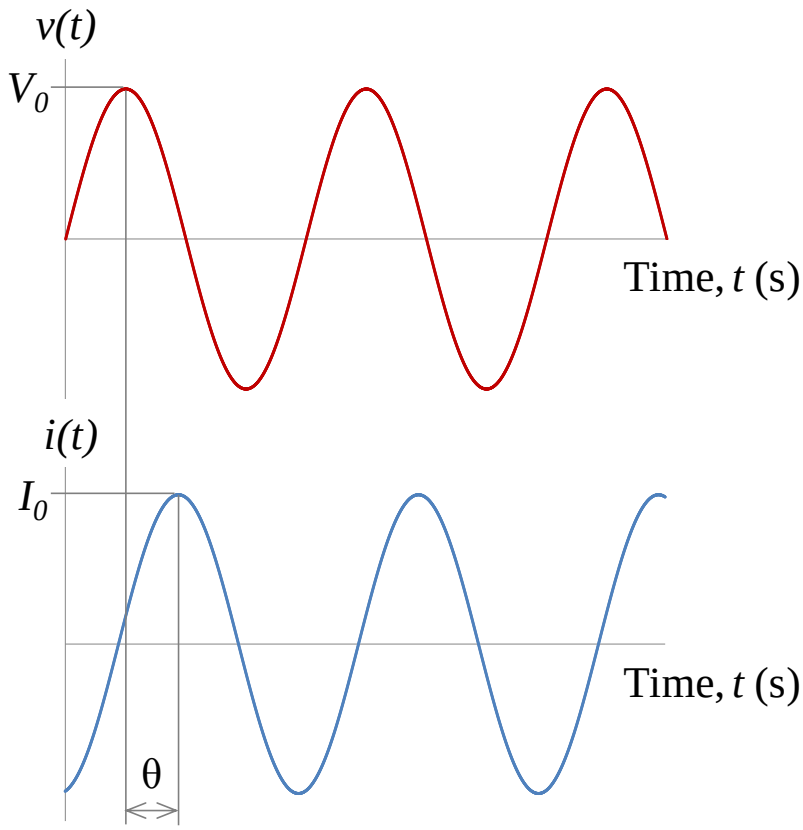

Figure 2.5 An example of a sinusoidal voltage perturbation and a current response as a function of time at a frequency, reproduced from [Macdonald 1987].

To represent the impedance data at a whole range of frequencies, the real part is plotted on the X-axis and the imaginary part is plotted on the Y-axis, this is so-called the Nyquist plot. Another way to present the impedance is the Bode plot, whereby its magnitude and phase shift are plotted versus the frequency in Hz. These plots signify the characteristics of a measured system, as well as lead us to qualitative and quantitative data interpretation by adopting an appropriate electrical equivalent circuit. If a simple parallel combination of a resistance, R, and a capacitance, C, or denoted as R//C is taken into account, the impedances of such a system are described in eqs. 2.22, 2.23, and 2.24.

$$Z_R = R \tag{2.22}$$

$$Z_C = \frac{1}{j\omega C} \tag{2.23}$$

$$Z_{R//C} = \left(\frac{1}{Z_R} + \frac{1}{Z_C}\right)^{-1} = \frac{R}{1+\omega^2 R^2 C^2} + j\left(-\frac{\omega R^2 C}{1+\omega^2 R^2 C^2}\right) \tag{2.24}$$

The magnitude, $|Z_{R//C}|$, and phase shift, $\theta_{R//C}$, of $Z_{R//C}$ or are shown in eqs. 2.25, and 2.26, respectively.

$$|Z_{R//C}| = \sqrt{\left(\frac{R}{1+\omega^2 R^2 C^2}\right)^2 + \left(-\frac{\omega R^2 C}{1+\omega^2 R^2 C^2}\right)^2} = \sqrt{\frac{R^2}{1+\omega^2 R^2 C^2}} \tag{2.25}$$

$$\theta_{R//C} = \arctan\left(-\frac{\omega R^2 C}{1+\omega^2 R^2 C^2} \Big/ \frac{R}{1+\omega^2 R^2 C^2}\right) = \arctan(-\omega RC) \tag{2.26}$$

Eqs. 2.25 and 2.26 are used for the Bode plots.

Re-arranging eq. 23 gives the relation between the real and imaginary parts, $Z'_{R//C}$, and $-Z''_{R//C}$, respectively, of $Z_{R//C}$ in eq. 2.27, which is used for the Nyquist plot.

$$\left(Z'_{R//C} - \frac{R}{2}\right)^2 + \left(-Z''_{R//C}\right)^2 = \left(\frac{R}{2}\right)^2 \tag{2.27}$$

the impedance spectrum demonstrated by Nyquist and Bode plots of this system in Figure 2.6 and 2.7, respectively

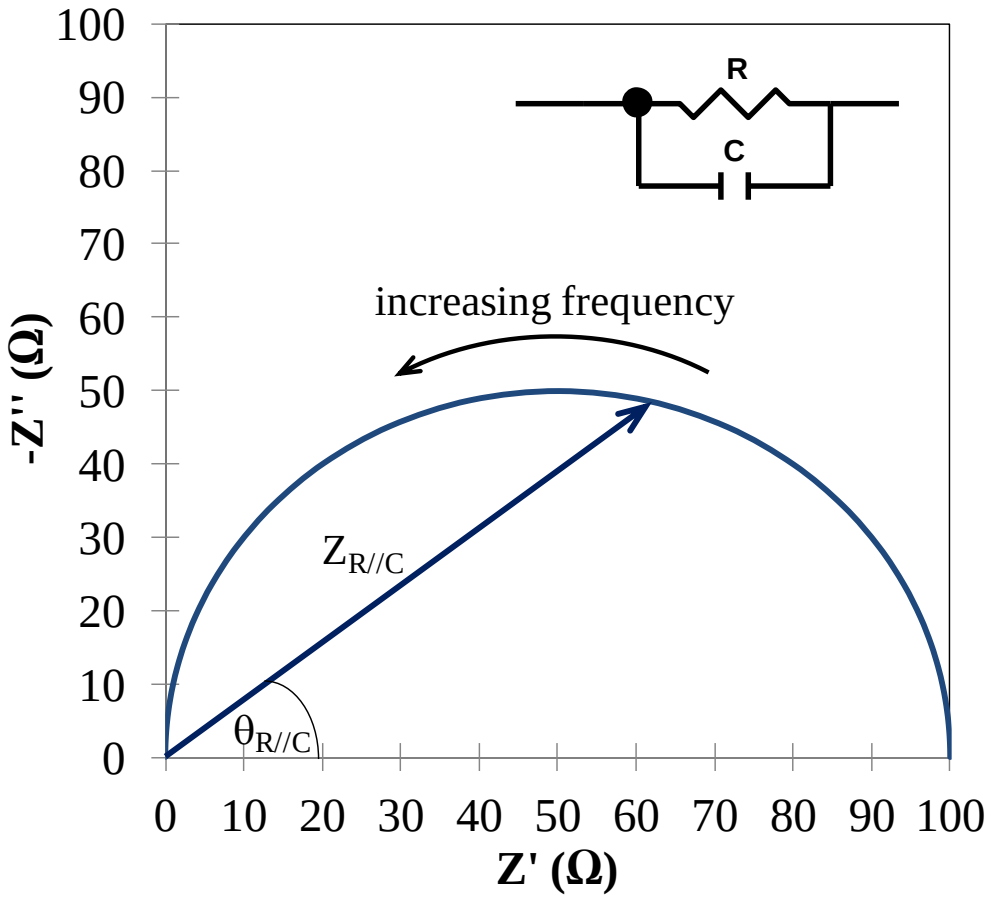

Figure 2.6 A Nyquist plot with an examplary impedance vector of the impedances at different frequencies of an equivalent circuit R//C

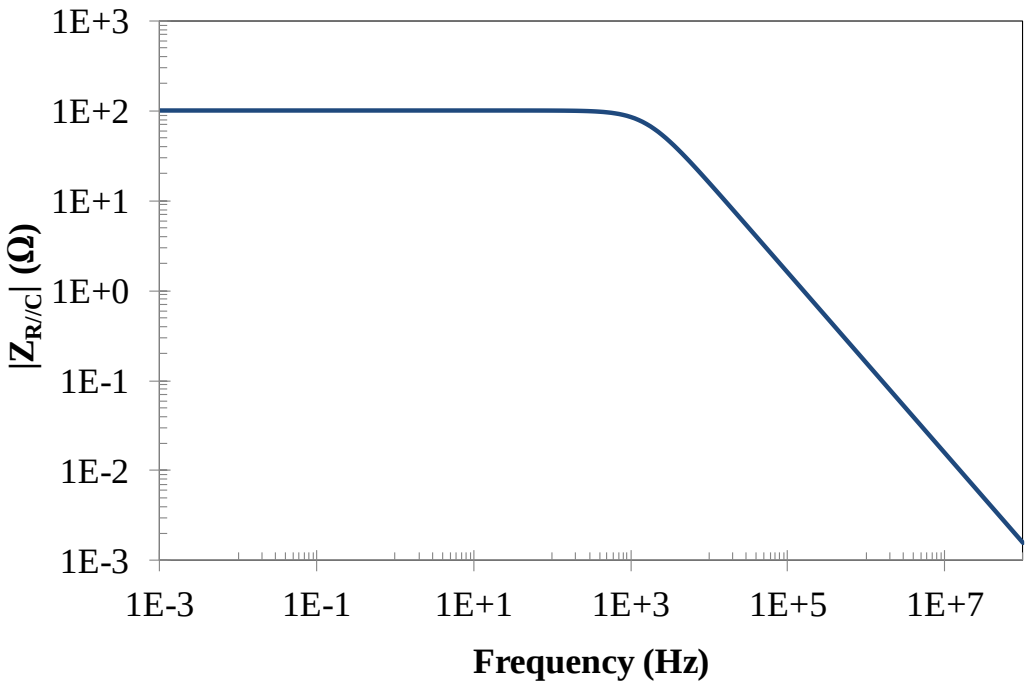

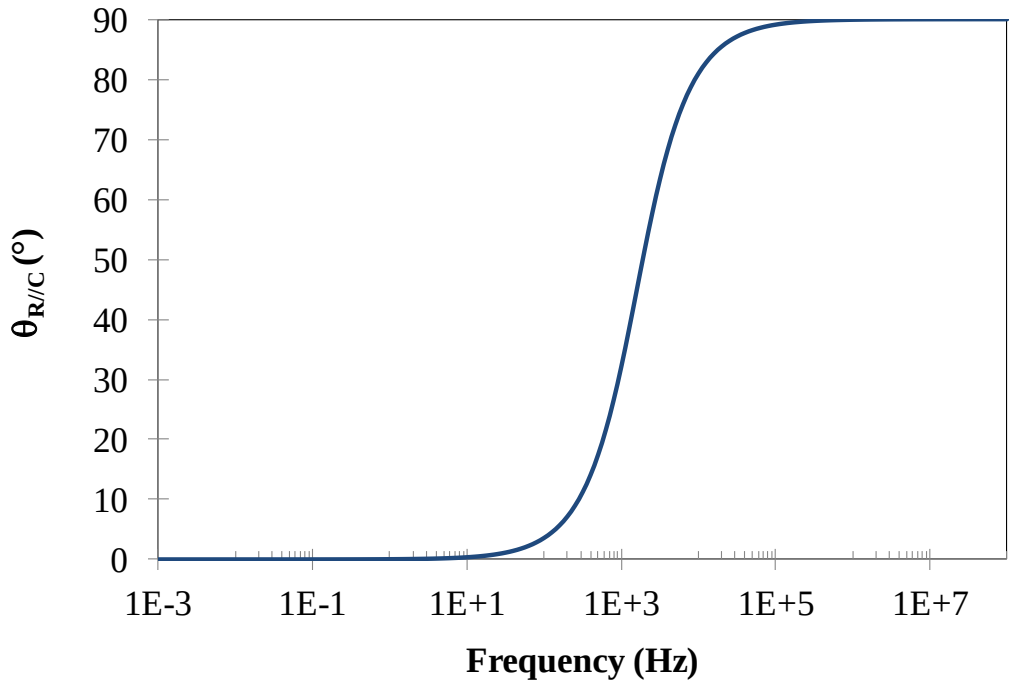

Figure 2.7 Bode plots of the magnitude of the total impedance, (upper) and the phase shift, (lower) as function of frequency of an equivalent circuit R//C

Data fitting of a measured impedance spectrum in the Nyquist plot is performed by building up an electrical equivalent circuit The fitting is implemented by executing a software called ZView from Scribners Associates Inc.. The method for the data fitting is the Complex Nonlinear Least Squares (CNLS). Optimized fitted data can be obtained via minimizing the object function, S, eq. 2.28 [Macdonald 1987], which is basically the sum of squared deviation between each measured and fitted values of impedance.

$$S = \sum_{i=1}^{N} w_i \{[Z_i^{'} - Z_i^{'}(\omega_i, a_k)]^2 + [Z_i^{''} - Z_i^{''}(\omega_i, a_k)]^2\} \qquad (2.28)$$

$Z_i^{'}$ and $Z_i^{''}$ are the measured real and imaginary parts, respectively, of an impedance Z_i at a frequency ω_i. w_i is the weight factor and is set to "Calc-Modulus" according to ZView. $Z_i^{'}(\omega_i, a_k)$ and $Z_i^{''}(\omega_i, a_k)$ from the model function are the fitted values of the real and imaginary part, respectively, of an impedance corresponding to the assigned equivalent circuit model, at which a_k indicates an initial estimate that has to be given by a user to initiate the fitting sequences.

Building up an appropriate equivalent circuit for the data-fitting, the types of circuit elements and their combinations in order to physically interpret the measure systems are crucial. In case of solid electrolytes [Boukamp 2004], [Imanishi 2008], and [Thangadurai 2003] and Li(-ion) batteries [Boukamp 2004], [Aurbach 2000], [Illig 2010], and [Levi 1999], a common parallel combination of resistance, R, and capacitance, C, see Figure 2.8 is added in an equivalent circuit to describe the movement and storage of charge carriers across or in any of the following contributions: grain (bulk), grain boundaries of solid electrolytes, surface film, liquid electrolyte, and

interfaces between two different materials, e.g. interface between solid and liqsuid electrolyte, or between lithium metal and liquid electrolyte. The resistance and capacitance from the interface contribution are also called charge-transfer resistance and electrical-double-layer or space-charge capacitance. The total impedance of a system is, in principle, measured by adding up the impedances of all the contributions. Accordingly, each R//C combination in the system is assumed to be connected to the others in series or "Voigt" structure in an equivalent circuit as shown in Figure 2.8 (a) and (b).

There are nonetheless contributions that do not follow the R//C combination. Some contributions like geometric (grain/bulk) or liquid electrolyte possess too low capacitance combined with the highest input frequency of 1 MHz limited from the measurement devices for Gamry Interface 1000. By this, the impedance of such a capacitance is much higher than that of the corresponding resistance. During voltage perturbation, the majority of the current would pass through the resistance rather than the capacitance. As a result, the capacitance is negligible and the R//C is reduced to R. Likewise, if the resistance approaches to infinity, lin such a case of charge-blocking interface, e.g. Au and LATP or Cu and LiPON, where neither Li^+ or e^- are able to move across R//C is replaced by C.

Most measured systems contain no ideal capacitance, C. Due to the fact of inhomogeneous conditions and distribution of microscopic material properties (interface is not smooth and uniform but presents surface defects, local charge inhomogeneity, variation in composition), an element called Constant Phase Element, CPE is introduced to have a better data fitting instead of C [Macdonald 1987] and [Boukamp 2004]. Its impedance is empirically defined by eq. 2.29.

$$Z_{CPE} = \frac{1}{(j\omega)^p T} \tag{2.29}$$

By fitting, the values of T (CPE-T) and p (CPE-p) are obtained. CPE-p must be in the range of 0 to 1. For the special case that p is 1, T becomes C for an ideal capacitance. From these values, together with the resistance value, R, the effective capacitance, C_{eff}, which has a unit of Farad (F) is computed by eq. 2.30.

$$C_{eff} = R^{(1-p)/p} \cdot T^{1/p} \text{ [F]} \tag{2.30}$$

By further taking into account geometry factors, i.e. electrical contact area, and thickness of a material, specific effective capacitance, C_{spec}, in either the dimentsions of F/cm or F/cm^2, is obtained. This specific capacitance can differentiate the types of contributions in the electrochemical system. Each contribution has its specific range for C_{spec}, that is classified in Table 2.2. The specific effective capacitance for either the grain or the grain boundary is calculated according to eq. 2.31 by including the thickness of the material, d, and the contact area, A, where the electric polarization takes place by an external electric field.

$$C_{spec} = C_{eff} \frac{d}{A} \text{ [F/cm]} \tag{2.31}$$

For the contribution of the electrical double layer at the interface between two materials, only the contact area at the interface, A, is considered for the specific effective capacitance, as shown in eq. 2.32.

$$C_{spec} = C_{eff} \frac{1}{A} \text{ [F/cm}^2\text{]} \tag{2.32}$$

Furthermore, the time constant, τ and the characteristic frequency, f_c of the contributions are calculated as follows:

$$\tau = RC_{eff} \text{ [s]} \tag{2.33}$$

$$f_c = \frac{1}{2\pi\tau} \text{ [Hz]} \tag{2.34}$$

Besides R and C or CPE, Warburg diffusion (Z_W) [Aurbach 2000], [Illig 2010], and [Levi 1999] and inductance (L) [Illig 2010] and [Vetter 2005] are often included in equivalent circuits. In this work, the two contributions were not apparent in the measured impedance spectra Therefore, they were not considered for the equivalent circuit and data fitting.

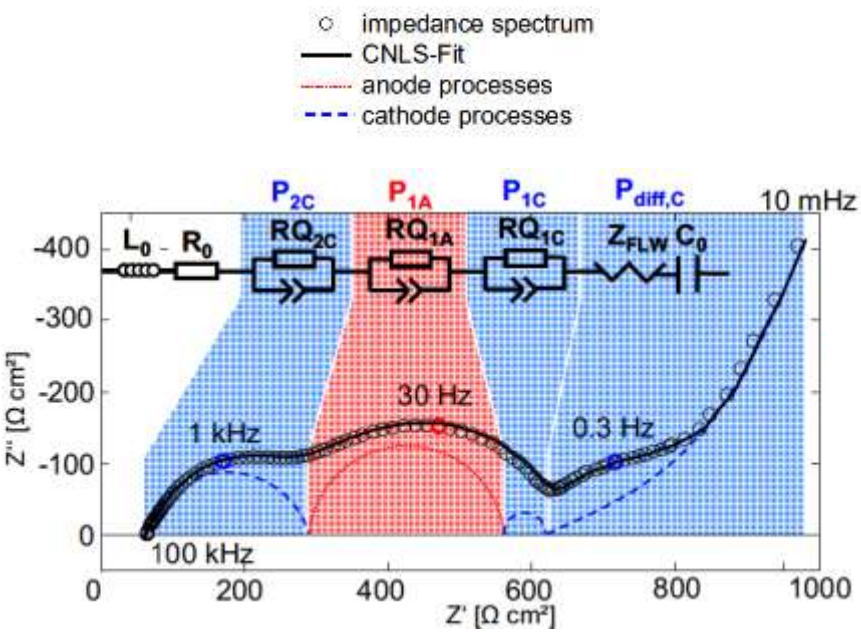

Figure 2.8 (a) A measured impedance spectrum (Nyquist plot) of a Li-ion cell with a fitted curve showing different contributions of the equivalent circuit [Illig 2010]

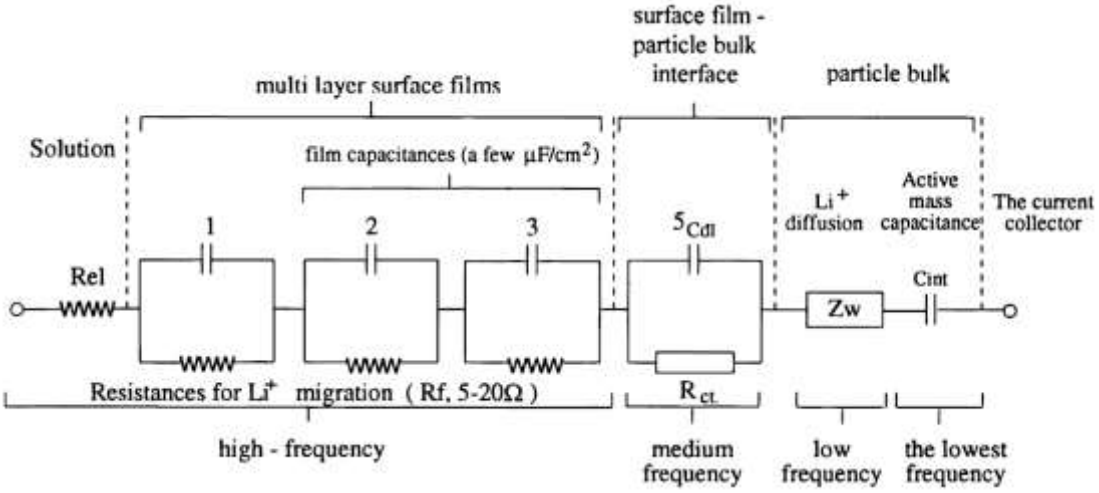

Figure 2.8 (b) an Example of a proposed equivalent circuit with detailed contributions for a Li-ion battery [Levi 1999].

Table 2.2 Classification of contributions according to specific effective capacitances [Boukamp 2008]

Source of contributions	Approximate value
Geometric/Bulk	2 – 20 pF (cm^{-1})
Grain boundaries	1 – 10 nF (cm^{-1})
Double layer/Space charge	0.1 – 10 μF/cm^2
Surface charge/Adsorbed species	0.2 mF/cm^2
(Closed) pores	1 – 100 F/cm^3

High frequencies

Low frequencies

.

3 Experimental

3.1 Cell Components

Composite Sulfur electrode

The sulfur electrode was prepared entirely inside an Argon-filled glovebox by tape-casting a slurry composed of elemental sulfur, carbon black, polyvinylidene fluoride (PVdF) particles and a solvent of *N*-Methyl-2-pyrrolidone (NMP) on a carbon-coated aluminium current collector (30 µm thickness). The wet thickness of the slurry on the current collector accounted to 500 µm, whereby the electrode layer's thickness reduced to approximately 40 µm after solvent evaporation from the slurry. The final mass composition of the dried electrode is 40 % elemental sulfur, 40 % carbon black, 20 % PVdF binder, making up a sulfur (capacity) loading of around 2 mAh/cm^2.

Li metal electrode

Lithium metal foil used for all the concerned experiments was 200 µm thick, purchased from China Energy Lithium Co., Ltd. [China Energy].

Liquid electrolyte

Chosen on the basis of typically use in lithium-sulfur batteries, a solution of ether-based solvents with a lithium salt of a concentration of 1 Molar was prepared as liquid electrolyte. The organic solvents purchased from Sigma-Aldrich are 1,3-dioxolane (DOL) and 1,2-dimethoxyethane (DME), see Figure 3.1 (left) and (middle), respectively. The lithium salt is Lithium Bis(Trifluoromethanesulfonyl)imide (LiTFSI), see Fig. 3.1 (right), which has the

molar mass of 287.09 g/mol. The mixing was carried out inside a glovebox by using equal volumes of both solvents to dissolve the salt.

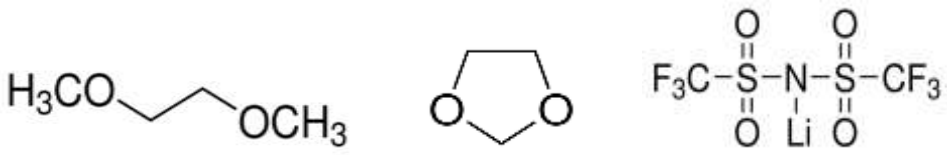

Figure 3.1 Molecular structures [Sigma-Aldrich] of 1,2-dimethoxyethane (left), 1,3-dioxolane (middle), and Lithium Bis(Trifluoromethanesulfonyl)imide (right)

Separator

Two types of separators were chosen; one was Freudenberg Fleece FS21090 with the thickness of 230 µm and another was Celgard® 3400 which is 25 µm thick. They were introduced into a glovebox via heating under vacuum of around 5 x 10^{-2} mbar to 70 °C for 8 h to minimize the moisture content.

Protective layer (Solid electrolyte)

To obtain a composite protective layer of Cu-LiPON-LATP plate, firstly one side of a LATP plate with 12.7 mm x 12.7 mm x 155 µm was fixed on a piece of heat-resistive tape (Kapton®) and placed on a silicon wafer before being introduced in a LiPON sputtering chamber. After an eight-hour sputtering process, the sputtered plate was taken out and the tape was removed. The LiPON-LATP plate was further processed for 15-minuite copper sputtering by using a mask to have a specific area of a Cu layer. This resulted in a 10-mm-diameter circular area of a Cu layer on the LiPON layer, see Figure 3.2. The ready-to-use Cu-LiPON-LATP protective layer was introduced directly into an Ar-filled glovebox so that undesired interactions between

LiPON and moisture were minimized. The photographs of LATP plates after each processing step are shown in Fig. 3.2.

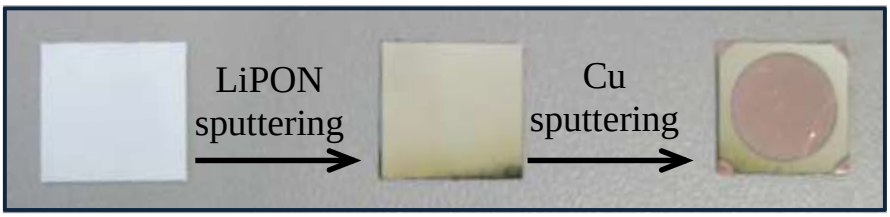

Figure 3.2 LATP plate (left), LiPON sputtered on LATP (middle) and Cu sputtered on LIPON-LATP (right)

3.2 Cell Assembly

All the cells towards electrochemical characterization were assembled inside an Ar-filled glovebox. The conditions of the atmosphere inside the glovebox are: ca. -4 mbar relative to the normal atmospheric pressure, both H_2O and O_2 levels lower than 0.1 ppm. Every cell assemblies are denoted as follows: *Au-LATP*, *Liquid-LATP*, *protective layer*, *Li vs Li*, *standard SC vs Li*, *hybid SC vs Li*, and *SC vs SC*; the details of their configurations and components can be found in Table 3.1 and Illustration 3.1. In general, the electrodes i.e. SC electrode, lithium metal foil, and the separator of Freudenberg fleece were punched out in a disc-shape with a diameter of 10-mm. For the liquid electrolyte, it was added directly on a fleece by using micro-liter Pipette. The needed components were stacked together concentrically in each test cell. Two types of test cells were used for assembling, EL cell-ECC-STD and Swagelok T-cell, see Figure 3.3.

In some cell assemblies, i.e. *Li vs. Li* and *standard SC vs. Li* cells, employing only Li metal without protective layer, the 12-mm-diameter disc-shape of Celgard was punched and included in addition to the Fleece. The Celgard was placed on the 10-mm-diameter lithium metal foil in order to avoid a direct contact with another electrode or the possibility of short-circuit. A special case of *SC vs. SC* assembly is that a 4-mm-diameter lithium metal foil was cut and placed as a reference electrode, and the 10-mm SC electrodes were located at the positive and negative as in Illustration 3.2. Apart from a piece of the Fleece, it was necessary to put two pieces of 10-mm-diameter Celgard in between the reference Li and both SC electrodes in order to secure no direct contact between the SC and electrodes and the Li.

Figure 3.3 Photographs of EL cell-ECC-STD [EL cell] (left) and Swagelok T-cell (right) [Swagelok]

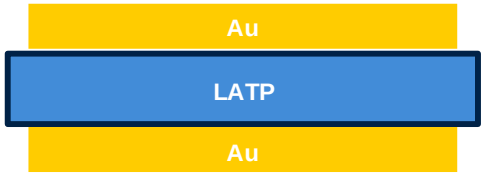

(a) *Au-LATP*

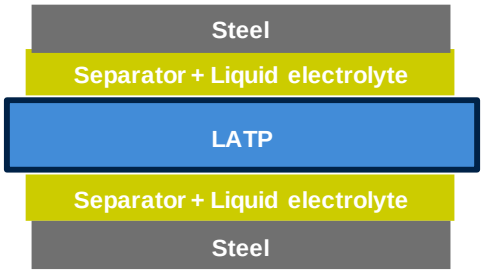

(b) *Liquid-LATP*

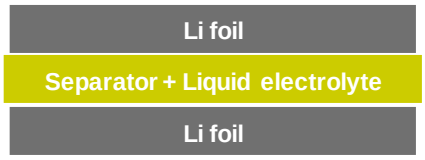

(c) *Li vs Li*

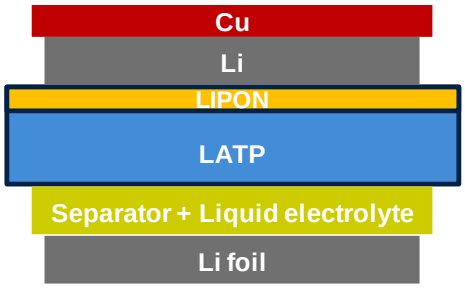

(d) *Protective layer*

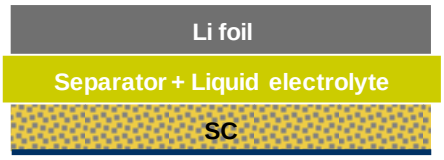

(e) *Standard SC vs Li*

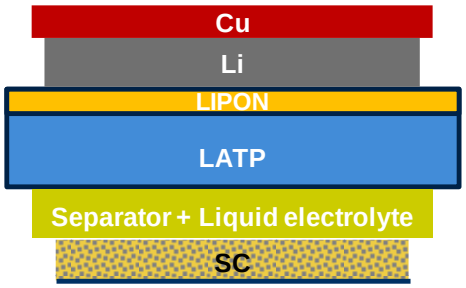

(f) *Hybrid SC vs Li*

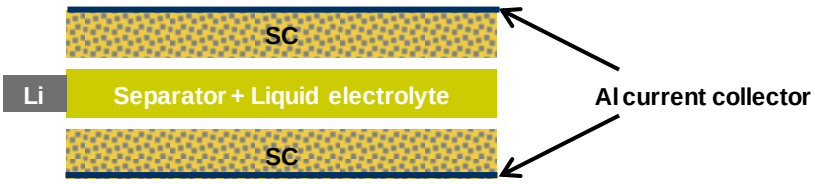

(g) *SC vs SC*

Illustration 3.1 All configurations of test cell assembly (a) to (g)

Table 3.1 Cell denotations, configurations, and constituents of all the cell assemblies.

Denotation	Test Cell	Positive Electrode	Separator(s)	Amount of liquid electrolyte (µL)	Negative Electrode
Au-LATP	EL cell	Au, Sputtered	LATP	---	Au, Sputtered
Liquid-LATP	EL cell	Steel (EL cell surface)	Fleece +LATP+Fleece	2 x 5	Steel (EL cell surface)
Li vs Li	EL cell	Li metal foil	Celgard+Fleece +Celgard	10	Li metal foil
Protective layer	EL cell	Li metal foil	Celgard+Fleece +LATP+LiPON	5	Li metal
Standard SC vs Li	EL cell	SC electrode	Fleece+Celgard	15	Li metal foil
Hybrid SC vs. Li	EL cell	SC electrode	Celgard+Fleece +LATP+LiPON	15	Li metal
SC vs SC	Swagelok cell	SC electrode	2 x Fleece at SC Fleece+Celgard at Li	30	SC electrode

3.3 Electrochemical Tests

3.3.1 Galvanostatic Cycling

Cycling of the test cells was executed by using a battery-test equipment of BaSyTec CTS. For the combined cycling and EIS measurement, Gamry Interface 1000 was utilized. Before cycling, assembled test cells were allowed relaxing for 15 minutes. The C-rate or imposed current is calculated on the basis of an electrode loading (area specific capacity) of 2 mAh/cm^2; thus, 1 C

is equal to 2 mA/cm^2. The voltage window is set between 1.3 (discharge) to 2.6 (charge) V. The limit of the voltage is to prevent oxidation reactions of liquid electrolyte at sulfur-carbon electrode during charge process and reduction reactions when discharge. The details of cycling parameters for each cell assembly can be found in Table 3.2. Cycling at each C-rate of the *standard* and *hybrid SC vs. Li* cells was preformed with three and five cells, respectively, in order to ensure the reproducibility.

3.3.2 Cycling of *SC vs. SC* Cells

As can be seen in Illustration 3.2, the positive SC electrode in the *SC vs. SC cells* was discharged against the reference Li metal, which was connected as the negative electrode in order to introduce lithium inside the *SC vs. SC* system. This first lithiation lasted for 20 h (also limited voltage not lower than 1.3 V) with the current density of 0.1 mA/cm^2 or equivalent to C/20, where C is related to the average of the theoretical sulfur capacity of both SC electrodes. After that, the discharged SC electrode was re-connected to the negative electrode and the other SC was the positive electrode. The Li metal then became the reference electrode. Cycling between two SC electrodes was performed at the C-rate of C/5 (0.4 mA/cm^2). In addition, the voltage of each SC electrode was measured with respect to the Li metal, acting as a reference electrode, and controlled between 1.3 and 2.6 V. For instance, a discharge process would terminate when at least one the following conditions met: the voltage of the negative SC electrode was less than 1.3 V and that of the positive SC electrode was more than 2.6 V. For the charge process, the terminating conditions were converse from the discharge case. Four *SC vs. SC* cells were assembled and underwent the cycling test.

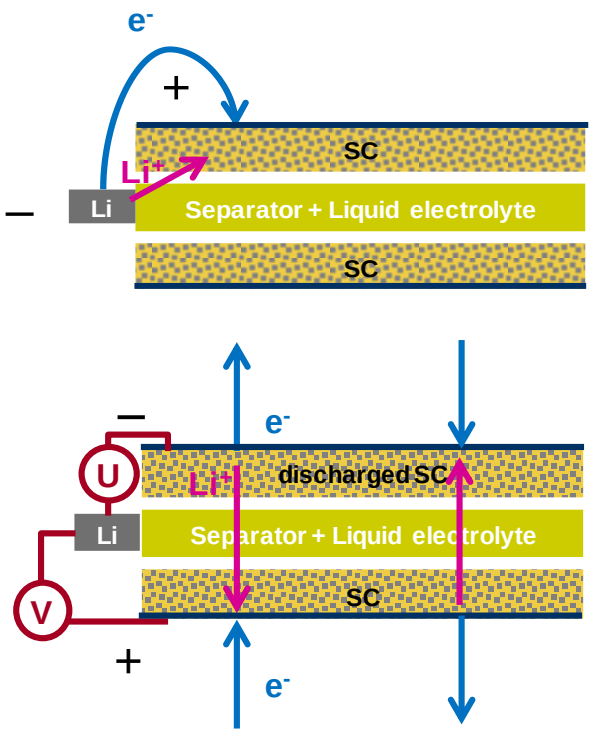

Illustration 3.2 A configuration of *SC vs. SC* cells during the first lithiation or discharge (upper) and further cycling (lower)

3.3.3 Cycling of Aged *Hybrid* Cells

To prove the existence of parasitic reactions of soluble sulfur and/or polysulfides at LATP, a direct interaction between the mentioned species has to be raised. Two aging conditions were then implemented on the *hybrid SC vs. Li* cells. By this, the *hybrid* cells were first assembled and let in open-circuit mode (without current flow) for 24 h of an exposure of soluble elemental sulfur in liquid electrolyte to LATP. Secondly, they were discharged and charged for 1 cycle at C/10. The polysulfides were subsequently delivered into liquid electrolyte phase to be in contact with LATP, see Illustration 3.3. Again, the cells containing polysulfides were switched to a relaxation mode of 24 h. Further cycling test was subsequently reinstated. The discharge capacity of the aged and unaged *hybrid* cells are compared with each other to

prove whether the parasitic reactions occurred. Two *hybrid* cells were assembled for this aging cycling.

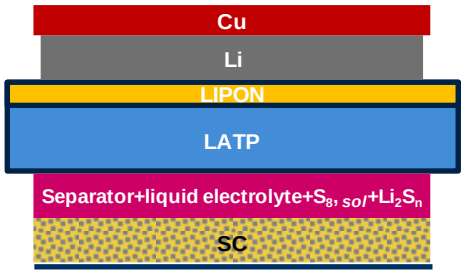

Illustration 3.3 A configuration of a *Hybrid SC vs. Li* cell under ageing condition with the presence of soluble sulfur ($S_{8,}$ *sol*) and polysulfides (Li_2S_n)

Table 3.2 Cycling parameters of all the cell assemblies

Cell	C-rate	Current (mA/cm^2)	Voltage limit (V)	Time limit (h) for each discharge and charge	Relaxation time between discharge and charge (min)
Au-LATP	No cycling				
Liquid-LATP					
Li vs Li					
Protective layer	C/10	0.2	-0.5 – +0.5	10	2
Standard SC vs Li	C/5, C/10	0.4, 0.2	1.3 – 2.6	---	2
Hybrid SC vs Li	C/10	0.2	1.3 – 2.6	---	2
SC vs SC	C/5	0.4	1.3 – 2.6[a]	---	2

[a] voltage measured from both SC electrodes vs. Li reference

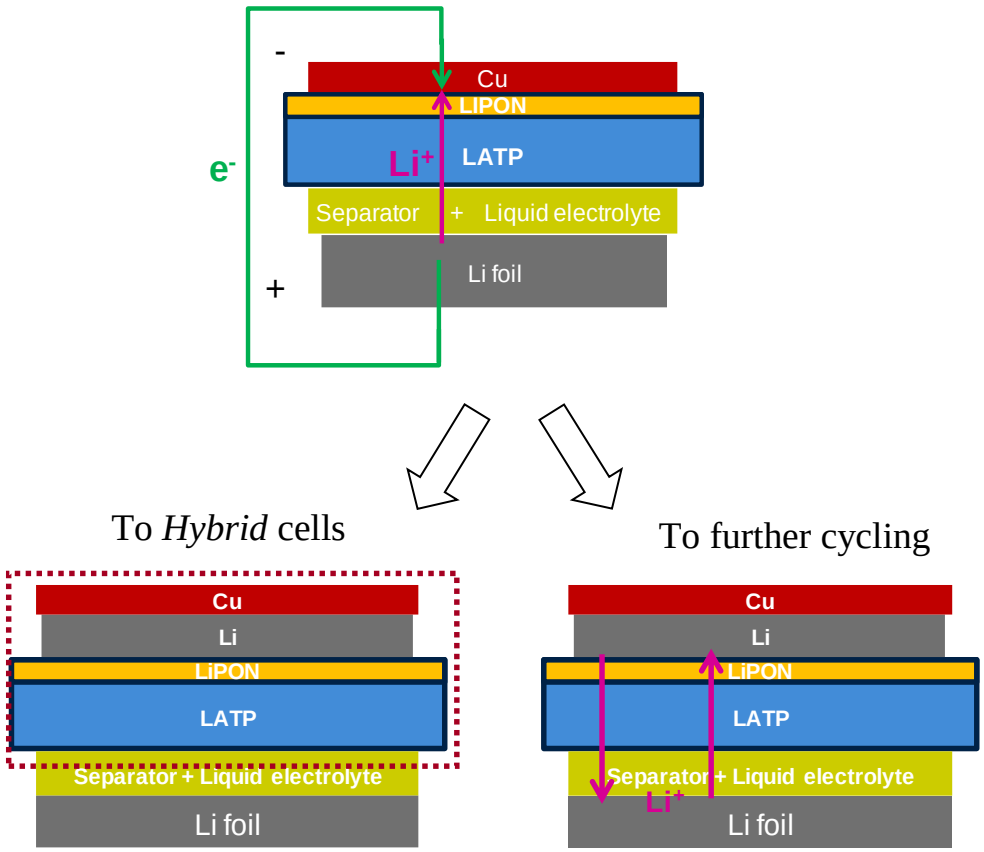

Illustration 3.4 A *protective layer* cell at initial state (upper) and after the first electrchemical deposition of lithium metal in between Cu and LiPON (lower)

3.3.4 Cycling of *Protective Layer* Cells

After LiPON and Cu were sputtered on a LATP plate, a metallic lithium layer was inserted in between Cu and LiPON by electrochemical deposition with a current density of 0.23 mA/cm^2 for 15 h. This process is termed as the first deposition, see Illustration 3.4. The resulting Cu-Li-LiPON-LATP composite is ready to be used in the *hybrid SC vs. Li* cells. The total capacity at least 3.45 mAh/cm^2 is obtained after this first lithium deposition. The lithium metal capacity of 3.45 mAh/cm^2 is already in excess of the sulfur capacity of 2.3 mAh/cm^2 at the sulfur-carbon electrode. Cycling of two *protective*

layer cells is continued by consecutively extracting and re-depositing lithium. The value of the current flow remains the same at 0.23 mAh/cm^2, but both extraction and re-deposition times are reduced to only 10 h. The voltage limit is -0.5 V for extraction and +0.5 V for (re-)deposition.

3.3.5 Electrochemical Impedance Spectroscopy

All the electrochemical impedance spectroscopy measurements were carried out by devices called Gamry Interface 1000 with a potentiostatic mode. During the measurement, the test-cells were situated in a temperature-controlled chamber at 23 °C. Before measuring impedance, a system or test- cell was allowed to relax at open-circuit mode for at least 15 min The applied voltage amplitude was 10 mV with respect to the open-circuit voltage (OCV) of a measured cell. The characterization underwent by sweeping a frequency of the input signal from 1 MHz to 100 mHz, which means nine decades in logarithmic scale. For each decade, ten different measured frequencies were applied. The measurement was carried out with a “Normal” mode. The cell assemblies that were measured the impeadance included *Liquid-LATP, Li-vs.-Li, protective layer, Au-LATP, standard SC vs. Li, and hybrid SC vs. Li.* The number of the measured cells of each cell assembly is shown in Table 3.3

Table 3.3 Cycling parameters of all the cell assemblies

Cell	Number of cell undergoing impedance measurement
Au-LATP	2
Liquid-LATP	3
Li vs Li	3
Protective layer	3
Standard SC vs Li	2
Hybrid SC vs Li	2
SC vs SC	None

3.4 Microstructural Analysis

Only electrochemical characterizations are not able to cover all the necessary information to explain the alteration originating from the cell components, e.g. LATP or lithium metal. Microstructural analytics like Scanning Electron Microscope (SEM) and X-ray Photoelectron Spectroscopy (XPS), also known as Electron Spectroscopy for Chemical Analysis (ESCA) can provide complementary information. SEM was used to visualize the structural and microstrucral pictures of the lithium metal at the LiPON interface. The SEM instrument was a “Leo Gemini 1530” from ZEISS. During the analysis, the voltage of 5 kV to accelerate the electron beam was used and the back-scattered-electron detector was applied. Elemental compositions and chemical states at the surface of the LATP plate after in contact with soluble sulfur and polysulfides were analyzed by XPS. The X-ray photoelectron spectrometer for the XPS analysis is a “PHI Quantera SXM™ - Quantum 2000 Scanning ESCA Microprobe” from PHSICAL ELECTRONICS. The XPS-spectra were collected using monochromatic Al-Kα X-ray radiation.

For the analysis with SEM, the Cu-LiPON-LATP plate was removed from the *protective layer* cells after the cycling test. It was wiped out on the LATP surface by tissue paper with some drops of 1,2-dimethoxyethane (DME) to clean it from the residual lithium salt, which can be reactive to the electron beam. Subsequently, the plate was left inside the glovebox overnight to ensure complete evaporation of the solvent. It was cracked with hand to obtain a fracture surface, and fixed on an adjustable sample holder with a piece of conductive carbon tape, see Illustration 3.5. An air- locked chamber was used to transfer the sample from the glovebox to a vacuum chamber of the microscope. Under the vacuum atmosphere in the order of 10^{-6} Torr, the SEM pictures were recorded by scanning the whole area of samples with the magnifications of 300 X, 1.0, 2.0, 5.0, and 10.0 kX.

From the aged *hybrid SC vs. Li* cells after the first charge, the LATP plates were in contact with soluble sulfur and polysulfides in liquid electrode for more than 24 h. Before proceeding for the XPS analysis, the composite LATP plates were likewise removed the cells. Then it was cleaned by a DME-soaked tissue paper and dried inside the glovebox, followed by transferring via an air-proof chamber into an XPS-analyzing chamber. After the ultrahigh vacuum around 10^{-8} Torr had been reached, the analyzed areas at the surface of the LATP plates were selected and irradiated by X-rays to create photo-electronfrons, see Illustration 3.6. The emitted electrons can be further detected and gave the information about the elemental compositions and the correlated binding energies. Three different analysed areas for each sample were performed to have the collective results. The diameter of an analysed area was 200 µm. As the penetration depth of the X-rays for the XPS analysis is 5 nm, the XPS results were obtained from the surface of the samples to the corresponding depth.

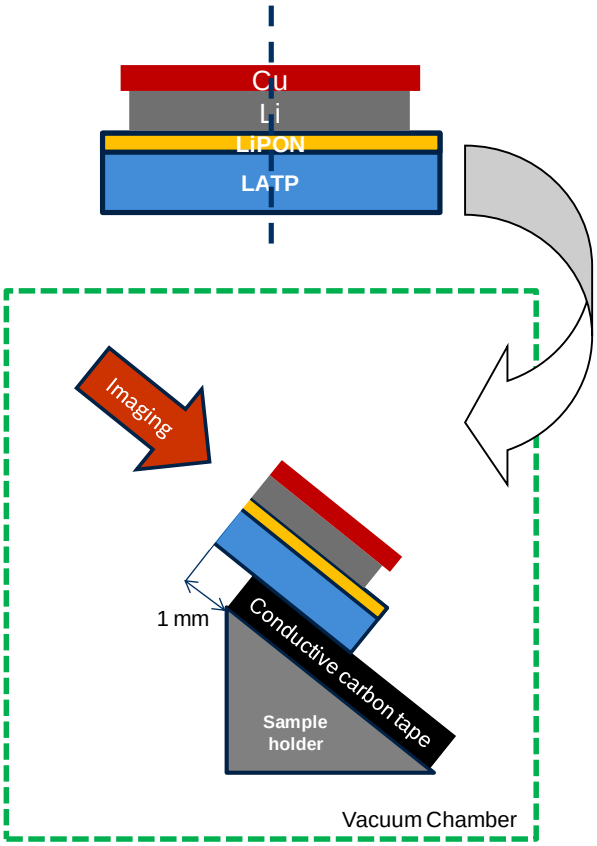

Illustration 3.5 Preparation and Configuration of a cracked Cu-Li-LiPON-LATP plate for SEM

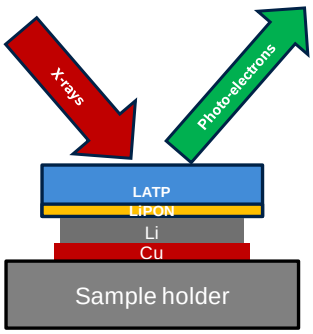

Illustration 3.6 Configuration of a Cu-Li-LiPON-LATP plate for XPS

4 Results and Discussion

4.1 Discharge & Charge Curves of *Hybrid* & *Standard* Cells

The voltage profiles at C/10 during discharge and charge as a function of the specific capacity with respect to the total mass of the sulfur-carbon electrode layer (sulfur + carbon black + binder) of the *standard* and *hybrid SC vs Li* battery cells can be seen in Figure 4.1. On the whole, both the *standard* and *hybrid* lithium-sulfur batteries exhibit the analogous voltage profile as expected with two distinctive plateaus corresponding to two main reduction reaction steps of elemental sulfur and polysulfides, respectively as specified in section 2.1.

In fact, since at the beginning after assembly, both cell configurations (*standard* and *hybrid*) expose the significant discrepant initial open-circuit voltages measured for 5 min, see Figure 4.2. The OCV of the *hybrid* cells go up around 2.7 V, yet that of the *standard* cells stand at 2.4 V.

The presence of different forms of the active sulfur species in each system after cell assembly might contribute to these phenomena. In case of the *standard* cells, there is molecular S_8 ring in both solid and liquid phase as mentioned in section 2.1, whereas in the *hybrid* systems more reactive sulfur species with higher potential versus Li^0/Li^+ is probably formed. According to [Weber 2014], molecular S_8 ring can be dissociated into S_6 to S_2 by Ti of $Li_7Ti_5O_{12}$, which is also a Li-ion conductor. In parallel, Ti of LATP plate in the *hybrid* cells is likely to create such a more-reactive sulfur, as well.

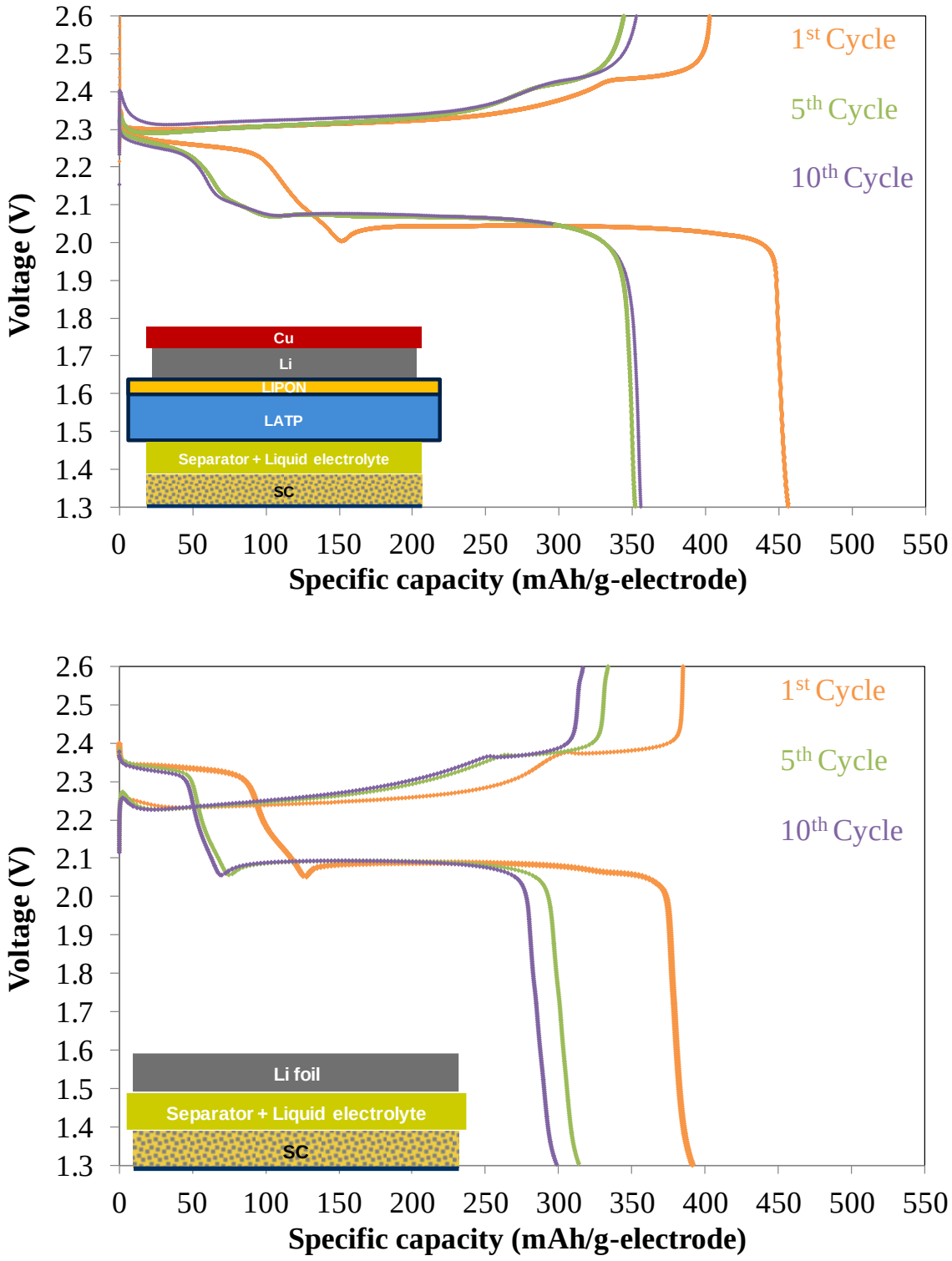

Figure 4.1 Discharge and Charge curves with C/10 at 1st, 5th, and 10th cycle of a *hybrid SC vs. Li* (upper) and a *standard SC vs. Li* cell (lower).

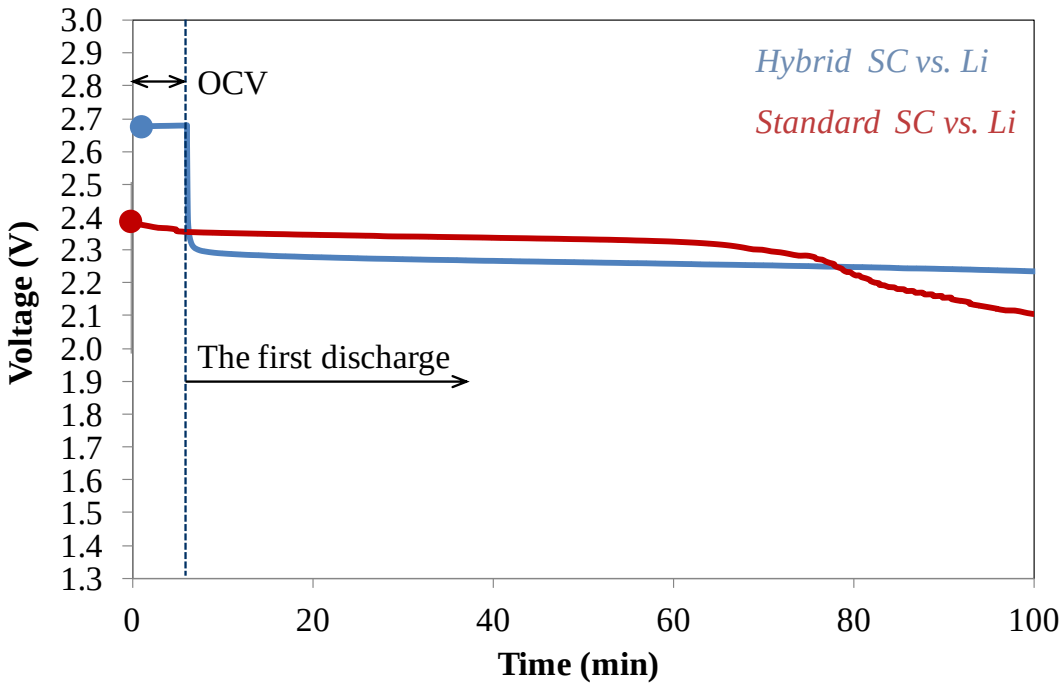

Figure 4.2 The initial OCV before the first discharge and a part of the first discharge curve vs. time of the *hybrid* and *standard SC vs. Li* cells

Table 4.1 Summary of the discharge capacity at the upper and lower plateau of the *hybrid* and *standard SC vs. Li cells* from Figure 4.1

Cycle	*Hybrid SC vs. Li*		*Standard SC vs. Li*	
	Discharge capacity (mAh/g-electrode) at the plateau(s)			
	Upper	Lower	Upper	Lower
First	96	283	76	235
Fifth	48	230	48	230
Tenth	48	230	48	203

The possible ring-opening of S_8 in the *hybrid* cells is supposed to occur just at the LATP surface, where soluble S_8 can reach via the liquid-electrolyte phase. This effect consumes a minority of soluble elemental sulfur during the initial relaxation time of 15 minutes. The existence of elemental S_8 in the *hybrid* system is evidenced by the presence of the upper plateau in the first discharge. The discharge upper plateau regardless of *hybrid* or *standard* cells is governed by the reduction reactions from elemental sulfur (S_8^0) to octa-sulfides (S_8^{2-}).

The capacities at the first, fifth, and tenth cycles attributed from the upper and lower plateau of the discharge curves in both *hybrid* and *standard* cells are summarized from Figure 4.1 in Table 4.1. The capacities at the plateaus are taken on the basis of the length of the plateaus. By comparing the first discharge capacities of the *hybrid* and *standard* cells, the higher capacity in the *hybrid* cell is observed. Thus, it can be pointed out that elemental sulfur in the *standard* cells is lost to the parasitic reactions with the Li-metal electrode.

Either in the *hybrid* or *standard* cells, the upper-plateau capacities of the tenth and the fifth discharges are equal, although they are lower than that of the first discharge. This implies that a limited amount of elemental sulfur can be oxidized back from polysulfides during the first (re-)charging process. According to the first charge curve of the *hybrid* cell, it also supports the possibility of this limitation, since the (re-)charge capacity is lower than the first discharge one. In case of the *standard* cell, the limitation of re-converting polysulfides back to elemental sulfur seems not the case because the capacity of the first charge is identical to that of the first discharge. The occur-

rence of the shuttle mechanism of polysulfides as depicted in Figure 2.2 results in the apparent elevated charge capacity rather than the actual capacity delivered from the lithium – sulfur cells. At the fifth and the tenth cycles of the *standard* cell, this phenomenon is even more obvious; the charge curves lead to higher capacity than the discharge ones in Figure 4.1. The shuttle mechanism is, in brief, the result of the diffusion of the polysulfides in the liquid electrolyte, along with the repetition of the electrochemical and chemical reactions of the long-chain and short-chain polysulfides occurring in the sulfur-carbon electrode and at the surface of the lithium metal demonstrated in eq. 2.12, 2.14, and 2.15.

From Table 4.1, the capacities at the lower plateau in the *standard* and *hybrid* cell assemblies become smaller in the fifth and the tenth discharges, respectively, when compared to that of the frist discharge. Correlatively, there must be a loss in the discharge capacity that goes through irreversibly parasitic reactions of soluble sulfur and polysulfides in the liquid electrolyte phase with lithium metal in the standard cells or LATP in the *hybrid* cells. Another reason that is able to provoke the diminution of the lower plateau capacity is that some of the lithium sulfide (Li_2S) still remains on the surface of carbon-black particles after complete charge. As a consequence, carbon-black particles covered by Li_2S become no longer electrochemically active for the next cycles. In other words, less surface area of the carbon black particles lowers the net extent of polysulfide reduction reactions to precipitate Li_2S, and ultimately the discharge capacity after cycling to the fifth or tenth cycle is restricted.

4.2 Cycleability of *Hybrid* and *Standard* Cells

Galvanostatic cycling method was adopted to test the performance of lithium-sulfur batterie, at which it involved imposing a constant current during discharge and charge. The cycling-test conditions for both the standard and hybrid set-ups were identical, see section 3.3. The cycleability information is represented with the discharge capacity as a function of the cycle number in Figure 4.3.

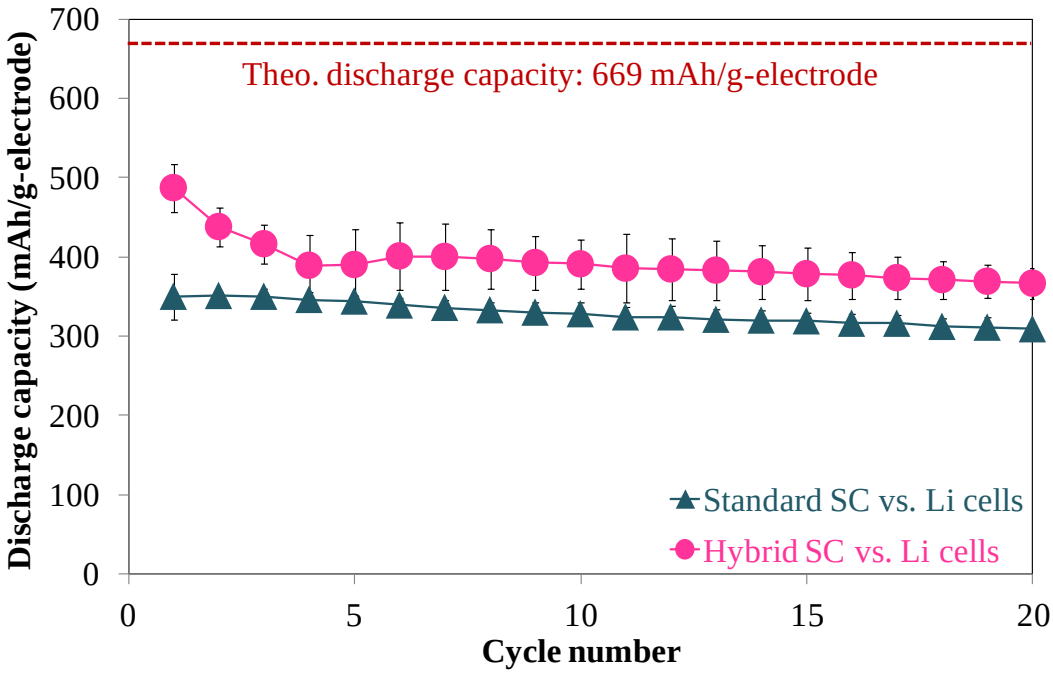

Figure 4.3 Discharge capacity (mAh/g-electrode) vs. cycle number of *hybrid* and *standard SC vs. Li* cells via cycling at 0.2 mA/cm^2 (C/10) between 1.3 and 2.6 V.

The *standard SC vs. Li* cells show a first discharge capacity of 350 ± 25 mAh/g, approximately which can be converted to a sulfur utilization of 52 % from the theoretical capacity of 669 mAh/g. For the *hybrid SC*

vs Li cells, the average first discharge capacity improves up to 500 ± 20 mAh/g equivalent to 75 % sulfur utilization.

One explanation of the sulfur utilization less than 100 % can be the loss of active sulfur species due to the irreversible parasitic reactions during the first discharge with lithium metal for the *standard* cells, or with LATP for the *hybrid* ones. The limitation of the surface area of carbon-conductive matrices (carbon black) can be another issue governing the low utilization of sulfur. After the first discharge, the solid discharge product of Li_2S precipitates and covers the carbon-black particles. This non-electronically-conductive compound, which is also non soluble in the liquid electrolyte, prohibits the further reduction reactions of polysulfides by blocking the accessibility of polysulfides to electrons.

As long-term cycleability of the *standard* cells, their discharge capacity steadily declines from the first until the twentieth cycles. One of the capacity fading problems originates from the continuous irreversible parasitic reactions between lithium metal and active sulfur species. Secondly, there is accumulation of lithium sulfide depositing on carbon-blacks surface. Last but not least, matrices of carbon black and binder can collapse. The difference in bulk densities of solid S_8 (2.07 g/cm^3) and solid Li_2S (1.66 g/cm^3) [Sigma-Aldrich] causes volume expansion and shrinkage of the sulfur-carbon electrode during the discharge and charge processes. Subsequently, the collapse of the electrode is possible. If the last two phenomena occur, the electrical contact in the electrode, e.g. between carbon-black particles, carbon-black and binder, electrode layer and current collector, will deteriorate and increase the cell resistance.

Though the first discharge capacity of the *hybrid* cells is enhanced and higher than that of the *standard* cells, Figure 4.3 illustrates a rapid drop in the capacity from the frist and the fourth cycles, followed by a further constant decrease until the twentieth cycle. This capacity decrease in the *hybrid* cells, but not noticed in the *standard* cells, is connected with either the interactions of soluble sulfur and/or polysulfides to LATP, and/or the dynamic process of depositing and extracting the lithium metal between LiPON and Cu layers of the protective plate-Cu-Li-LiPON-LATP.

4.3 Capacity Fading Investigations

In summary, three possible phenomena of the discharge-capacity fading linked to different constituents in the *hybrid SC vs. Li* cel configuration, see Illustration 3.3, are as follows:

- Deterioration of the electrical contact of the carbonaceous conductive matrix in the composite sulfur-carbon electrode owing to the structural collapse and/or accumulation of Li_2S,
- Degeneration of electrical contact between lithium metal and LiPON layers related to the interfacial alteration between Li and LiPON,
- Loss of active sulfur species (soluble sulfur and polysulfides), together with Degradation of LATP, due to the parasitic reactions at the interface between LATP and Liquid electrolyte.

By carrying out further cell assemblies and investigations to verify the assumptive phenomena listed above, it would enable us to understand the capacity fading as well as ageing behavior of the *hybrid SC vs. Li* system, or more precisely to find out where they are located.

4.3.1 Cycling of *SC vs. SC* Cells

Symmetrical assembly for cycling *SC vs. SC* cells is intended to minimize the undesired reactions between soluble active sulfur-derivatives in the liquid electrolyte and lithium metal. It is also to inquire ageing aftermath that may occur associating with the sulfur-carbon electrode. Three-electrode configuration in Swagelok T-cell as shown in Illustration 2.1 (g), Figure 4.4 presents the first discharge using the reference lithium metal as the negative electrode. By this way, the first lithiation brings lithium-ions and electrons into the sulfur-carbon electrodes. The current density applied for 20 hours was 0.1 mA/cm^2 equivalent to C/20. The reason for implementing the relatively low current was to avoid the large Ohmic overvoltage as a result of the small effective area of the reference lithium metal electrode of 0.126 cm^2, when compared to the area of the sulfur electrodes of 0.785 cm^2.

The striking features of Figure 4.4 are no remarkable plateaux as in the *standard SC vs. Li*, and the continuous reduction in the voltages at both SC electrodes. The latter phenomenon results from the fact that not only sulfur from the sulfur-carbon electrode connected as the positive electrode was electrochemically reduced by lithium-ions and electrons, but sulfur from the other sulfur-carbon electrode, dissolved also into the liquid electrolyte phase and diffused to undergo the reduction reactions at the positive electrode. A very

high concentration of polysulfides was consequently present in the liquid phase, which disguises the system to become more single-phase-like and inclines the voltage plateaux. At the end of this lithiation, all elemental sulfur should be transformed to polysulfides and also lithium sulfide.

After that, the electrical connection was re-adjusted in order to have a current flow only between the two sulfur-carbon electrodes. The lithium metal became the reference electrode so that the voltages at both sulfur electrodes could be monitored and controlled, see Illustration 3.2.

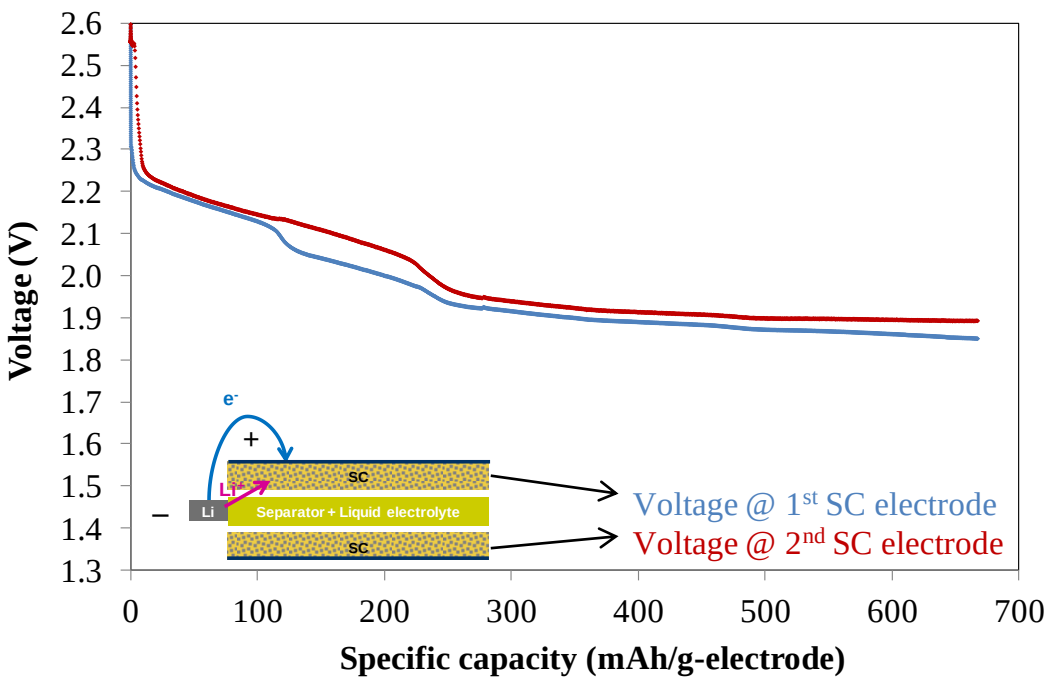

Figure 4.4 The voltage profiles at the first lithiation as a function of specific capacity of the *SC vs. SC* cells; the voltages of both SC electrodes measured vs. Li metal

Symmetrically cycling between the two sulfur-carbon electrodes was carried out. The current density was at 0.4 mA/cm^2 and the C-rate was C/5. The C-rate would be twice lower if taking into account the total sulfur capacity from the two sulfur electrodes engaging in the electrochemical reactions. That is

why the specific capacities of the *standard SC vs. Li* cells versus the cycle number at C/5 and C/10 are included in Figure 4.5 for comparison.

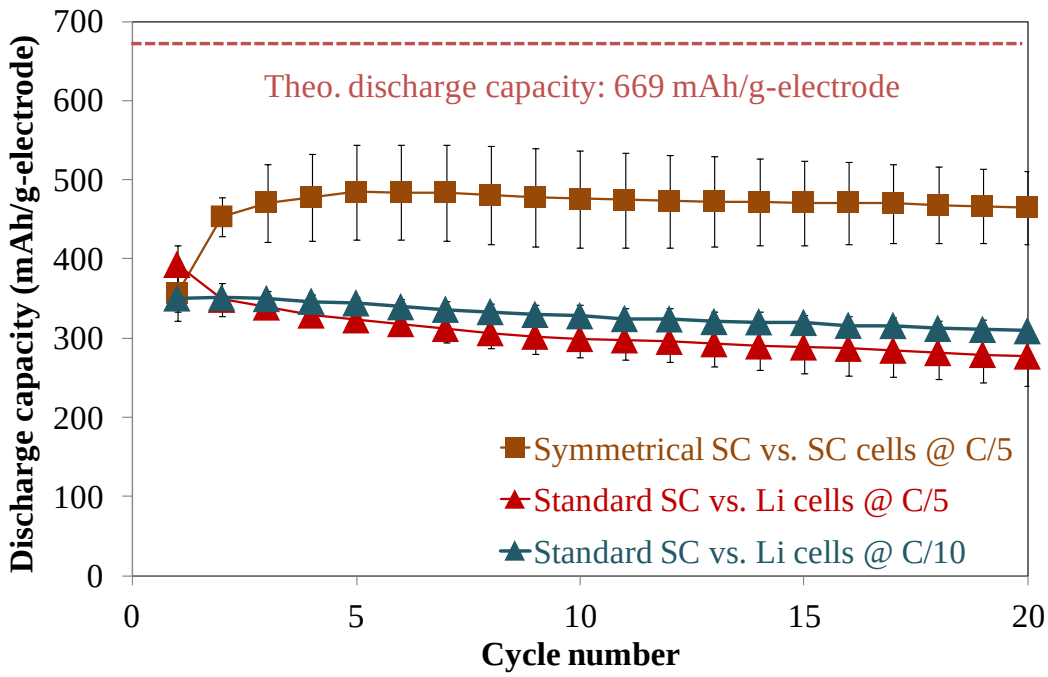

Figure 4.5 The curve of discharge capacity (mAh/g-electrode) vs. cycle number of the *SC vs. SC* cells at C/5 and the *standard SC vs. Li* cells at C/5 and C/10

The *standard* cells give a slightly higher the first discharge capacity at C/5 than those at C/10. Nonetheless, the *standard* cells at both C-rates display a downward tendency in the specific capacity.

According to Figure 4.5, the obtained capacity is comparably low at 350 mAh/g in the first cycle. It climbs up to 450 mAh/g in the second cycle before peaking at 500 mAh/g in the fifth cycle and leveling for the consecutive cycles. This maximum capacity of 500 mAh/g is corresponding to the first discharge capacity gained from the *hybrid* cells. Thus it indicates that the maximum sulfur capacity is controlled by the surface area of the carbo-

naceous conductive matrices in the sulfur-carbon electrode. When solid insulating Li_2S precipitates on and covers all the carbon black particles, further reduction reactions of polysulfides are no longer possible.

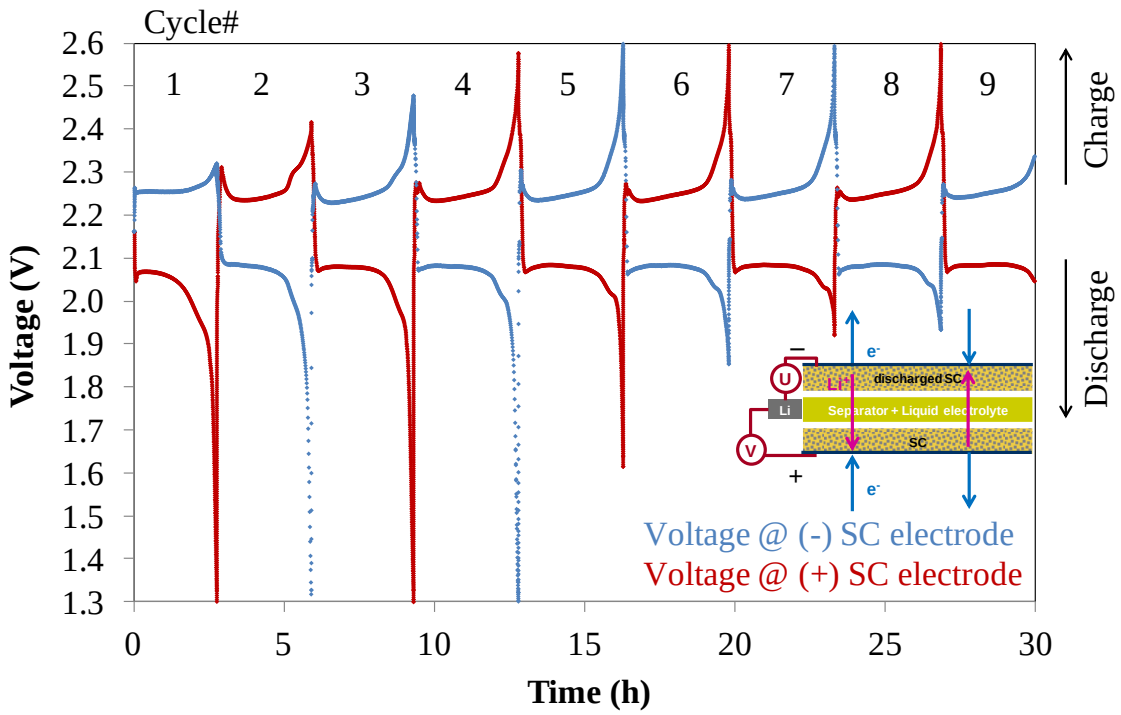

Figure 4.6 The time-dependent voltage profiles of a symmetrical *SC vs. SC* cell at the positive and the negative SC electrodes during cycling

For the low capacity of the symmetrical *SC vs. SC* cells during the first five cycles, it can be explained by the discharge and charge profiles from Figure 4.6. After the previous first lithiation, there is solid Li_2S that covers the carbon-conductive matrices in the sulfur-carbon electrodes. This solid Li_2S inhibits the electrochemical reactions in the sulfur-carbon electrodes. In other words, it limits the utilization of the sulfur capacity and leads to the obtained low capacity. The presence of Li_2S is ascertained by the sharp voltage decrease during the discharge from 2.0 to 1.3 V as in Figure 4.6. This sharp decrease in the voltage is also similarly present in the discharge curve of the

standard SC vs. Li cells, see Figure 4.1. Hence, the first five cycles of the the *SC vs. SC* cells serves as an activation step where Li_2S is re-oxidized back as polysulfides into the liquid electrolyte.

For the consecutive cycles, the voltage profile of the *SC vs SC* system is different from that of the *standard* one. The discharge curve shows only the lower plateau, followed by a short drastic voltage decrease or increase terminating before 1.3 V, see Figure 4.6. This termination is indeed governed by the charging process at the other sulfur-carbon electrode as its voltage increases constantly and instantaneously reaches 2.6 V, respectively. There is no clear explanation for these behaviors, but it seems to be involved in the different mechanisms in the formation of elemental sulfur and lithium sulfide on the electronically conductive carbonaceous matrices.

More importantly, no significant fading in the capacity of the symmetrical *SC vs. SC* cells is observed when either the capacity of the *standard SC vs. Li* cells cycled at C/10 or C/5 is used as a reference as in Figure 4.5. The resulting capacities of the *SC vs. SC* cells are quite scattered up to ±50 mAh/g-electrode which deviates from the arithmetic mean value of all the symmetrical cells. For this reason, the accumulation of Li_2S and the volumetric alteration during transition from S_8 to Li_2S or vice versa are minimal. These results in relatively low aging developed in the sulfur-carbon electrodes. Above all, the capacity fading appearing in the *hybrid SC vs. Li* cells is not regulated by the ageing effects occurring in the sulfur-carbon electrode.

4.3.2 Interface between Lithium metal and LiPON

The next part of the *hybrid SC vs. Li* to be considered responsible for the capacity fading is the lithium metal at the interface between LiPON and Cu layers. During the cycling of the *hybrid* cells, the lithium metal was extracted or deposited depending on discharge or charge, repeatedly. The interface between LiPON and lithium metal possibly does not maintain a good electrical contact after extraction (discharge) and deposition (charge) processes, inducing a rise in the total resistance of the cell. This rising resistance causes an extra loss in the voltage apart from the change of the redox potential of the electrochemical reactions. Subsequently it limits the discharge or charge capacities of the *hybrid* cells. For instance, providing that the cell resistance is 2000 $\Omega \cdot cm^2$ and the applied current density is 0.2 mA/cm^2, the voltage loss is amounted to 0.4 V.

A first attempt to assemble lithium metal with the protective layer (LiPON-LATP plate) chosen by direct pressing between lithium metal foil and LiPON-LATP plate did not deliver a good electrical contact for electrochemical tests, e.g. cycling or impedance measurement. Consequently, to solve this issue, Cu layer with 1-µm thickness as a current collector was sputtered on the LiPON side of the LiPON-LATP plate. After that, the resulting Cu-LIPON-LATP plate was assembled with separator, liquid electrolyte, and lithium metal foil as a test cell- *protective layer* cell at initial state, which is represented in Illustration 3.4. The cell was then available for the electrochemical Li-metal deposition, whereby the layer of Li metal was inserted in between Cu and LiPON. At the same time, a good electrical contact between LiPON and the Li metal was established.

4.3.2.1 Impedance measurement of LATP+LiPON

Before going into details of the cycling test, interrupted by impedance measurements of the *protective layer* cell, impedance measurements of the different cells of *Au-LATP*, *Liquid-LATP*, and *Li-vs.-Li* were first performed, to gain reference information for the data interpretation of the more complex system of the *protective layer* cell. All the impedance or resistance data in this section and the next sections are represented in the area specific dimension of $\Omega \cdot cm^2$, for which the electrode or current collector area was used as a factor.

All the types of the bulk, interface, blocking-interface, and diffusion contributions of each cell assembly related to fitting elements of an equivalent circuit from the EIS measurement are summarized in Table A.1, Table A.2, Table A.3 an dTable A.4 in Appendix.

Sputtering gold with the diameter of 7 mm on both sides of a LATP plate with the thickness of 155 µm gives a Au|LATP|Au configuration, which was assembled as a *Au-LATP* cell in an EL cell shown in Figure 4.7 and Illustration 2.1 (a). The obtained impedance spectrum (Nyquist plot) of the cell and the fitting curve with the equivalent circuit are shown in Figure 4.8. In the high- frequency region (1 MHz to 10 kHz), a depressed semi-circle shifted from the origin point(0,0) presents. This part of the spectrum was fitted with the serial combination of R_s and $R_1//CPE_1$.

From medium frequency of 10 kHz downward, a linear increase of the impedance is observed and was fitted with CPE_2. This behavior relates to the fact that the interface between Au and LATP act as a blocking interface where no charge carrier can cross over from LATP to the Au electrode or

vice versa. For this reason, R_s and R_1 are the total resistance of LATP exclusively connected to the lithium-ion conductivity on the condition that the electronic conductivity of LATP is theoretically too low to be measured when compared to the ionic one.

The specific effective capacitance of R_1//CPE_1 can be calculated from eq. 2.31 using the electric contact area (Au sputtered: 0.785 cm^2) and the LATP thickness The calculated capacitance value of 64 pF/cm is in between the orders of magnitude for bulk and grain boundary, see Table 2.2. Thus, R_1//CPE_1 should be the overlapping contributions between grain and grain boundary. According to a literature [Fu 1997], R_s was assigned for the grain contribution and R_1 was for the grain boundary.

The total Li^+ conductivity calculated by eq. 4.1 is 9.5 x 10^{-5} S/cm at 23 °C for the first measurement after cell assembly, which is just a little lower than 1 x 10^{-4} S/cm at room temperature, the reported value from OHARA GmbH [OHARA].

$$\sigma = \frac{1}{R} d \tag{4.1}$$

where R is the total resistance (R_s + R_1) of a LATP plate, and *d* is the LATP-thickness.

To verify the stabilities of LATP against sputtered gold, time-dependent measurements were performed and depicted with the conductivity as in Figure 4.9 and Figure 4.12. There is no significant alteration in the conductivity of 10^{-4} S/cm over a month, which confirms the LATP stabilities.

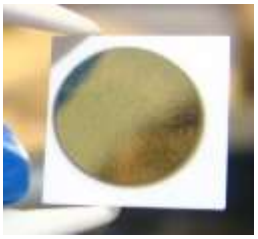

Figure 4.7 Gold sputtered as an electrode on a LATP plate

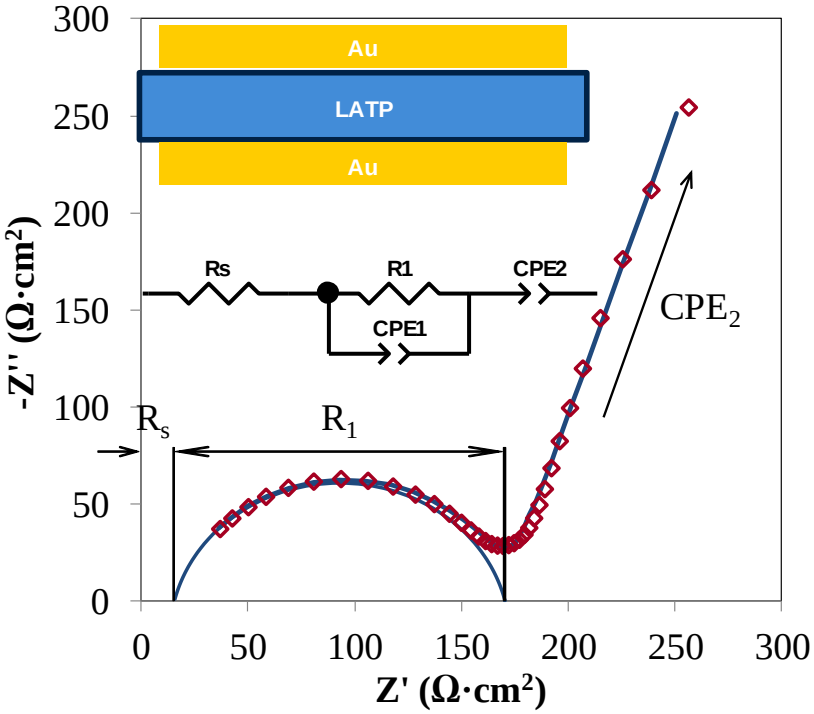

Figure 4.8 An impedance spectrum (red open symbol) and its fitting curve (blue line) of a *Au-LATP* cell, along with the used equivalent circuit

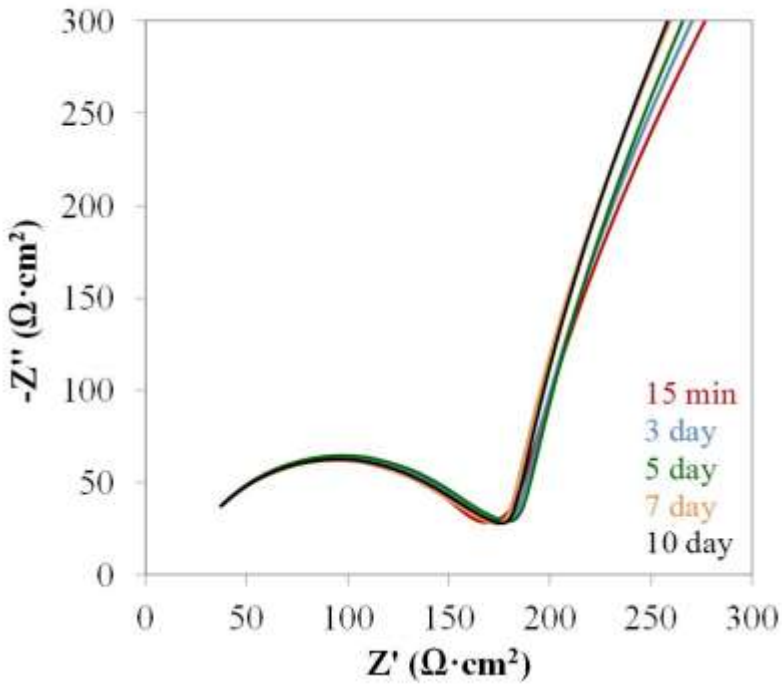

Figure 4.9 The impedance spectra of a *Au-LATP* cell measured at the different times after cell assembly

In order to determine the charge transfer resistance at the individual interfaces of the *protective layer* cells, reference cells, *Liquid-LATP* and *Li vs. Li*, have been assembled as shown in Illustrations 2.1 (b) and (c).

The impedance spectrum for a *Liquid-LATP* cell, is shown as a Nyquist plot in Figure 4.10. Four contributions, i.e. R_s, R_1//CPE_1, R_2//CPE_2 and CPE_3, of an equivalent circuit were used to fit the spectrum. R_s is obviously the total bulk resistance of liquid electrolyte and LATP. CPE_3 refers to the blocking-interface behavior between steel (EL cell surface) and the liquid electrolyte phase. The specific effective capacitance of R_1//CPE_1 is 66.3 ± 4.5 pF/cm calculated by using R_1, CPE-T_1, CPE-p_1, the electrical contact area (separator area) of 0.785 cm^2, together with the LATP-plate thickness of 155 µm. It indicates the possible overlapping between the bulk and the grain boundaries of LATP, which is matching with the value of 64 pF/cm from the *Au-LATP* cells.

The lower frequency contribution $R_2//CPE_2$ is assigned for the interface between liquid electrolyte and LATP plate. The effective capacitance of $R_2//CPE_2$, calculated using the fitting results of R_2, CPE-T_2, yields 1.9 ± 0.1 µF. By including the electrical contact area 0.785 cm^2 and the fact that there are two LATP|liquid electrolyte interfaces connected in series, the specific effective capacitance per area is 4.9 ± 0.3 µF/cm^2. Accordingly, R_2 is the charge transfer resistance and CPE_2 represents the electrical double layer at the interface between liquid electrolyte and LATP.

To estimate the Li-ion conductivity of LATP, the sum of R_s + R_1 resistances of 150 ± 8 Ω·cm^2, and the LATP thickness of 155 µm are taken into account in eq. 4.1. The obtained Li-ion conductivity of LATP amounts to around 1.0 x 10^{-4} S/cm, and matches the value reported by OHARA GmbH [OHARA]. It has to be noted that the small resistance of 3 Ω·cm^2 of the liquid-electrolyte resistance is neglected as it is relatively too small and does not change the order of the conductivity.

Another point to consider is the time-dependent stability of LATP against liquid electrolyte, which can be monitored by continuously measuring the impedance of the *Liquid-LATP* cells in a long term after cell assembly. The impedance spectra and the conductivity of LATP versus the time are shown in Figure 4.11 and Figure 4.12, respectively.

At the first measurement (15 min after cell assembly), the lowest resistance of R_1 and the respective highest conductivity of LATP are observed. After 3 days, the measured R_1 in Figure 4.11 relatively increases and the calculated conductivity decreases slightly. Reduction in the electrical contact area between liquid electrolyte and LATP due to partly vaporization of liquid electrolyte inside the test cell (EL cell) may explain this phenomenon. However,

this phenomenon should be already in equilibrium in the following measurements since there is no considerable change in either R_1 or the conductivity.

Moreover, the long-term conductivities of Li-ion in LATP resulting from the *Au-LATP* and *Liquid-LATP* cell assembies are in good agreement, both in the order of 10^{-4} S/cm. It can be concluded that LATP is stable against liquid electrolyte.

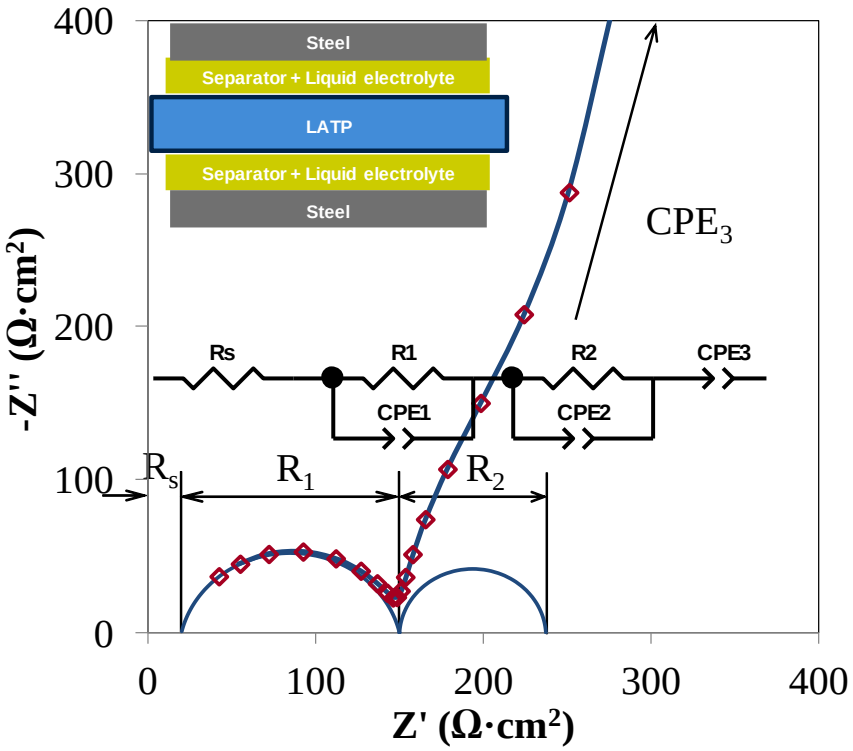

Figure 4.10 An impedance spectrum (red open symbol) and its fitting curves (blue line) of a *Liquid-LATP* cell with the corresponding equivalent circuit

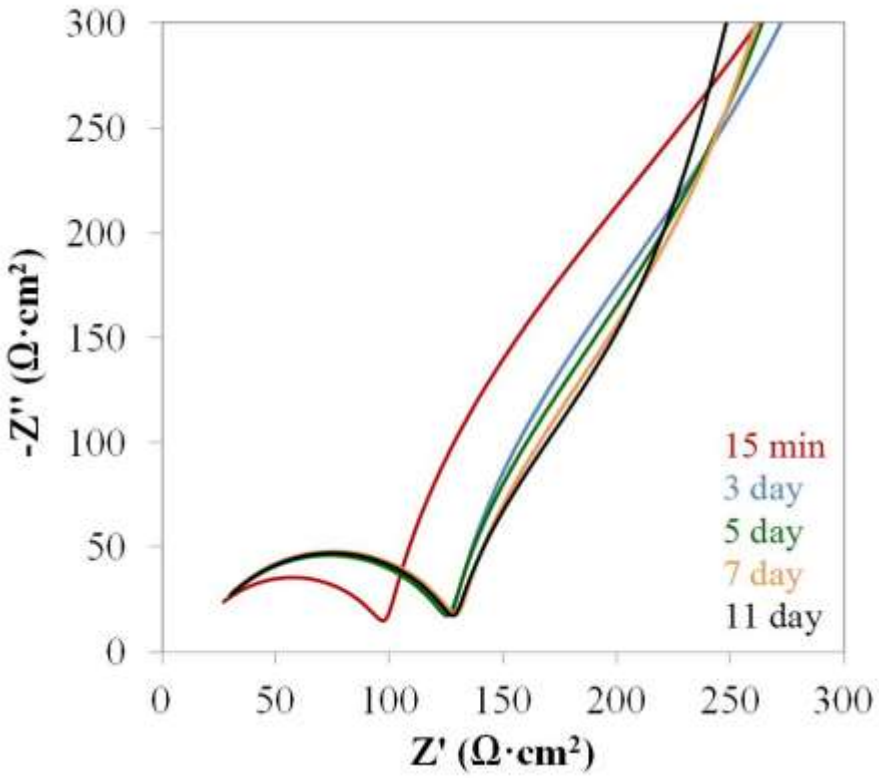

Figure 4.11 The impedance spectra of a *Liquid-LATP* cell measured at the different times after cell assembly

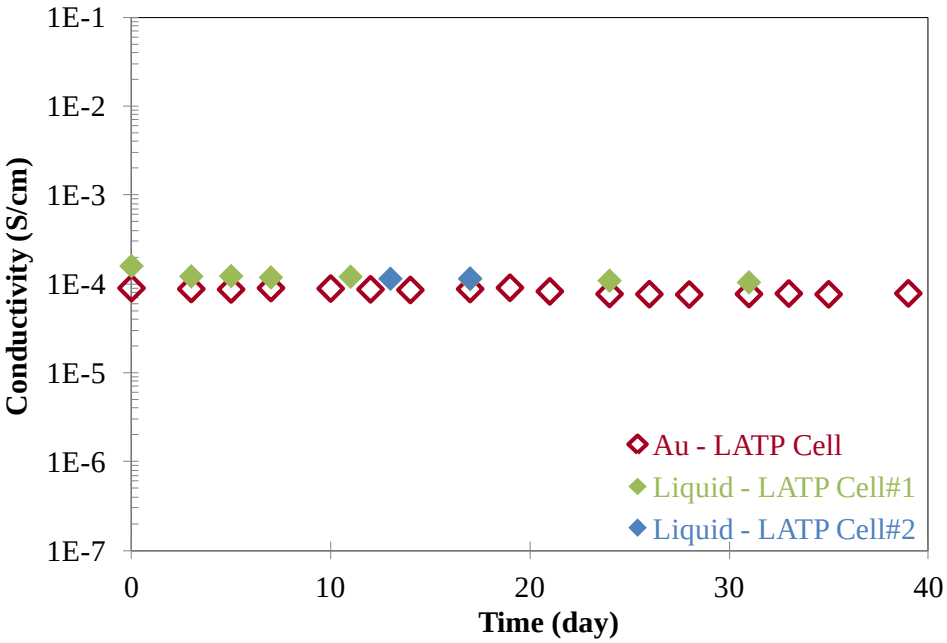

Figure 4.12 The Li-ion conductivity of LATP vs. time measured in the *Liquid-LATP* and *Au-LATP* cells

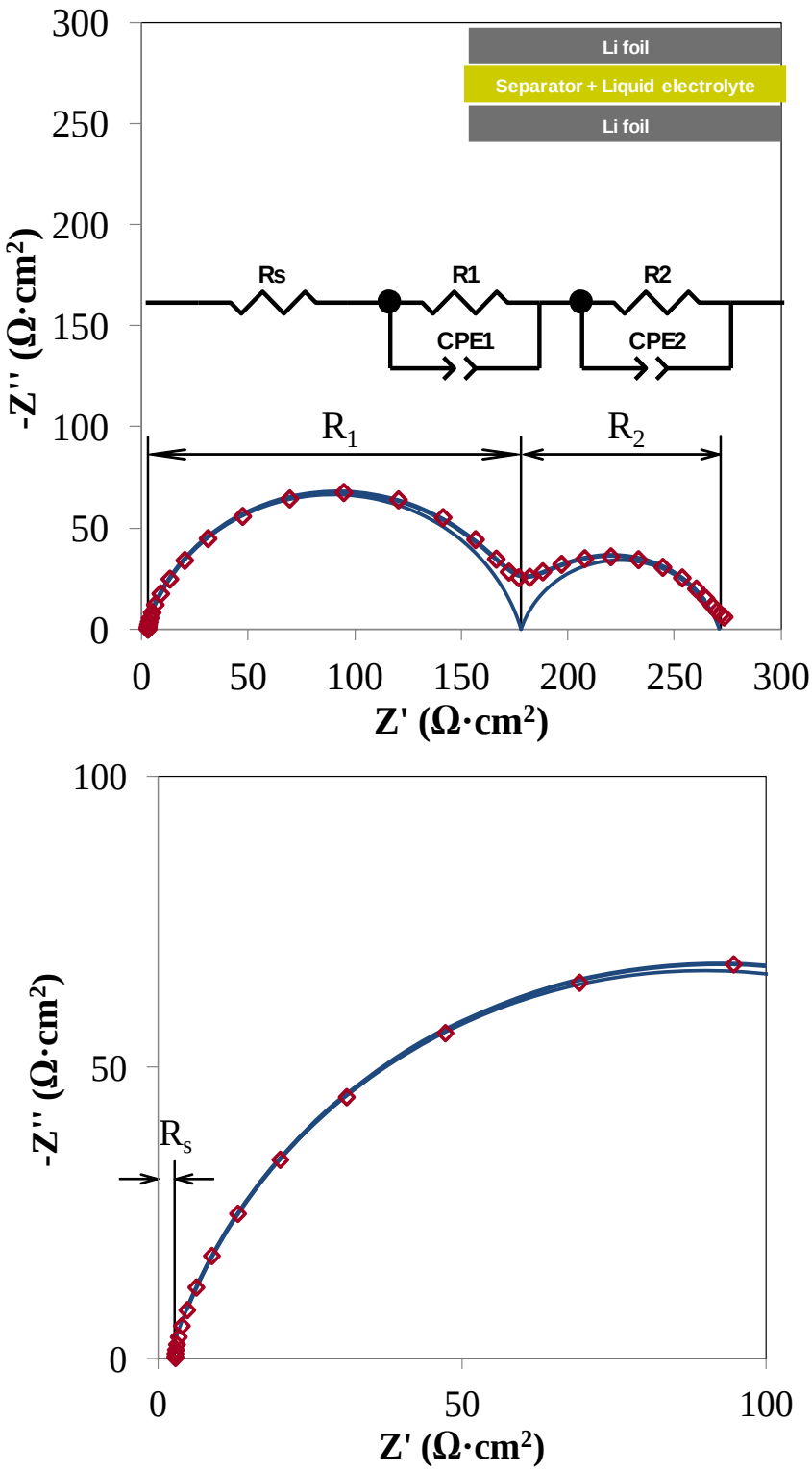

Figure 4.13 An impedance spectrum (red open symbol) and its fitting curves (blue line) of a *Li-vs.-Li* cell with the corresponding equivalent circuit (upper), and the close-up impedance data in the high-frequency region (lower)

The impedance data of *Li-vs.-Li* cells are shown as a Nyquist plot in Figure 4.13. The data were fitted with an equivalent circuit with three contributions: R_s, R_2//CPE_2, and R_1//CPE_1 can be found in Figure 4.13. The data analysis was done similarly to the cases of *protective layer* and *Liquid-LATP* cells. A relatively small serial resistance R_s due to liquid electrolyte with only 2.8 ± 0.3 Ω·cm^2 is found. The results after fitting the first semi-circle with R_1//CPE_1 gives the area specific effective capacitance of 1.9 ± 0.3 µF/cm^2 for one interface between liquid electrolyte and lithium metal foil.The second semi-circle contribution is represented with R_2//CPE_2. It leads to the effective capacitance of 0.7 ± 0.4 mF and the characteristic frequency of 3.9 ± 0.9 Hz.

The calculated specific effective capacitance from this contribution is 1.7 ± 1.0 mF/cm^2 (using the area of 0.785 cm^2). From Table 2.2, this capacitance is in the order of a surface charge or adsorbed species, which might be the solvent molecules or anions of $TFSI^-$ being adsorbed on the surface of the lithium metal foil. The value of the resistance R_2 is 59.7 ± 21.3 Ω·cm^2, which comes from a double surface of the lithium metal foil metal in contact with the liquid electrolyte in this symmetrical assembly. The resistance is thus reduced to 29.8 ± 10.7 Ω·cm^2 if there is one surface of the lithium metal foil as in the *protective layer* assembly.

The *protective layer* cells containing lithium metal in between Cu and LiPON after the first electrochemical deposition as in Illustration 3.1 (d), denoted with the configuration of Cu|Li|LiPON|LATP|L|Li foil underwent an impedance measurement. Since several components and interfaces co-exist, the impedance spectrum of this cell is a collective result of all the constituents.

According to Figure 4.14, the impedance spectrum was fitted with an equivalent circuit involving three different contributions: R_s, $R_1//CPE_1$, and $R_2//CPE_2$. R_s relates to the shift of the onset of the combined first ($R_1//CPE_1$) and second ($R_2//CPE_2$) depressed semi-circles from the origin point. It suggests the presence of bulk resistances of liquid electrolyte, LATP and LiPON. The effective capacitances of $R_1//CPE_1$ and $R_2//CPE_2$ are 2.55 ± 0.10 nF and 0.94 ± 0.14 µF, respectively. If taking into account the geometry factors, i.e. the total thickness of LATP and LiPON (158 µm), and the electrical-contact surface area (0.785 cm^2), the specific effective capacitances for $R_1//CPE_1$ is 51.3 ± 1.9 pF/cm. Likewise, the specific effective capacitance of $R_2//CPE_2$ is 1.2 ± 0.2 µF/cm^2 by considering only the surface area.

Comparing these specific values to those in Table 2.2, $R_1//CPE_1$ is attributed to the overlapping between grain and grain boundary phases of the LiPON-LATP composite layer. R_2 of $R_2//CPE_2$ is the total charge transfer resistance at all the interfaces since there are the interfaces between Li metal and LiPON, LiPON and LATP, LATP and liquid electrolyte, and liquid electrolyte and lithium metal foil. Meanwhile CPE_2 is the overall electrical-double-layer capacitances of all the referred interfaces.

In the lower frequency region (from 20 to 0.1 Hz) of the impedance results of the *protective layer* cell, where the effect of this surface-charge contribution is expected, see in Figure 4.14 (lower), the spectrum does not exhibit semi-circular pattern. It is accordingly not possible to extract the resistance of the surface-charge contribution due to the lithium metal foil in contact with the liquid electrolyte.

All the results regarding the impedance analysis on the *protective-layer*, *Liquid-LATP*, and *Li-vs.-Li* cells are summed up in Table 4.2. The interface contributions are in the frequency range from 800 to 1000 Hz. The sum of the resistances originating from between the interfaces between LATP and the liquid electrolyte (*Liquid-LATP*) of 40 ± 3 Ω·cm^2, and the lithium metal foil and the liquid electrolyte (*Li-vs.-Li*) of 89 ± 6 Ω·cm^2 is 129 ± 7 Ω·cm^2. In the *protective-layer* cells, the total interface resistance of 159 ± 17 Ω·cm^2 is found. Therefore, a residual interface resistance amounting to 30 ± 18 Ω·cm^2 is left over. It can be attributed to the interfaces between LiPON and LATP, LiPON and Li metal, or the combination of these two interfaces.

Table 4.2 Summary of all the contributions and resistances of the *protective layer*, *Liquid-LATP*, and *Li vs. Li* cells

Cell Configuration	Contribution: LATP (and LiPON) + liquid electrolyte			Contribution: Interface		
	$C_{spec.}$ (pF/cm)	$R+R_s$ (Ω·cm^2)	f_c (kHz)	$C_{spec.}$ (µF/cm)	R (Ω·cm^2)	f_c (Hz)
Cu|Li|LiPON|LATP|L|Li *Protective layer*	51.3 ± 1.9	465 ± 26	109 ± 6	1.2 ± 0.2	159 ± 17	850 ± 66
Steel|L|LATP|L|Steel *Liquid-LATP*	66.3 ± 4.5	150 ± 8	294 ± 6	4.9 ± 0.3	40 ± 3	810 ± 20
Li|L|Li *Li vs. Li*	---	Rs: 2.8 ± 0.3	---	1.9 ± 0.3	89 ± 6	990 ± 129

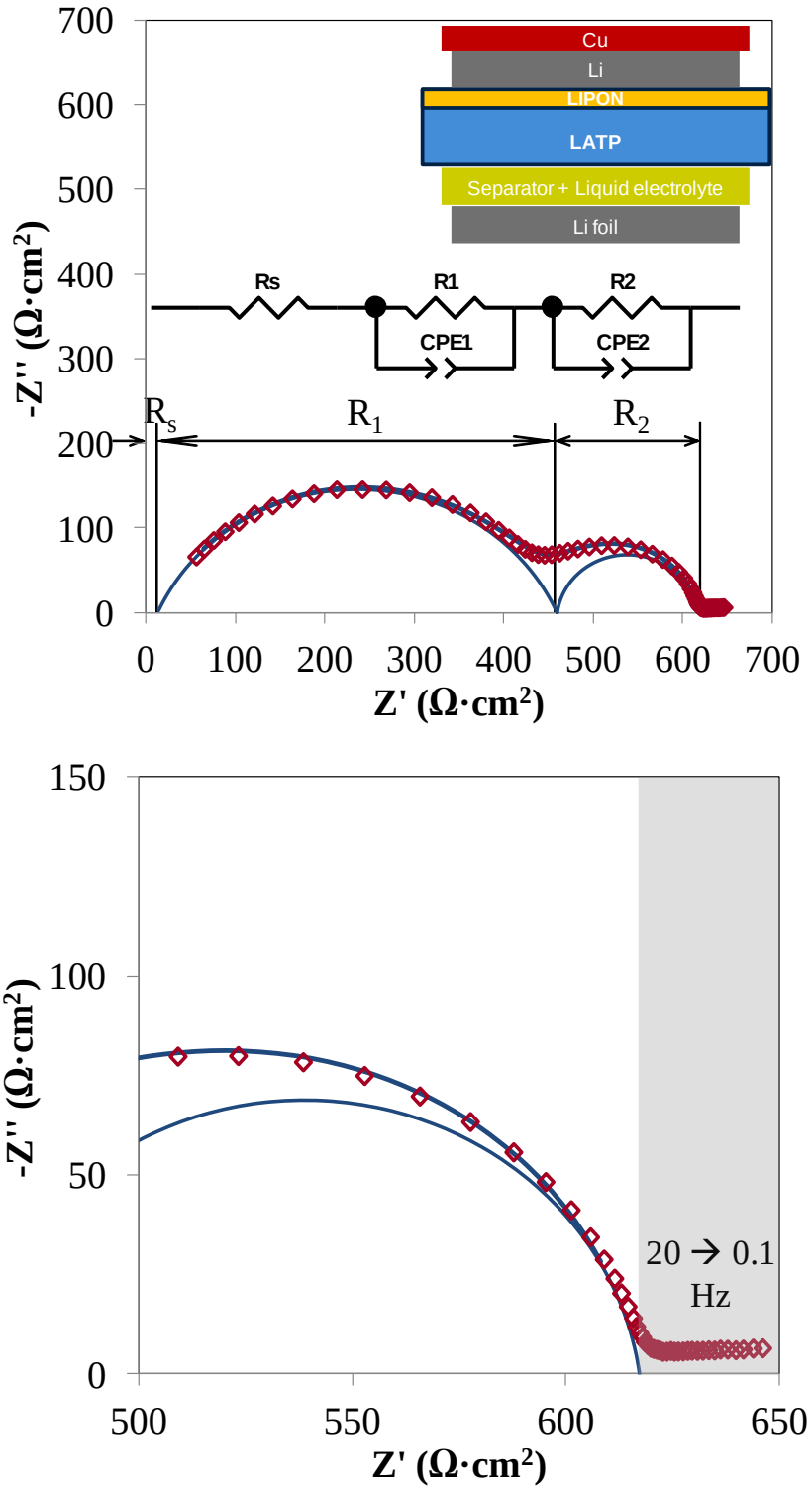

Figure 4.14 An impedance spectrum (red open symbol) and its fitting curves (blue line) of a *protective layer* cell with the corresponding equivalent circuit (upper), and the close-up impedance spectrum in the region from 20 to 0.1 Hz (lower)

4.3.2.2 Cycling & Impedance measurement of *Protective Layer* Cells

Cycling tests of *protective layer* cells were performed to examine the degradation at the interface between LiPON and Li metal as located in Illustration 3.4 (lower). The lithium metal was iteratively electrochemically extracted from and (re-)deposited on the LiPON surface in the *protective layer* cells. This analogous procedure was also happening with the lithium metal in the *hybrid SC vs. Li* cells while being discharged and charged. The current density applied for the entire cycling was 0.23 mAh/cm^2, equivalent to C/10 in either the *hybrid* or *standard SC vs. Li* cells. The cell voltage was controlled between 0.5 and -0.5 V. The occasion that the voltage is positive corresponds to the deposition process; meanwhile, the negative voltage value is measured during the extraction process.

The voltage response during the extraction and deposition represented against the capacity from the first to the eleventh cycles is shown in Figure 4.15. After assembly, a Cu-LiPON-LATP plate with a piece of separator soaked with liquid electrolyte and a Li-foil disc in a cell as in Illustration 3.4 (upper), the cell OCV is lower than -1.7 V, because the Li foil was connected to the positive electrode and the Cu, which has a higher electrochemical potential than Li, was connected to the negative side.

The first deposition of Li metal at the interface between LiPON and Cu was accomplished by application of a current with the appropriate direction. The outcoming capacity after the first deposition of 15 h was *ca.* 3.45 mAh/cm^2.

Subsequently after the application of the current, the cell voltage soared up to +0.15 V before stabilizing for the rest of the deposition. The increase in the voltage is a result of the intrinsic resistances of the cell, which can be

divided into two categories: material and interface resistances, as in Table 4.2. The stable voltage infers that the Li-metal deposition undergoes a continuous film growth, which is confirmed by images taken by Scanning Electron Microscope (SEM), see section 4.3.2.3. At the end of the deposition, both sides of the negative and positive electrodes of the *protective layer* cell consisted of lithium metal. The OCV was thereby recorded to be 0.0 V.

Applying the current in the opposite direction for the first extract the lithium metal from the LiPON interface, the voltage drops to the negative value of -0.15 V. It has a flat pattern in common to the first deposition. The extraction period was 10 h and yielded the capacity of 2.3 mAh/cm^2. Hence, the first Li-metal deposition and extraction at the interface with LiPON are symmetrical in the resistance and kinetically reversible. Moreover, it is plausible that the lithium metal is able to maintain a good electrical contact with LiPON. Note that further Li-metal depositions as well as extractions were experimentally set to a duration of 10 h and at the same time had to fulfill the condition of the voltage limit. Up to the sixth cycle of the Li-metal deposition and extraction, all the voltage curves look almost identical and the capacity is obtained at 2.3 mAh/cm^2. The absolute values of the voltage during deposition and extraction increase slightly to nearly 0.2 V, referring to no significant change in the cell total resistances and also the contact between LiPON and the lithium metal.

Starting from the seventh cycle, there is a significant deviation at the extraction voltage plateau. In the seveth extraction, this deviation begins just at a capacity value of 2.0 mAh/cm^2, where the voltage decreases sharply from -0.2 to -0.3 V. In the eighth cycle, the voltage during the Li-metal extraction

is no longer flat. It deteriorates steadily and exceedes the limit of -0.5 V before the completion of the 10-h extraction process. The obtained capacity is reducted to 1.9 mAh/cm^2.

For the nineth and tenth extractions, the voltage curves drop to values lower than -0.5 V and around 0.8 mAh/cm^2 is reached. From the seventh to the eleventh depositions, though the voltage values substantially increase to more than 0.4 V, all the depositions have a plateau-like shape, and complete the capacity of 2.3 mAh/cm^2. This suggests that the electrical contact area at the interface between the lithium metal and LiPON is depleted, escalating the total cell resistance.

In the *protective layer* cells, lithium metal foil was assembled in contact with separators and liquid electrolyte. It is widely accepted that lithium metal is not chemically stable against liquid electrolyte [Aurbach 2000]. The continuous formation of solid electrolyte interphase (SEI) as well as dendrite formation give rises in the cell resistance and the chance of short-circuit, respectively. When the lithium metal at the LiPON interface is deposited or extracted, at the same time lithium metal is also extracted or deposited, respectively, at the interface between lithium metal foil and liquid electrolyte as in Illustration 4.1. The counter reactions at the lithium metal foil side lead to available lithium metal to react with liquid electrolyte. For this reason, cycling of symmetrical cells of *Li-vs-Li* was aimed to verify how significant the influence of the interaction of lithium metal with to liquid electrolyte. Two different assemblies of *Li-vs-Li* cells were used: one contained the combined separators of Celgard and Fleece and one has Fleece separator only. Note that in the *protective layer* cells, separators of Celgard and Fleece were used.

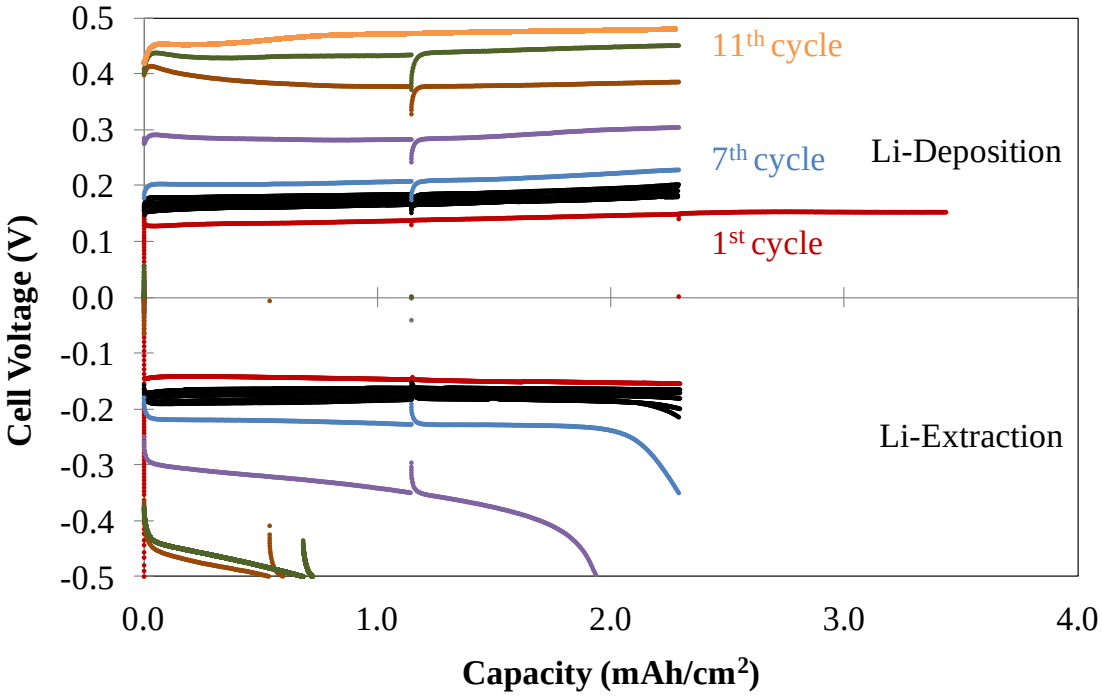

Figure 4.15 Voltage profile as a function of capacity related to the Li-metal deposition and extraction of a *protective layer* cell from the first to the eleventh cycles

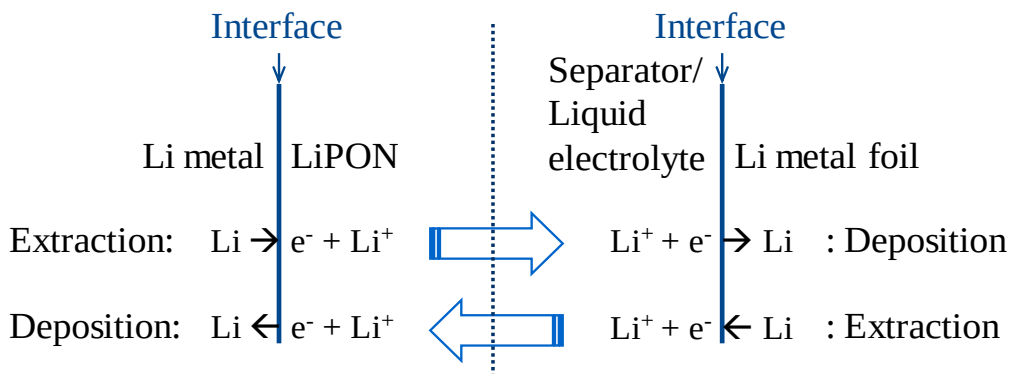

Illustration 4.1 The electrochemical reactions occurring at the interface between Li metal and LiPON, and at the interface between liquid electrolyte and lithium metal foilduring the extraction and deposition

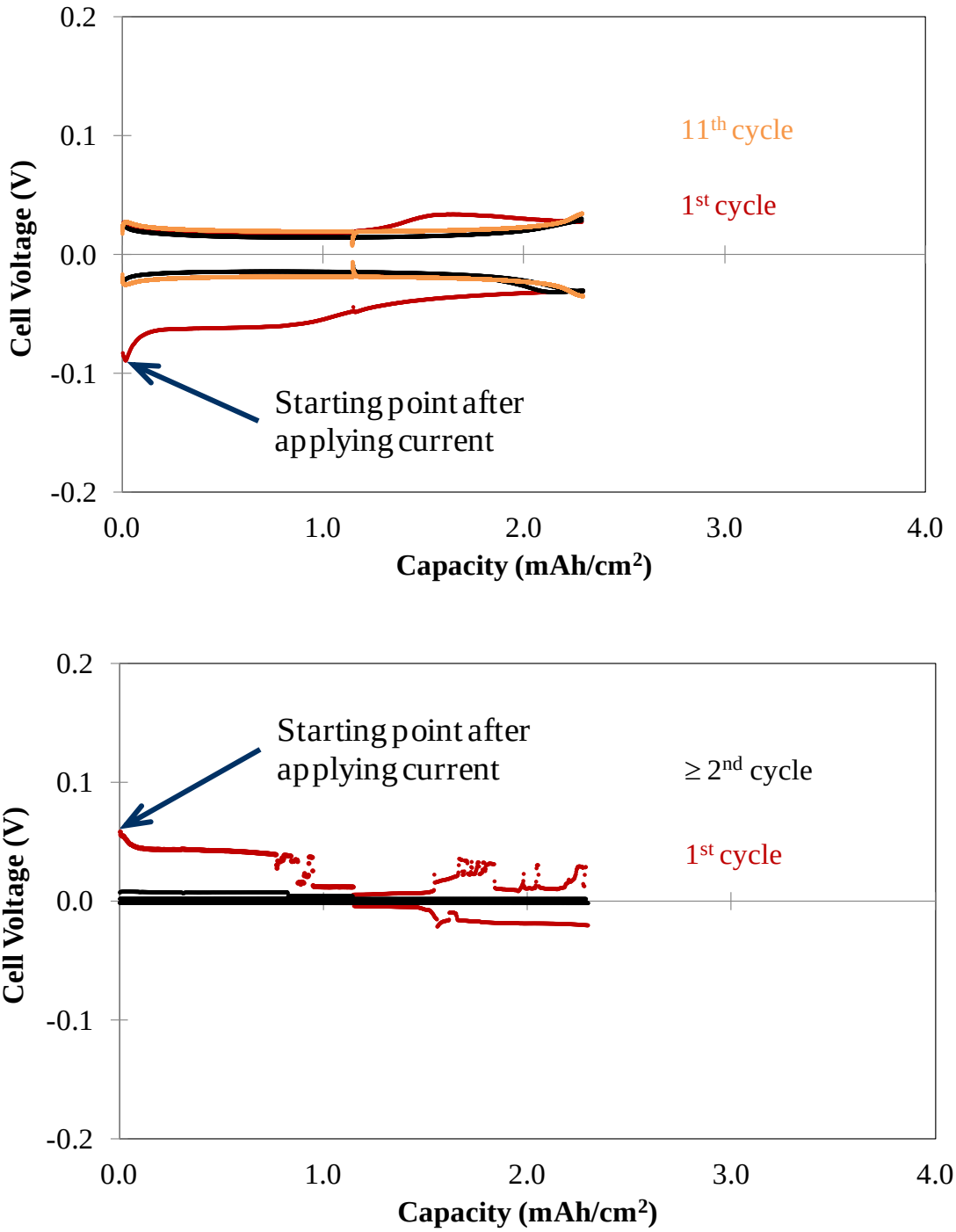

Figure 4.16 Voltage profile as a function of capacity related to the Li metal deposition and extraction of the symmetrical *Li vs. Li* cells with Celgard and Fleece (upper) and with only Fleece from the first to eventh cycles (lower)

The cycling conditions for the *Li vs. Li* cells are the same as in the *protective layer* cells. The resulting voltage profiles are shown in Figure 4.16. The cell with only Fleece separator has a short-circuit problem at which the cell voltage drops down to zero after the first cycle. At this state it is most likely that lihium dendrites directly contact both Li-metal electrodes. The cell with an additional Celgard separator exhibits no short-circuit behavior until the eleventh cycle.

The lowest cell voltage in the voltage profiles of the *Li vs. Li* with both Celgard and Fleece as separators appears at the first cycle at roughly -0.1 V. This highest absolute voltage value for the present measurement occurs at the beginning of the application of the constant current. As-received lithium metal foil is covered with a surface film of species like Li_2CO_3, Li_2O, and LiOH, which is poor in both Li-ion and electron conductivities [Fujieda 1994]. The surface film has a high resistance. When the *Li vs. Li* cells were assembled and first polarized, it resulted in the largest drop in the cell voltage compared to those in the following cycles as in Figure 4.16. From the second to the eleventh cycles, all the voltage profiles are alike, and the voltages constantly stay in the range between -0.05 and 0.05 V. This phenomenon can be explained by that the high-resistance surface film on the lithium metal foil is replaced with the better conductive layer of SEI.

For these reasons, the interfacial reactions between the lithium metal foil and liquid electrolyte do not play a role in the degradation observed in the cycling curves of the *protective layer* cells, Figure 4.15.

Before measuring the cell resistances by EIS, after deposition and extraction in each cycle, the *protective layer* cell was first allowed to relax for 15 min.

The impedance spectra of the cycled *protective layer* cells resembled those of the cells after the first Li-metal deposition. Three contributions: R_s, R_1//CPE_1 and R_2//CPE_2 were found, see Figure 4.14 and Table 4.2, so the data fitting and interpretation were carried out in the same manner.

R_{AC} is defined as the sum of all resistances from the impedance measurement, R_s, R_1, and R_2. In addition to EIS, the direct-current resistance R_{DC} was calculated by using data from the discharging and charging curves as illustrated in Figure 4.17 and assuming the Ohm's law as in eq. 4.2 to 4.3:

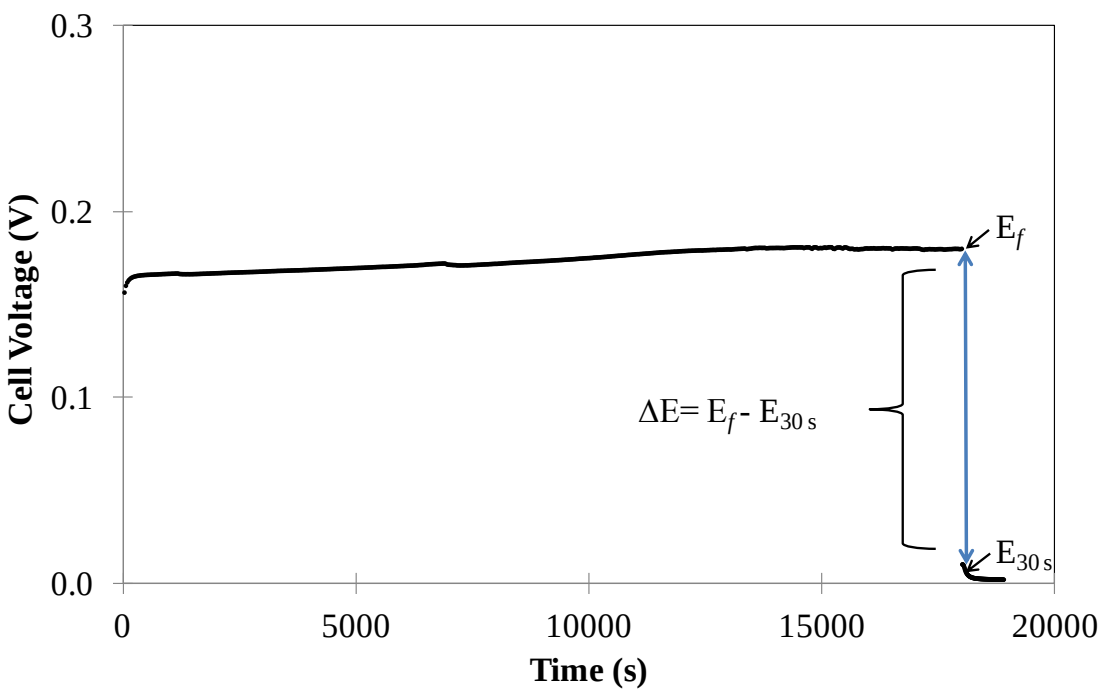

Figure 4.17 The cell voltage vs. time of a *protective layer* cell during the Li metal deposition with the details of ΔE for the calculation of R_{DC}

$$R_{DC} = \frac{\Delta E}{I} \tag{4.2}$$

$$\Delta E = | E_f - E_{30s} | \tag{4.3}$$

where E_f is the final voltage measured after the Li-metal deposition or extraction, E_{30s} is the open-circuit voltage recorded 30 seconds after terminating the current polarization, and I is the current applied.

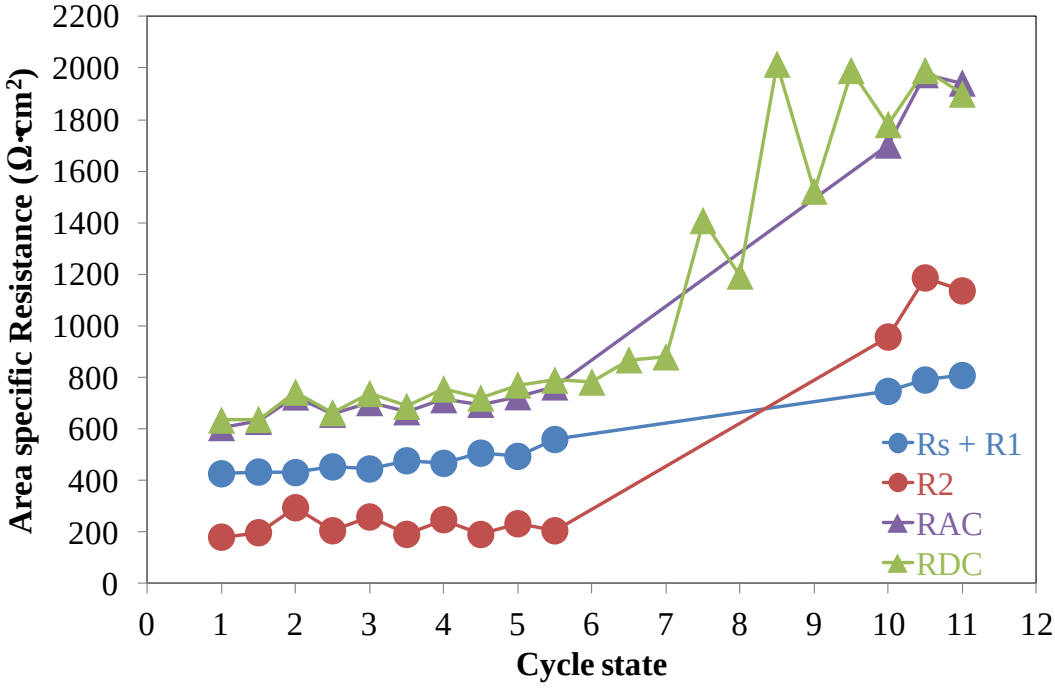

Figure 4.18 The resistances of R_s, R_1, R_2, R_{DC} and R_{AC} vs. the cycle state of the Li metal deposition and extraction of the *protective layer* cells

The resistances from the impedance measurement and the direct-current resistance after the Li-metal deposition and extraction versus the cycle states from the first to the eleventh cycles are expressed in Figure 4.18. The first deposition starts at the cycle state of 1.0, followed by the first extraction at 1.5. Further deposition and extraction states are likewise symbolized., The values of R_{AC} and R_{DC} are in good agreement, and follow the same trend. Between the first and the fifth cycles, both of them remain almost constant at around 700 Ω·cm^2. The total resistances of R_{DC} and R_{AC} increase up to

2000 $\Omega \cdot cm^2$.at the tenth cycle, which is almost three times the starting value. Furthermore, the total interface resistance R_2 overtakes the material resistances of (R_s + R_1). These changes do attest the degradation of the electrical contact at the interface between the Li-metal and LiPON.

4.3.2.3 SEM Analysis

At the fracture surface of the composite LATP plates where all the components Cu, lithium metal, LiPON, and LATP were piled up as a stack, see Illustration 3.5. Microstructure of such a system was investigated by SEM. The main fous is the lithium metal located at the LiPON interface. The SEM micrographs of the composite plates containing the lithium metal at different states, i.e. the first, second, fifth deposition and extraction, together with the eleventh deposition are shown in Figure 4.19 to Figure 4.23, respectively.

Before going into details regarding of the lithium metal layer on LiPON, it is interesting to pay attention to the microstructures of LiPON and LATP. All the taken SEM pictures have shown no pin hole in both solid electrolytes. This is also corresponding to the cycling and impedance results from the cells in which the protective layer of LiPON and LATP act as separator. No evidence of any effects related to the formation of Li-metal dendrite is observed, e.g. the fluctuation of the cell voltage or the short circuit where the voltage is very close to zero in the order of µV.

The capacity from the voltage curves of the *protective layer* cell relates to the applied current that causes the extraction and the deposition of lithium metal at the LiPON interface. Hence, the amount or thickness of the lithium metal at the LiPON interface is proportional to the capacity. From the capacity obtained after the deposition or the extraction, Q, the Li-metal specific

capacity, Q_{Li}, of 3862 mAh/g [Osaka 2000] and the Li-metal density, ρ_{Li}, of 0.534 g/cm^3 [Smithhells 1983] the thickness of the Li-metal layer, δ, can be calculated:

$$\delta[\mu m] = \frac{Q\left[mAh/cm^2\right] \cdot 10^4}{Q_{Li}\ [mAh/g]\ \cdot\ \rho_{Li}\left[g/cm^3\right]} \tag{4.4}$$

The Cu-Li-LiPON-LATP plates were fractured by hands. The microstructure of the interface between the lithium metal and LiPON can afftected by this preparation, i.e. the lithium metal layer might be sliding off from the LiPON surface. However, the overall microstructure of the lithium metal layer should be intact as before being fractured as in the cycled *protective* layer or the cycled *hybrid SC vs. Li* cells.

The deposition or the extraction of lithium metal occurs at where there is the electrical contact between LiPON and the first-deposited Li-metal layer. The Li-metal microstructure will be altered if the electrical is degenerated. The calculated thickness of lithium metal after the first deposition with the capacity of 3.45 mAh/cm^2 is 17 µm. According to Figure 4.19, the measured thickness of the lithium metal after the first deposition executed by the software combined with SEM is 19 ± 5 µm. The uncertainties are included from the sample preparation, placement, and undeniably measuring method (10 %), which accounts at least 20 %. Nonetheless, the difference between the measured and the calculated values is quite close.

Furthermore, the lithium metal layer appears dense and continous. These evidences validate the assumptions of film growth of the lithium metal during the first deposition observed as the plateau in the voltage curves in Figure

4.15. The capacity extracted during the next step is 2.3 mAh/cm^2. The capacity difference between the deposition and the extraction is 1.2 mAh/cm^2, leading to the calculated thickness of the lithium metal layer to 5 µm. The thickness measured after the first extraction in Figure 4.20 is 3 ± 2 µm.

The measured thicknesses after the deposition and the extraction from the second and fifth cycles shown in Figure 4.20, Figure 4.21, and Figure 4.22 are ranged from 16 to 20 µm (± 4 µm) and from 2 to 3 µm (± 1 µm), respectively. There is no visible degradation in the microstructure of the Li metal. As a consequence, the interface between the Li metal and LiPON maintains its morphology, which fits the behavior of the total cell resistances R_{AC} or R_{DC}, and the total interface resistance R_2 from the first to the fifth cycles presented in Figure 4.18.

A completely changed microstructure of the lithium metal layer after the eleventh deposition is noticed in the SEM images, see Figure 4.23 (a) to (f). The layer exhibits a column-like structure with a high thickness of nearly 30 µm. Both the thickness and the structure become inhomogeneous. With a large total resistances of R_{DC} or R_{AC} of around 2000 Ω·cm^2 in (Figure 4.18), it can be concluded that the interface between LiPON and the lithium metal is degenerated and randomly connected. The electrical contact at this interface has been diminished in area. This finally reduced the cycleability of the *hybrid SC vs. Li* cells.

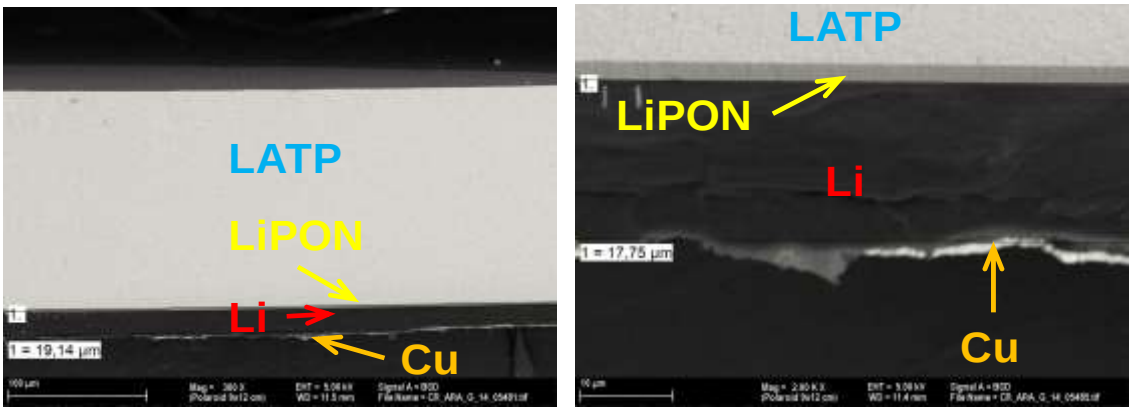

Figure 4.19 SEM micrographs of a Cu-Li-LiPON-LATP fracture surface after the first Li metal deposition with the magnifications of 300 X (left) and 2.0 kX (right)

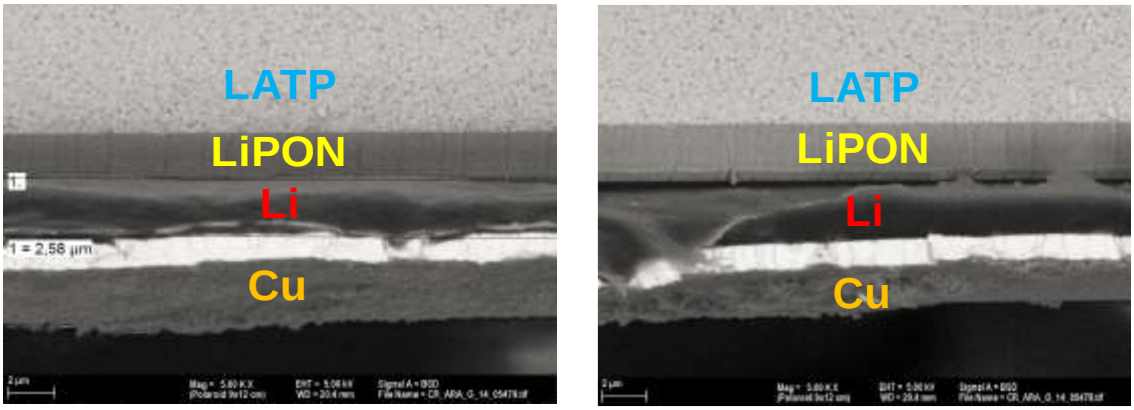

Figure 4.20 SEM micrographs of a Cu-Li-LiPON-LATP fracture surface after the first Li metal extraction with the magnification of 5.0 kX

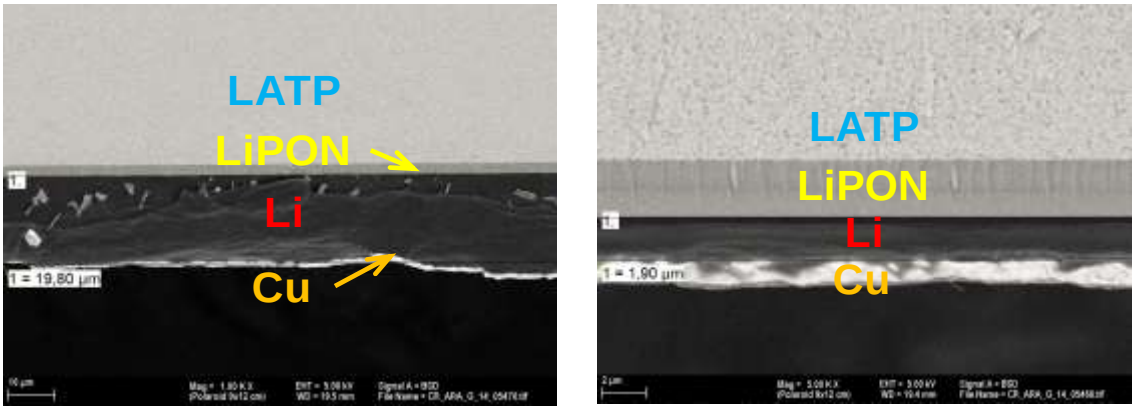

Figure 4.21 SEM micrographs of a Cu-Li-LiPON-LATP fracture surface after the second Li metal deposition (left) and extraction (right) with the magnifications of 1.0 kX and 5.0 kX, respectively

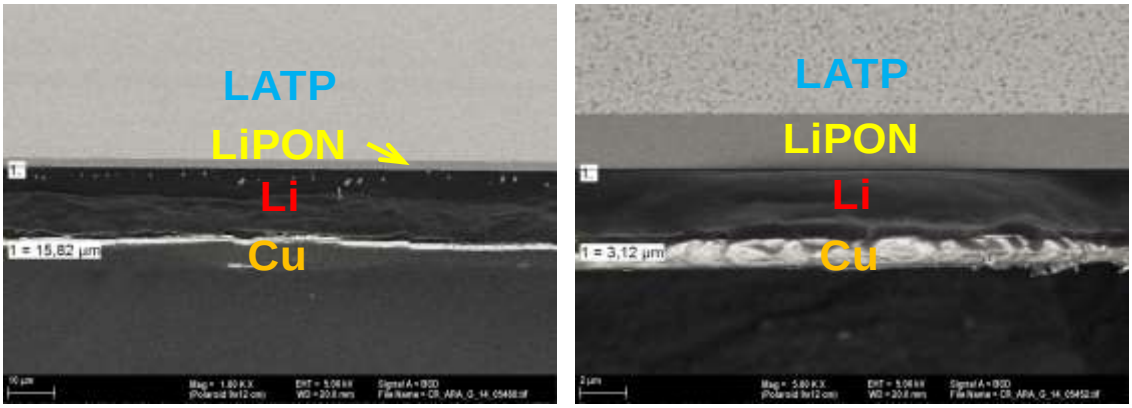

Figure 4.22 SEM micrographs of a Cu-Li-LiPON-LATP fracture surface after the fifth Li metal deposition (left) and extraction (right) with the magnifications of 1.0 kX and 5.0 kX, respectively

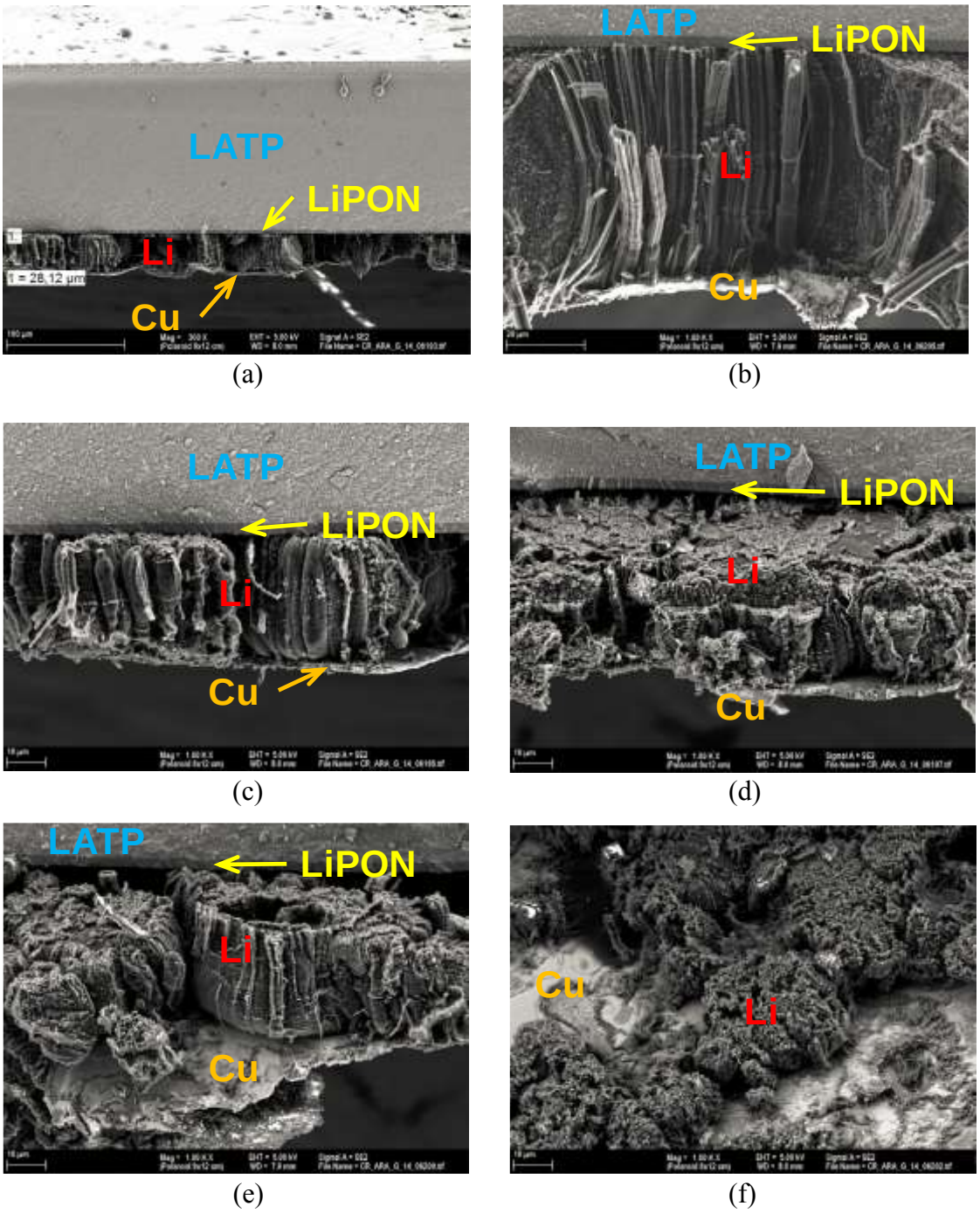

Figure 4.23 SEM micrographs of a Cu-Li-LiPON-LATP fracture surface after the eleventh Li metal deposition with the magnifications of 300 X (a) and 1.0 kX (b) to (f) at the different locations

Further analyses remain to be done to model the mechanism of this degradation. One explanation is a non-uniform current flow through the interface due to the surface roughness of LiPON or the heterogeneous distribution of the Li-ion conductivity at the LiPON surface. The latter variation is possibly a result of the material inhomogenity. The non-uniform current can lead to preferred Li-metal deposition or extraction on some locations, where high current passes through. This can create random empty space in the growing lithium metal layer during thr deposition process.

Another explanation could be the deformation of the contact between the lithium metal and LiPON owing to the repeated movement of the non-rigid thin Li-metal layer during the extraction and deposition. In the beginning, the Li-metal layer remains flat along the interface. After repeating the movement, the layer could become wrinkled, and subsequently have reduced to point contacts with LiPON.

An estimation of the maximum cycle number for the *hybrid SC vs. Li* cells can reach based on the cycleability of the *protective layer* cells is as follows: According to Figure 4.15, the accumulated capacity exchanged after the deposition and extraction of the lithium metal in the *protective layer* cells from the first extraction until the end of the sixth deposition (equivalent to complete 5 cycles) is 2 x 5 x 2.3 or 23 mAh/cm^2 or 18 mAh as the electrode area of 0.785 cm^2 is always considered. The average mass of a sulfur-electrode without current collector, used for the assembly of the *hybrid* cells is 0.0025 g. Then, the accumulated capacity is converted to 7200 mAh/g. Thanks to the following assumptions:

- The first discharge capacity of the *hybrid* cell is 500 mAh/g, according to Figure 4.3,
- Complete charging archeived in every cycle, meaning a charge capacity of 500 mAh/g in the following cycles
- No loss of active sulfur or polysulfides capacity,

The possible number of cycles for the *hybrid SC vs. Li* cells operating based on the capacity of 7200 mAh/g is 7. By this, it points out that there should be no capacity fading in the *hybrid SC vs. Li* cells for at least 7 cycles. From Figure 4.3, the capacity fading in the *hybrid* cells begins right after the second cycle and continues in the next cycles. It is concluded that the degradation of the electrical contact between the Li-metal and LiPON is not responsible for the initial capacity fading of the *hybrid* cells. A possible capacity loss due to the interaction between LATP and soluble sulfur or polysulfides is then investigated.

4.3.3 LATP in Protective Layer

To investigate the capacity fading related to LATP, impedance characterization was accomplished via the *hybrid SC vs. Li* cells and microstructural analyses were done directly on LATP taken out after disassembling the cells. The capacity loss due to the parasitic reactions between LATP and soluble sulfur or polysulfides could be proved by monitoring the OCV as well as cycling the *hybrid* cells. Aging conditions involving two states were implemented on the *hybrid* cells and created degrading effects on LATP.

The aging conditions were then concisely to expose LATP to the possible reactive species of soluble elemental sulfur and polysulfides, as well as to prolong the aging time. It was postulated that the reactions were time-dependent.

As the first state, the time after assembly of the *hybrid* cells leading to the exposure of LATP to soluble elemental sulfur, was extended to 24 h. The second state was that the *hybrid* cells were discharged and charged for one cycle to release polysulfides in the liquid electrolyte and let them contact LATP again for 24 h as another aging period for the *hybrid* cells.

4.3.3.1 OCV & Discharge Curve of Aged *Hybrid* Cells

OCV measurement was selected as an indicator to monitor the aging of *standard* and *hybrid SC vs. Li* cells since OCV links to the potentials of the electrochemically active species, e.g. elemental sulfur or polysulfides. The change of OCV could indicate the presence or absence of the active species inside the cells. In the *standard* cells, elemental sulfur dissolves into liquid electrolyte and diffuses to react directly with the lithium metal electrode forming polysulfides, [Kolosnitsyn 2008-2].

Across the first 24-h period after cell assembly the recorded OCV in Figure 4.24 decreases to 2.2 V from the initial value of 2.3 V. The discharge curve of the *standard* cells in Figure 4.25 also supports the claim of that all elemental sulfur has been transformed to polysulfides as evidenced by the absence of the upper discharge plateau.

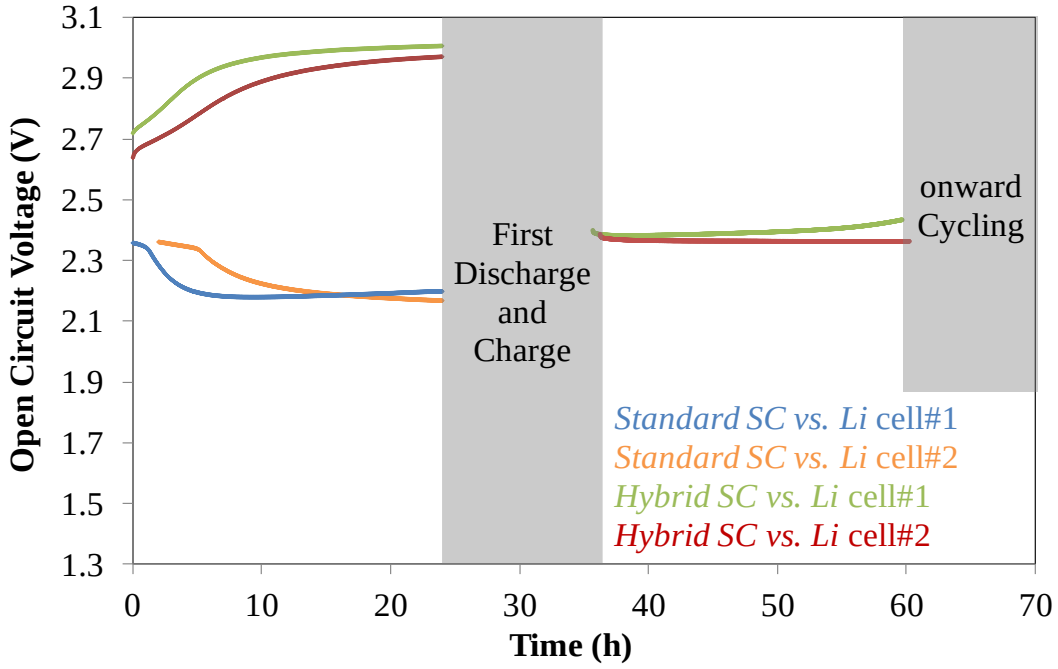

Figure 4.24 OCV vs. aging time of the *standard* and *hybrid SC vs. Li* cells

An inverse trend in the OCV is noticed for the *hybrid* cells. The initial OCV higher than 2.6 V is distinct, that might originate from the ring-opening of S_8 by the interaction with Ti (IV) in LATP to form more reactive sulfur species, as previously discussed in section 4.1. During the aging time of 24 h, the OCV continuously increases up to 3.0 V. Contrary to the behavior of the *standard* cells, the discharge curve of the *hybrid* cells according to Figure 4.25 still comprises the upper plateau. Based on these results, there seems to be no degradation at LATP or no parasitic reactions between LATP and soluble sulfur and polysulfides, inducing the capacity fading.

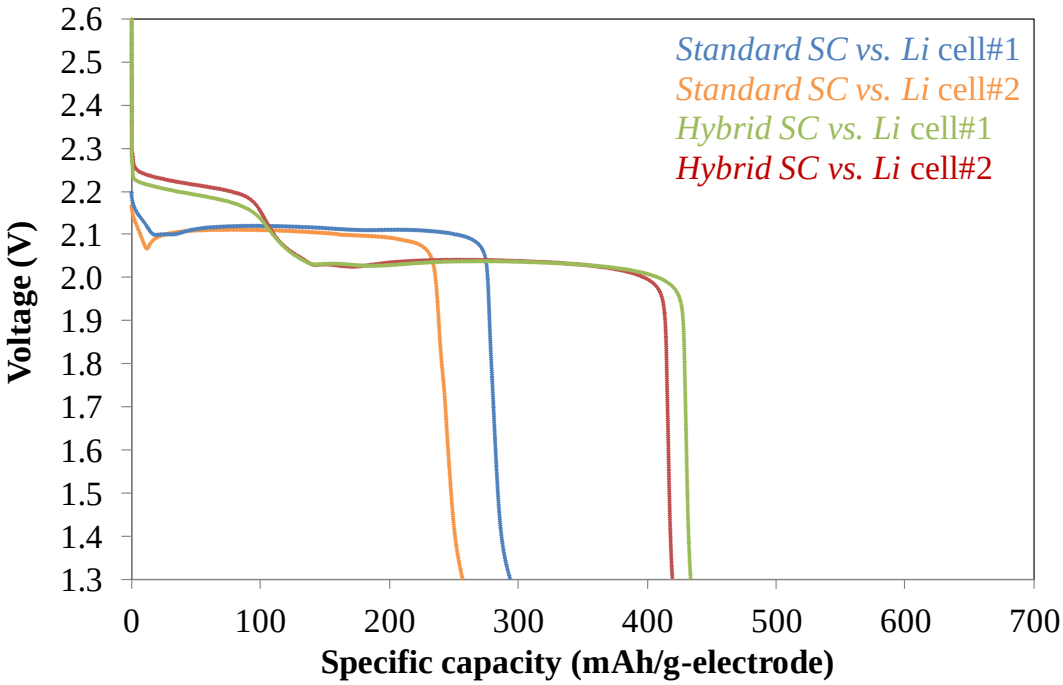

Figure 4.25 The first discharge curves of the *standard* and *hybrid SC vs. Li* cells after the aging time of 24 h after the cell assembly

4.3.3.2 Impedance measurement of Aged *Hybrid* Cells

The degradation in LATP can result from the change of its Li-ion conductivity. Impedance measurement of the aged *hybrid* cells was aimed to monitior the change of the LATP contribution in the impedance spectrum. This LATP contribution directly reflects the conductivity.

The first aging condition for the *hybrid* cells were also applied onto the *standard SC vs. Li* cells as a reference, where the cells were kept at the OCV-mode for 24 h. At this condition, soluble elemental sulfur dissolved into the liquid electrolyte phase and reacted with the lithium metal electrode, creating soluble polysulfides in the liquid phase. The impedance spectra of the *standard* cell assemblies can be seen in Figure 4.26. Figure 4.27 displays the im-

pedance data fitting with an equivalent circuit consisting of four contributions: R_s, R_1//CPE_1, R_2//CPE_2, and CPE_3 for the relaxation time of 15 min. The fitting of the impedance data at the other relaxation times was also carried out, likewise.

Note that all the types of the bulk, interface, blocking-interface, and diffusion contributions of each cell assembly related to fitting elements of an equivalent circuit from the EIS measurement are summarized in Table A.1, Table A.2, Table A.3 an dTable A.4 in Appendix.

R_s is the resistance of liquid electrolyte. CPE_3 can be interpreted as diffusion process of soluble sulfur and polysulfides as the value of CPE_3-P is in between 0.5 to 0.6 from Figure 4.31. This diffusion was also reported by Kolosnitsyn *et al*. [Kolosnitsyn 2011], Deng *et al*. [Deng 2013], and Canas *et al*. [Canas 2013].

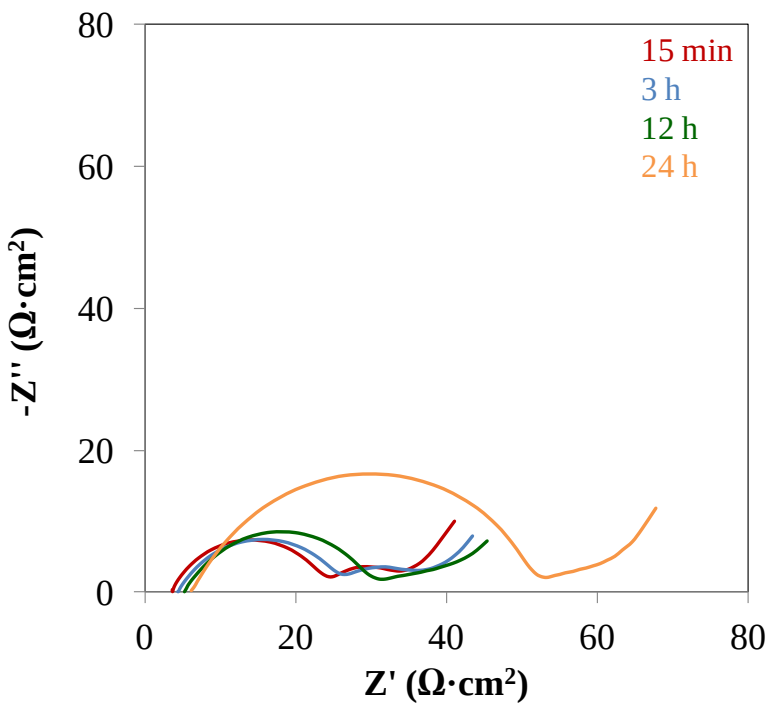

Figure 4.26 The impedance spectra at the differentaging times

measured after cell assembly of a *standard SC vs. Li* cell

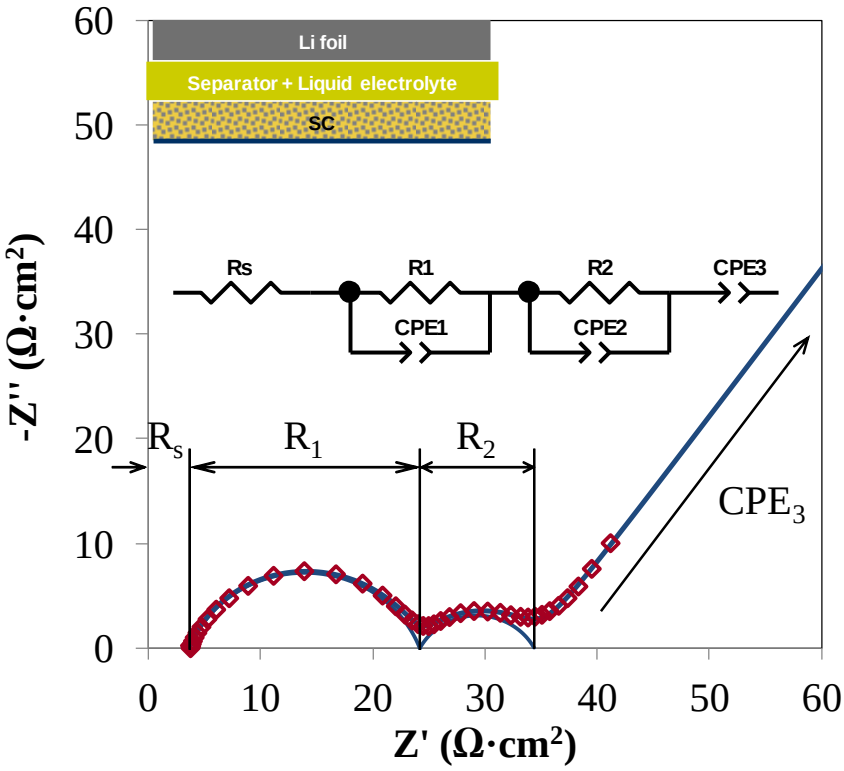

Figure 4.27 An impedance spectrum (red open symbol) after 15 min of the first-state aging time and its fitting curve (blue line)of a *standard SC vs. Li* cell, with the equivalent circuit

The effective capacitances of R_1//CPE_1 and R_2//CPE_2 are overall in the order of µF and mF, respectively, see Figure 4.28. The former is in the range of an electrical double layer, according to Table 2.2. If the surface area of the lithium metal electrode of 0.785 cm^2 is taken into consideration, it is still in the order of 1 µF/cm^2 as shown in Figure 4.29.

Hence, CPE_1 refers to the capacitance of the electrical double layer at the interface between the lithium metal electrode and liquid electrolyte, and R_1

is the charge transfer resistance correlating to lithium-ions and electrons, represented by eq. 2.10 or 2.15.

The high effective capacitance of $R_2//CPE_2$ potentially is attributed to the large total surface of the carbon-black particles, which is around 600 cm^2, in the sulfur-carbon electrode. The corresponding area-specific effective capacitances in Figure 4.29 stand between 1 and 10 $\mu F/cm^2$, which are also in the range of an electrical double layer from Table 2.2. Thus, CPE_2 associates with the interface between the carbon-black particles and liquid electrolyte, and R_2 is the resistance of charge transfer or the electrochemical reactions of polysulfides and/or soluble sulfur at this interface.

There are no values of the contributions of CPE_3 and $R_2//CPE_2$ at the aging time of 24 h, because the impedance spectrum shows the overlapping of both contributions and the fitting can not be accomplished.

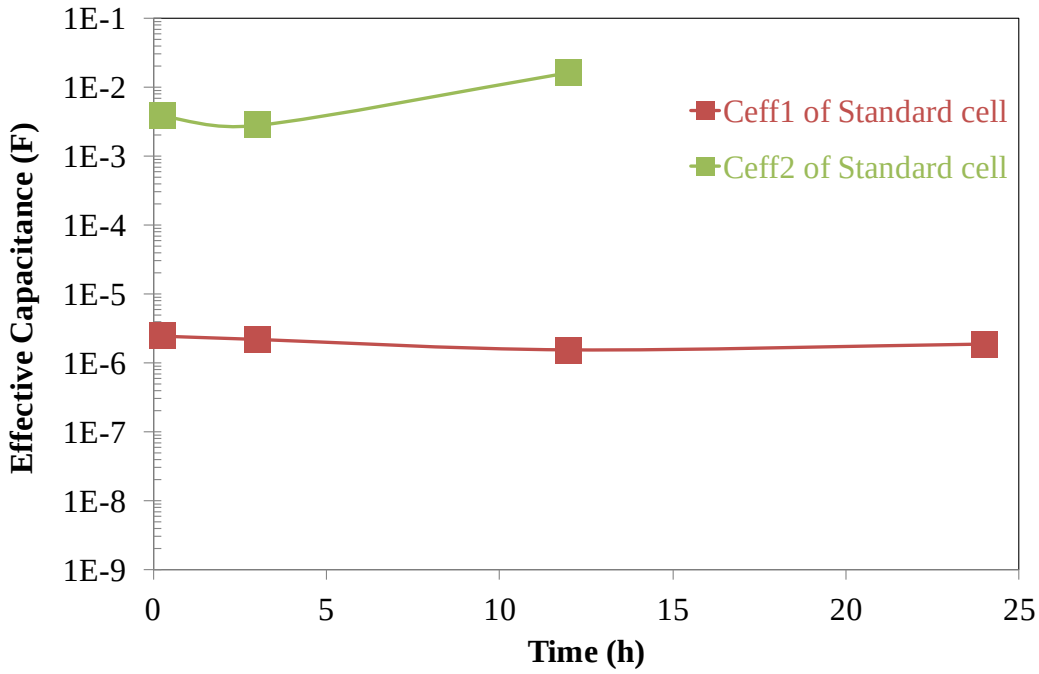

Figure 4.28 The effective capacitances: C_{eff1}, and C_{eff2} vs. the aging time, calculated from the impedance spectra measured after cell assembly of a *standard SC vs. Li* cell

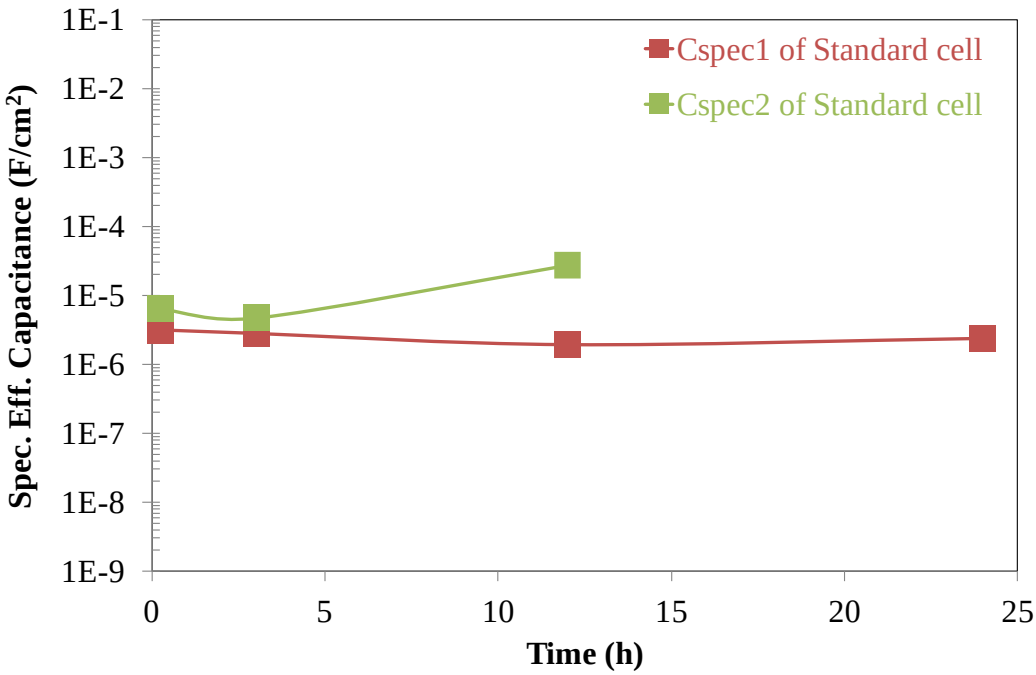

Figure 4.29 The specific effective capacitances: C_{spec1}, and C_{spec2} vs. the aging time, calculated from the impedance spectra measured after cell assembly of a *standard SC vs. Li* cell

All the resistances: R_s, R_1, and R_2 as functions of the aging time are plotted in Figure 4.30. In general, they increase along the time. This increase is expected to come from the dissolution of solid elemental sulfur from the sulfur-carbon electrode into the liquid electrolyte. The soluble elemental sulfur then reacts with the lithium metal electrode to create polysulfides. The longer the aging time is, the more the polysulfides are created. The high concentration of polysulfides makes the the liquid electrolyte more viscous and lower in the conductivity. This reduction of the conductivity of the liquid electrolyte is also stated by [Kolosnitsyn 2008-2].

R_1 is obviously the highest resistance compared to R_s, and R_2 at all times. From 15 min to 12 h, it rises marginally before soaring to 50 $\Omega \cdot cm^2$ after

24 h. The parasitic reactions at the surface of the lithium metal can lead to more surface passivation with insulating Li_2S, which conceivably causes the increasing R_2. Nevertheless, the reaction kinetics is rather slow as it took 24 h for this alteration. One explanation for the increase of R_2 from the aging times of 15 min to 12 h, can be that it is difficult for the charge transfer to process at the interface between the carbon black and liquid electrolyte due to the low lithium-ion conductivity of the liquid electrolyte, when there eas high concentration of the polysulfides.

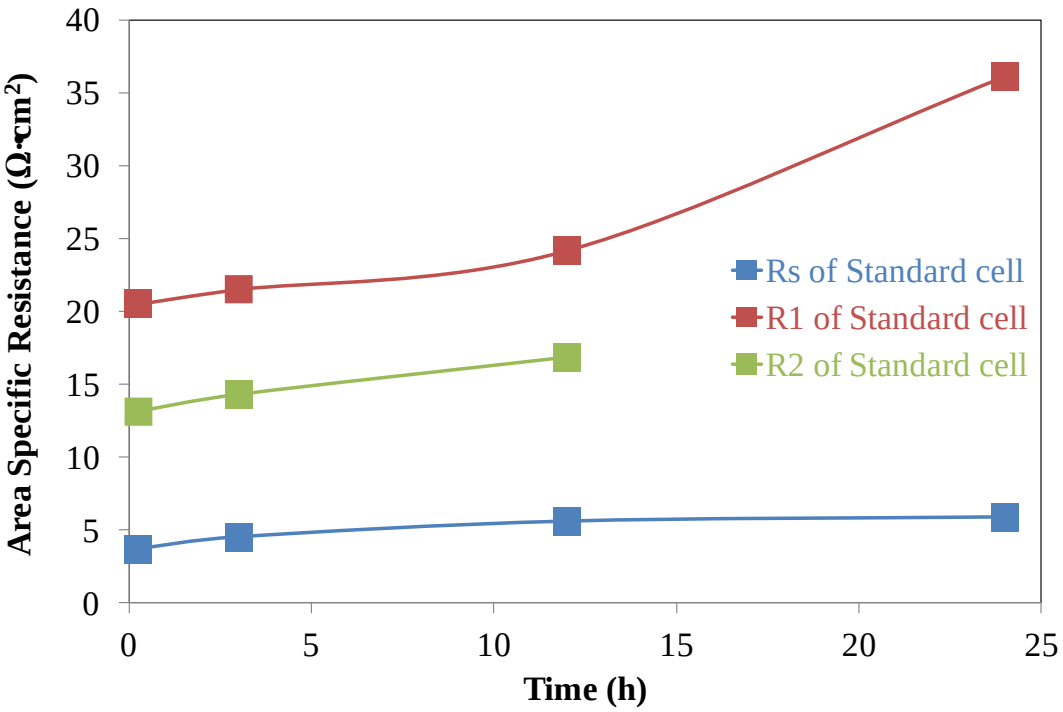

Figure 4.30 The resistances: R_s, R_1, and R_2 vs. the aging time, deducted from the impedance spectra measured after cell assembly of a *standard SC vs. Li* cell

In case of the *hybrid SC vs. Li* cells, impedance measurements were performed separately at the two states of the aging conditions. At the first state, LATP in the as-assembled *hybrid* cell#A was exposed to soluble elemental sulfur in liquid electrolyte.

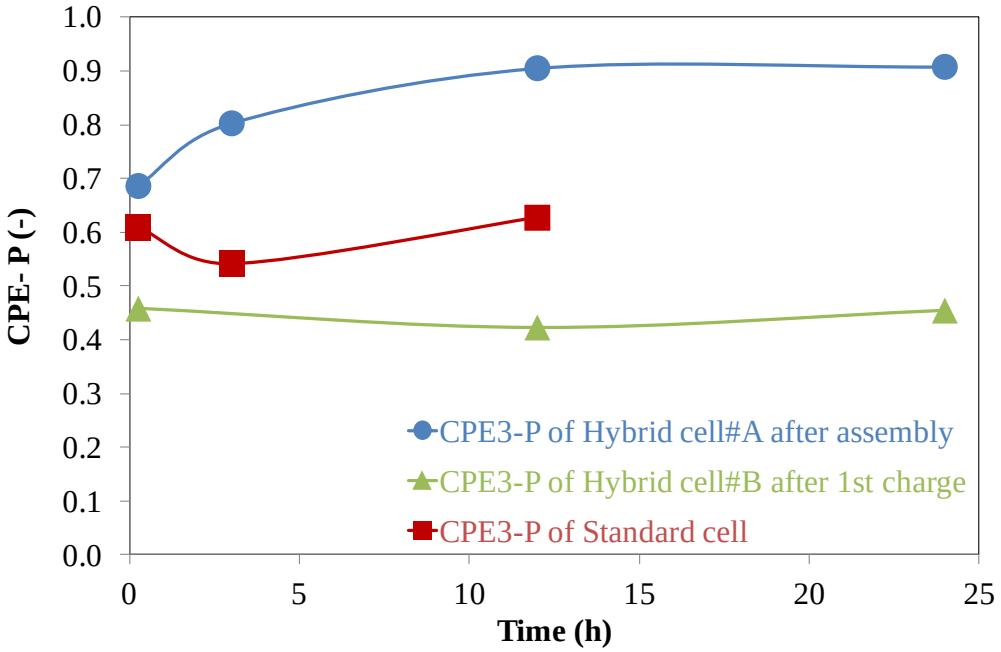

Figure 4.31 The CPE_3-P vs. the aging time, deducted from the impedance spectra measured after cell assembly of the *standard* and *hybrid SC vs. Li* cells, and the spectra measured after the first charge of the *hybrid* cell

The impedance spectra measured at the different aging times of 15 min, 3, 6, 12 and 24 h are shown in Figure 4.32. The impedance spectra were fitted by four contributions: R_s, R_1//CPE_1, R_2//CPE_2, and CPE_3. An example of the fitting of the umpedance spectrum at the aging time of 15 min is shown in Figure 4.34.

At the second state, the *hybrid* cell#B after the first charge contained both soluble sulfur and polysulfides in liquid electrolyte to be in contact with LATP. Figure 4.33 shows the impedance spectra at the aging times of 15 min, 12 and 24 h, and the fitting can be obtained by the same equivalent circuit with the four contributions as Figure 4.34.

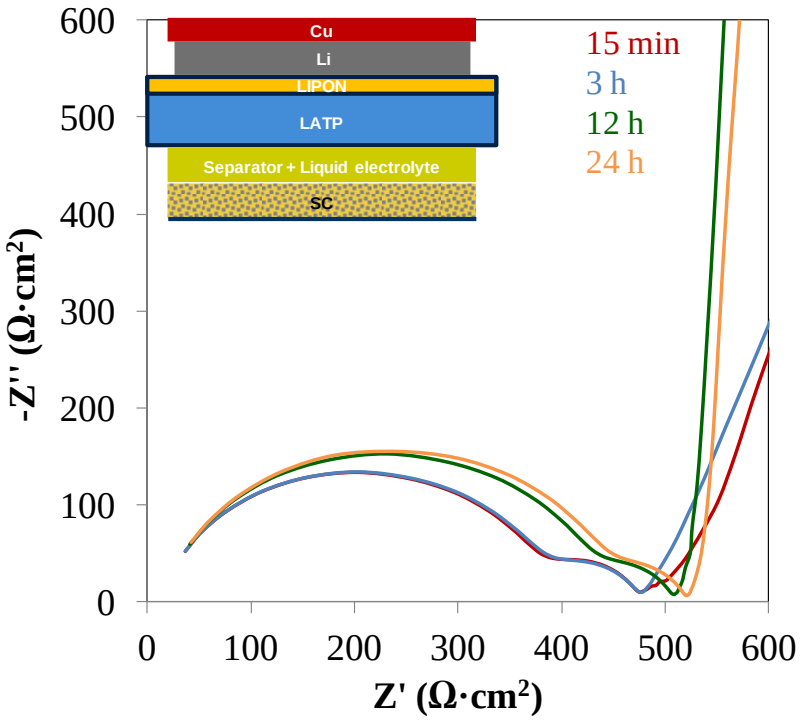

Figure 4.32 The impedance spectra at the different aging times measured after cell assembly of a *hybrid SC vs. Li* cell

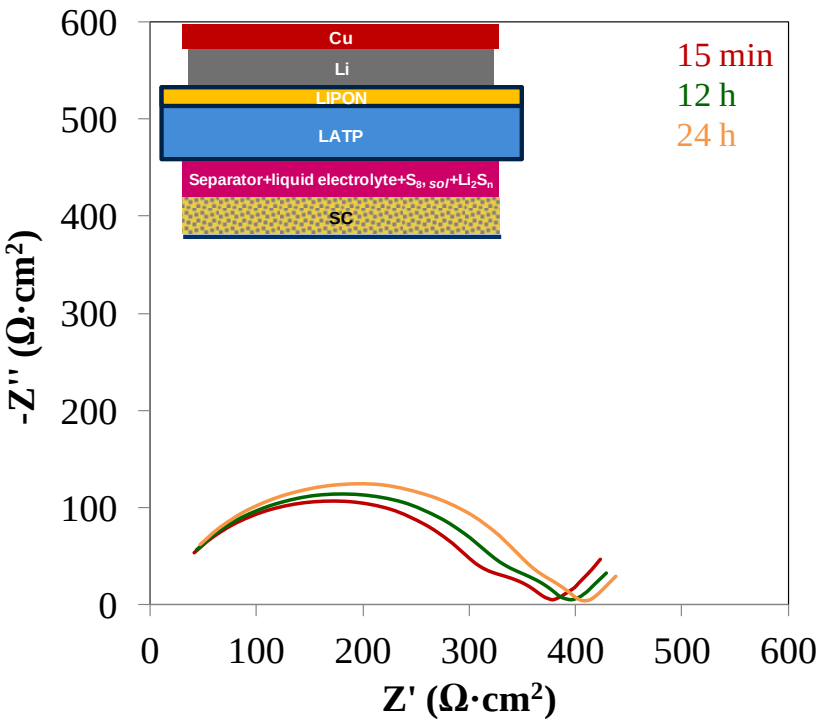

Figure 4.33 The impedance spectra at the different aging times measured after the first charge of a *hybrid SC vs. Li* cell

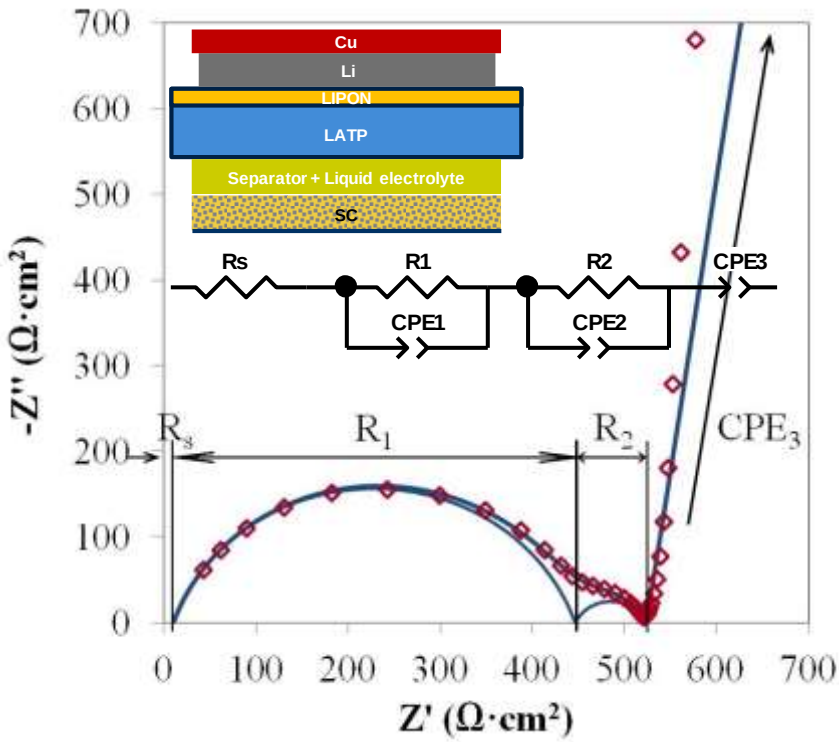

Figure 4.34 An impedance spectrum (red open symbol) after 15 min of the first-state aging timeand its fitting curve (blue line)of a *hybrid SC vs. Li* cell, with the equivalent circuit

From Figure 4.32 and Figure 4.33, R_s is not obviously present in the impedance spectra as its value is comparably lower than R_1. Hence, a combination of R_s and R_1 is instead calculated for further data analysis. Besides, Rs is a contribution corresponding to the high frequency

Across the 24-h aging time, the effective capacitances of R_1//CPE_1 obtained from either from the cell#A (after assembly) or #B (after the first charge) are more or less 3 nF see Figure 4.35, while the effective capacitances of R_2//CPE_2 of the cells#A and #B range from 2 to 3 µF. Interpretation and consideration for these effective capacitances can be done likewise to the impedance measurement of LATP-LiPON in section 4.3.2.1

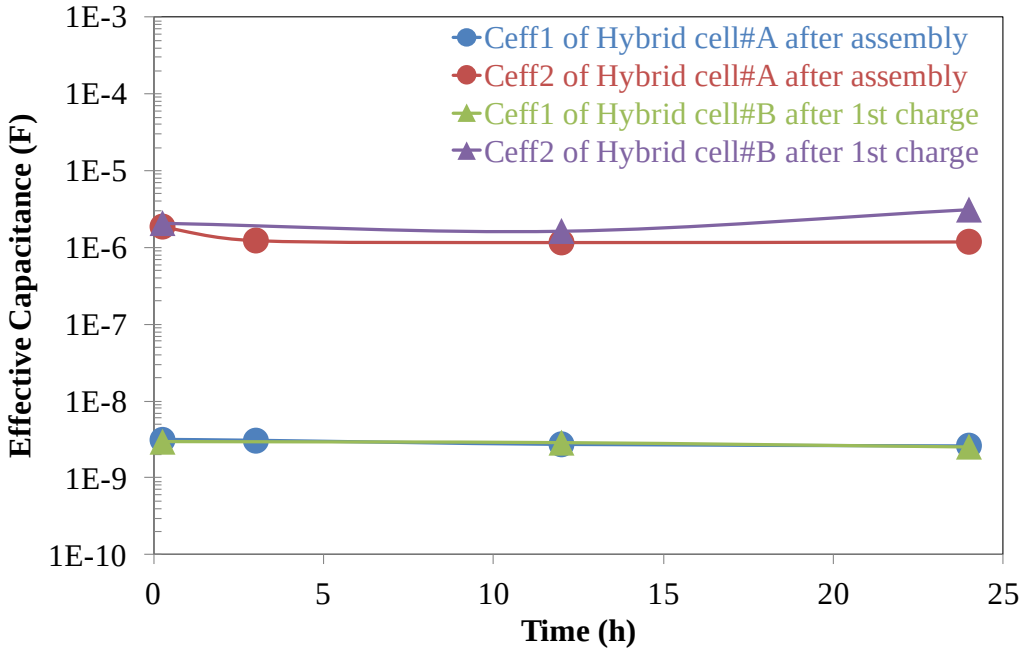

Figure 4.35 The effective capacitances: C_{eff1}, and C_{eff2} vs. time, calculated from the impedance spectra measured after cell assembly and after the first charge of the *hybrid SC vs. Li* cells

Once the 158-µm thickness of LATP and LiPON, along with the electrical contact area of 0.785 cm^2 are taken into account, the specific effective capacitance of R_1//CPE_1 is calculated to be from 50 to 60 pF/cm. The effective capacitance of R_2//CPE_2 is from 2 to 3 µF/cm^2 when only the contact area is considerd.

The effective capacitances of R_1//CPE_1 and R_2//CPE_2 versus the time are represented in Figure 4.36. Similar to the impedance results of the *hybrid* cells in section 4.3.2.1, the R_1//CPE_1 contribution connects with the grains and grain boundaries of the combined LATP-LiPON. CPE_2 and R_2 represent respectively the total capacitance of the electrical double layer and the total

charge transfer resistances from all the interfaces: Li-metal|LiPON, LiPON|LATP, and LATP|liquid electrolyte.

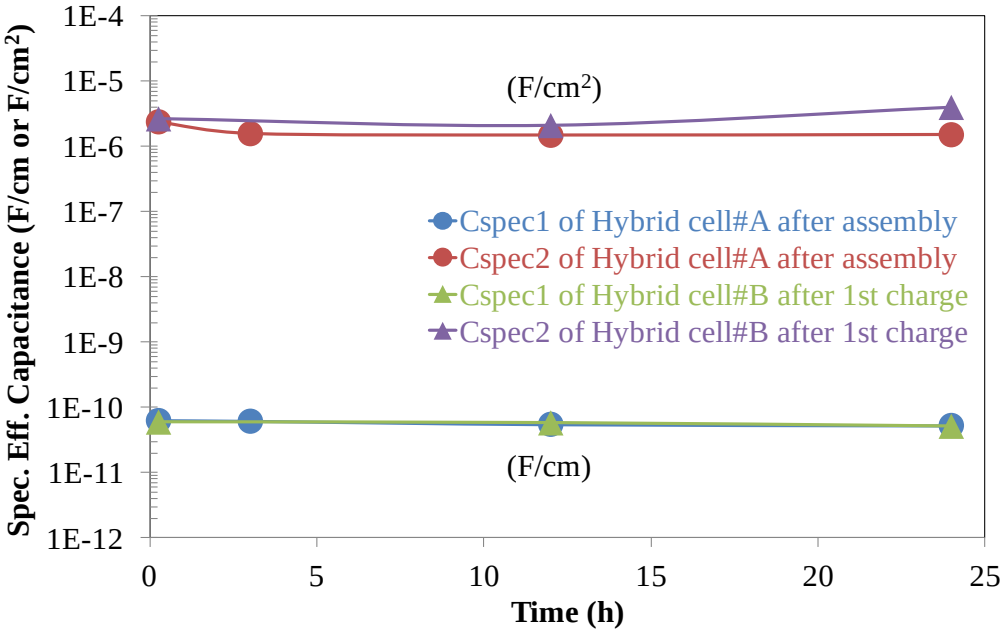

Figure 4.36 The specific effective capacitances: C_{spec1}, and C_{spec2} vs. time, calculated from the impedance spectra measured after cell assembly and after the first charge of the *hybrid SC vs. Li* cells

According to Figure 4.37, the tendency of the combined resistance ($R_s + R_1$), and the resistance R_2 versus the aging-time period of the *hybrid* cell#A (after assemly) and #B (after the first charge) is considered. Very similar tendency of each resistance- ($R_s + R_1$) or R_2 of the two *hybrid* cells is noticed. The charge-transfer resistance R_2 contribution of both cells is stable over the period, and the values for both cells are also close to each other.

The difference in ($R_s + R_1$) of the *hybrid* cells#A and #B possibly originates from the different thickness of LiPON on LATP. Thicker LiPON would bring higher resistance. From 15 min to 24 h, a slight increase in ($R_s + R_1$)

of the two *hybrid* cells of 50 $\Omega \cdot cm^2$ is concurrently observed. As LATP is exposed to the liquid electrolyte phase and the liquid electrolyte resistance is comparably small and negligible, the increase in the resistance should occur exclusively from a decrease in the Li-ion conductivity of LATP. Hence, LATP may be degraded due to the interaction with soluble sulfur or polysulfides. The total Li-ion conductivity of LiPON-LATP at the different aging times measured from the *hybrid SC vs. Li* cell#A and #B calculated by eq. 4.1 using the combined resistance (R_s + R_1), and the thickness of LiPON-LATP of 158 µm is shown in Figure 4.38. Small change of the conductivity of both *hybrid* cells#A and #B is observed, so the degradation of LATP is not significant.

Other species in liquid electrolyte like the ether solvents or lithium salt seem to have no influence since no change in the LATP resistance was observed in from the impedance measurement of the *Liquid-LATP* cells in section 4.3.2.1. From the available impedance results, the loss of active sulfur capacity can not be discussed. Further investigation is done by cycling test, see section 4.3.3.3.

The values of CPE_3-P measured from the *hybrid* cell#A for the entire period of the aging time in Figure 4.31 are from 0.7 to 0.9, which indicates the blocking-interface effect since the sulfur-carbon electrode is in a fully charged state. Only sulfur which is not a charge carrier unlike polysulfides is present. Conversely, the impedance spectra of the *hybrid* cell#B after the first charge give the CPE_3-P values close to 0.5, referring to the diffusion of polysulfides in liquid electrolyte. Due to the presence of polysulfides as charge carriers after the first charge, the blocking-interface effect disappears.

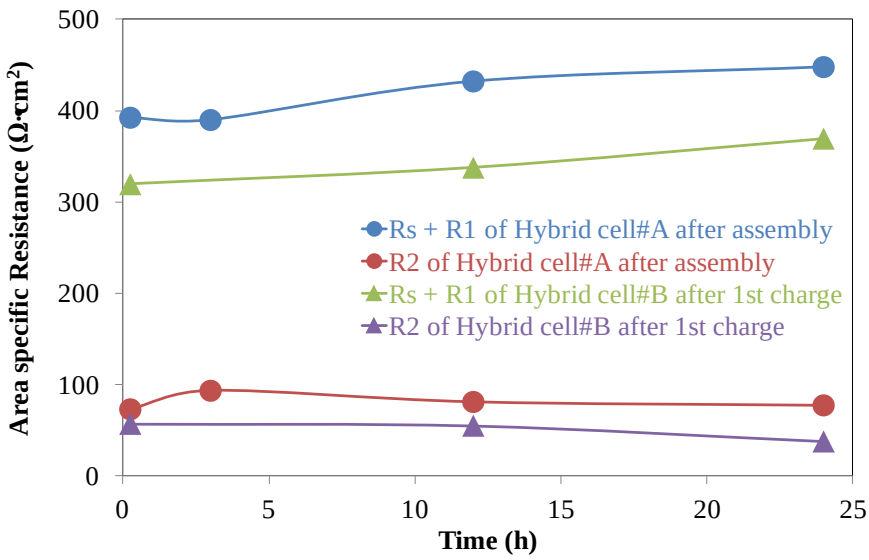

Figure 4.37 The specific effective capacitances: $R_s + R_1$, and R_2 vs. time, deducted from the impedance spectra measured after cell assembly and after the first charge of the *hybrid SC vs. Li* cells

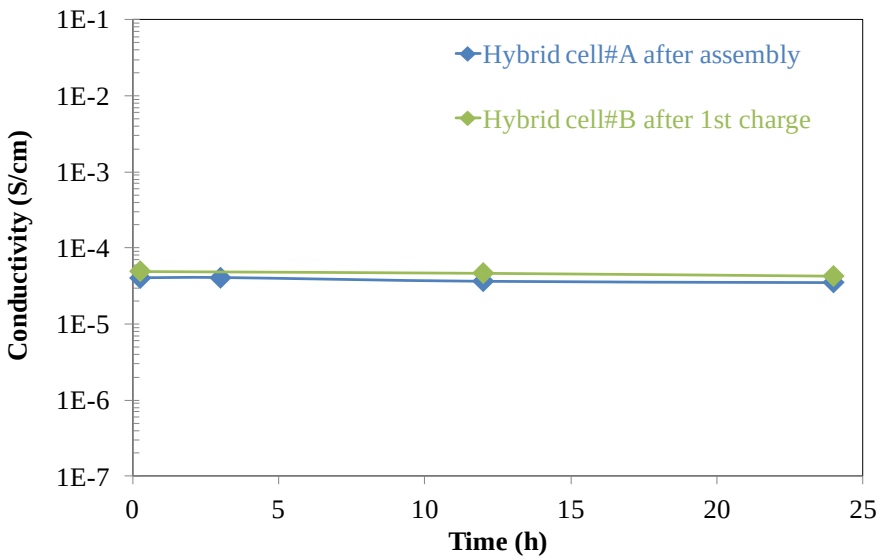

Figure 4.38 The Li-ion conductivity of LATP vs. the aging time Measured in the aged *hybrid SC vs.Li* cells#A and #B

4.3.3.3 Cycling of Aged *Hybrid* Cells

How the interaction between LATP and soluble sulfur and polysulfides from the aging conditions influences the cycleability of the aged *hybrid* cells can be verified by cycling the aged cells in comparison to the unaged ones. The cycling sequence was described in the experimental section 3.3.3. The results of the discharge capacity versus the cycle number are seen in Figure 4.39.

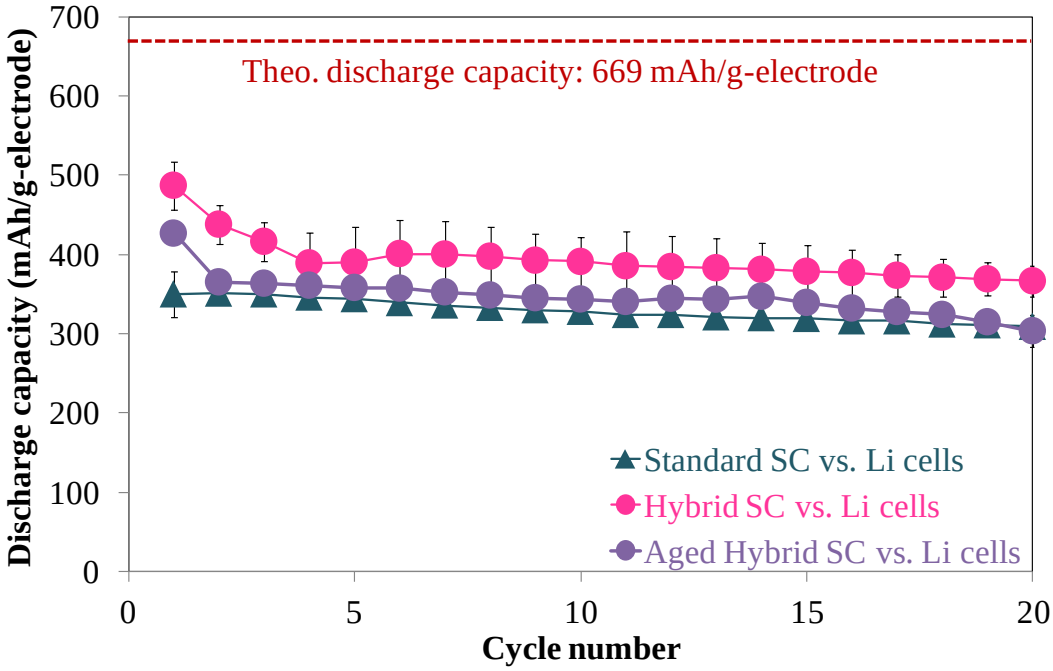

Figure 4.39 Discharge capacity vs. cycle number of *standard*, unaged and aged *hybrid SC vs. Li* cells via cycling at 0.2 mA/cm^2 (C/10)

The average first discharge capacity of the aged *hybrid* cells is around 425 mAh/g, which is 75 mAh/g lower than that of the unaged *hybrid* cells. Also, the second discharge capacity of the aged cells drops substantially to roughly 350 mAh/g while that of the unaged cells drops to 425 mAh/g. Further cycling of the aged and unaged *hybrid* cells expresses a comparably continuous fading rate in the capacity.

The small change of the Li-ion conductivity of LATP from the impedance measurement, see section 4.3.3.2 is not the main explanation for this significant capacity loss in the aged *hybrid* cells. In the first state of the aging conditions, there must be the loss of soluble elemental sulfur due to the irreversible parasitic reactions with LATP. Similarly observed in the second aging state, the parasitic reactions between polysulfides and LATP lead to the additional loss of the capacity.

After the aged *hybrid* cells from the first or second aging states had been dismantled, where the liquid phase had contact at the LATP plate, showed a dark blue color, see Figure 4.40. The blue location was deemed plausible by the build-up of Ti (III).

When LATP was in contact with soluble elemental sulfur in the liquid electrolyte during the first aging state, the reduction of Ti (IV) to Ti (III) is possible on the conditiona that Ti (IV) accepts eletron from elemental sulfur, so the oxidation state of sulfur becomes positive. The existing positive oxidation states of sulfur are +2, +3, +4, +5, and +6. However, there is no exact electrochemical information about the oxidation reactions of elemental sulfur, and the relevant electrochemical potentials.

The reactions of polysulfides with Ti (IV) in the aged *hybrid* cells over the second aging state corresponds to the work of Amiki *et al.* [Amiki 2013]. According to their work, that lithium-ions and electrons are inserted in LATP via the reduction reaction of Ti (IV) to Ti (III). The reaction takes place at virtually 2.35 V versus Li/Li^+.

The discharge behavior of lithium-sulfur batteries shown in Figure 4.1 demonstrates the reduction reaction from long-chain to short-chain polysulfides occurs at the potential lower than 2.2 V vs. Li/Li^+. Therefore, Ti (IV) or Ti^{4+} in LATP lattices can react with polysulfides by incorporating lithium ions and electrons from the polysulfides to form Ti (III) or Ti^{3+} as exemplified in the following proposed reactions (4.5), (4.6) and (4.7):

$$2Ti^{4+}_{LATP} + 3Li_2S_4 \rightleftharpoons 2[Ti^{3+} + Li^+]_{LATP} + 2Li_2S_6 \quad (4.5)$$

$$2Ti^{4+}_{LATP} + 4Li_2S_6 \rightleftharpoons 2[Ti^{3+} + Li^+]_{LATP} + 3Li_2S_8 \quad (4.6)$$

Or the half reaction on Ti:

$$Ti^{4+}_{LATP} + Li^+ + e^- \rightleftharpoons [Ti^{3+} + Li^+]_{LATP} \quad (4.7)$$

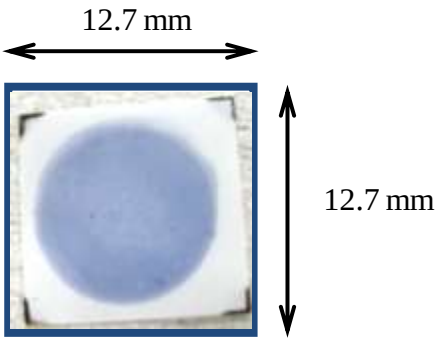

Figure 4.40 The circular area where in contact with liquid electrolyte composed of soluble sulfur and polysulfides.

4.3.3.4 XPS Analysis

The LATP plates taken from the aged *hybrid SC vs. Li* cells after the second aging state underwent an XPS analysis. The analysed areas corresponded to the blue and white locations of LATP as shown in Figure 4.40. The detected elements stated in Table 4.3 are discussed as follows:

Li, O, P, Al, Si, Ti, and Ge are elements expected according to Table 2.1 as they originate from the precursors for LATP synthesis. C, N, F, and S, are foreign species supposed to come from the environments such as the solvents DOL - $(CH_2)_2O_2CH_2$ and DME – $CH_3O(CH_2)_2OCH_3$ or the lithium salt LiTFSI – $(CF_3SO_2)_2N$-Li, or the polysulfides - Li_2S_n. C is generally found in any atmosphere and some of the detected C-atoms can be considered as contamination.

Table 4.3 Elemental composition from the XPS analysis at the white and blue locations of the LATP plates.

Color located on LATP	Atomic mass fraction (%) average from three areas of two samples										
	Li	C	N	O	F	P	S	Al	Si	Ti	Ge
Blue	9.9	34.7	0.3	36.8	5.5	7.7	0.4	1.5	0.4	1.7	1.3
White	3.5	46.2	0.4	36.2	1.4	6.7	0.3	1.8	1.2	1.1	1.2
Difference	6.3	-11.6	0.1	0.6	4.1	0.9	0.1	-0.3	-0.9	0.6	0.1
Relative Difference Fraction	1.8	-0.3	-0.1	0.0	2.9	0.1	0.3	-0.2	-0.7	0.5	0.0

For the interpretation of the results, the difference between the atomic mass fraction at the blue location and that at the white location of each element is calculated. The relative difference with respect to the mass fraction at the white location is additionally calculated. Striking differences are observed in the fractions of Li and F at the white and blue locations. There are higher

amounts of both elements at the blue locations compared to what is detected at the white locations.

The increasing amount of Li is expected as discussed in section 4.3.3.3 that the insertion of Li from polysulfides into LATP lattices via the reactions with Ti, forming Ti (III). After the reaction, the color of LATP turns to dark blue.

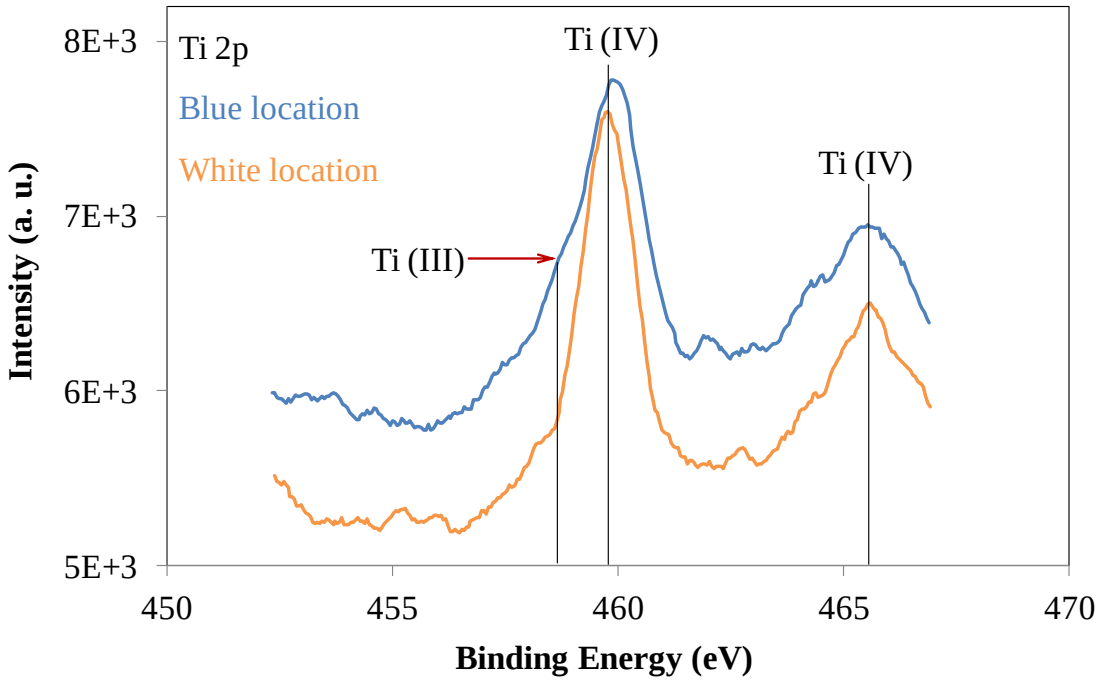

Figure 4.41 A XPS spectra of Ti 2p measured
at the blue and the white locations of an LATP plate

The XPS spectra of Ti taken at the blue and the white locations of the LATP are represented in Figure 4.41. At both locations, the double binding energy peaks of 460 eV and 466 eV referring to Ti (IV) are observed. An additional shoulder with the lower binding energy of *ca.* 458 eV is present only at the blue location. This is an evidence of the formation of Ti (III). Similar XPS

spectra of Ti (IV) and Ti (III) are also reported by [Aizawa 2003] and [Nasser 2000].

The excess Li at the blue location LATP was able to further react with F in the anion of $TFSI^-$ from the lithium salt (LiTFSI) to yield lithium fluoride (LiF). The XPS spectrum of F at the blue location in shown Figure 4.42 features a considerably high intensity of the binding energy of 685 eV, which is assigned for F in LiF, compared to that at the white location. This confirms a high amount of LiF at the blue location. Another F binding energy of around 489 eV found at both spectra is assigned for the residual lithium salt of LiTFSI. It can be contaminated at the white location during the cleaning step before the XPS measurement.

The binding energy of 64 eV in the XPS spectra in Figure 4.43 is possibly related to Na 2s [Barrie 1975], which is noticed at both the white and the blue location. The lithium metal foil purchased from China Energy Lithium Co., Ltd. is reported to contain Na metal [China Energy]. Some Na metal can be therefore dissolved into the liquid electrolyte as Na^+ via the first electrochemical deposition of the lithium metal at the interface between LiPON and Cu, see section 3.3.4. The dissolved Na^+ can be contaminated onto the LATP glass plate, and further active to the XPS analysis.

The Li binding energy of 56 eV can originate either from LiF or LiTFSI. Considering the high amount of F due to LiF at the blue location, the peak at 56 eV of the XPS spectrum of Li at the blue location correlates more to LiF. Instead, the spectrum of this binding energy at the white location possibly comes from the residual LiTFSI.

The references for the XPS spectra of Li and F in the compounds of LiF and LiTFSI are reported in [Schroder 2012], [Högström 2014], and [Ensling 2009].

The detected binding energies for the other elements: C, N, O, S, P, Al, Si, and Ge at the blue and the white locations exhibit no significant difference. For this reason, it is probable that no chemical reactions involve these elements.

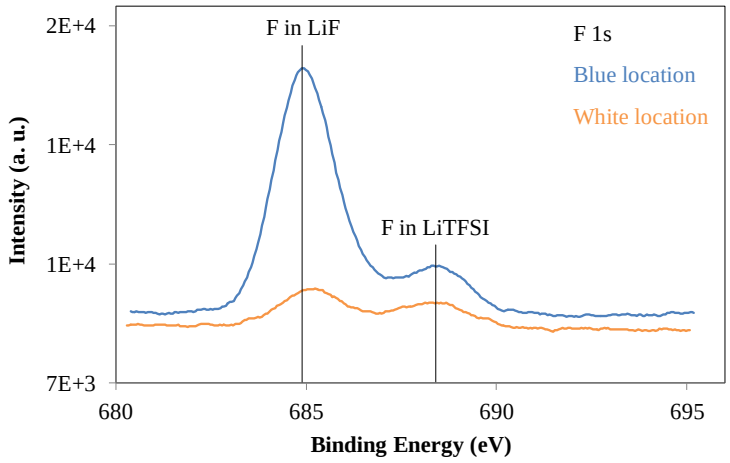

Figure 4.42 XPS spectra of F 1s measured
at the blue and the white locations of an LATP plate

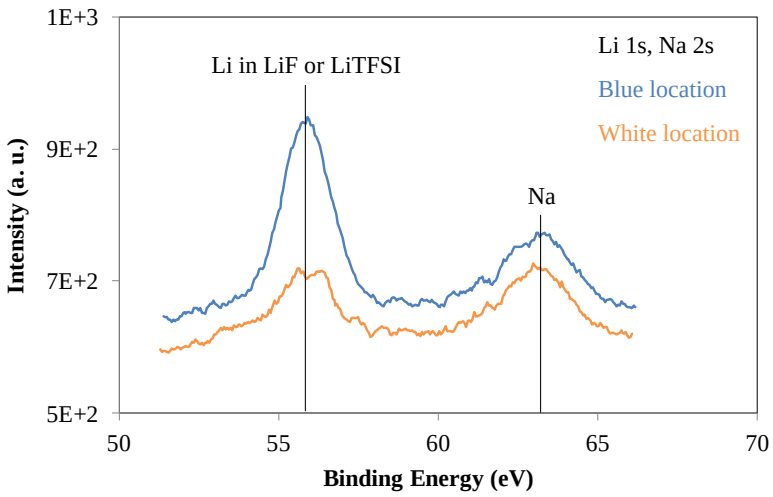

Figure 4.43 A XPS spectra of Li 1s and Na 2s measured
at the blue and the white locations of an LATP plate

5 Conclusion and Outlook

The *hybrid* cells of lithium-sulfur batteries are composed of the standard sulfur-carbon electrode, the liquid electrolyte, and the composite solid electrolyte of LATP and LiPON acting as a protective layer on a lithium metal layer. LiPON and LATP possess the striking feature of dense microstructure, that do not allow the growth of Li-metal dendrite from the Li-metal electrode towards the sulfur-carbon electrode.

These cells showed an increase in the discharge capacity of 20 %, compared to the *standard* cells without the protective layer. The improvement is achieved by suppressing the loss of electrochemically active sulfur to react with the lithium metal electrode. In addition, the shuttle mechanism due to the presence of polysulfides is not visible in the *hybrid* cells.

However, the cycleability of the *hybrid* cells is still a concerned issue. The discharge capacity starts to deteriorate since the second cycle. One factor of the deterioration is the oxidation of polysulfides and/or soluble elemental sulfur in the liquid electrolyte phase by Ti (IV) in LATP. The change of the LATP color from white to dark blue is noticed at the contact area with the liquid phase, accordingly. The XPS analysis concurs the reactions between LATP and polysulfides, providing the evidence of a higher Li concentration at the blue area of LATP than that at the white area. An additional binding energy of Ti, which is possibly related to Ti (III), is observed only at the blue location of LATP.

The *protective layer* cells in which the two electrodes of lithium metal are separated by the protective layer and liquid electrolyte disclose a second remarkable degradation mechanism. Cycling tests and impedance measurements of the cells demonstrate an increase in the cell resistance. After ten cycles of deposition and extraction of the Li-metal at the interface to LiPON, the electrical contact between the Li metal and LiPON is worsened. The degradation of the Li-metal microstructure is proved by the SEM micrographs at the fractured surface of the cycled protective layers. Two possibilities are proposed for the origin of the degradation:

- Inhomogeneous Li-metal deposition and extraction due to the roughness or the Li-ion conductivity variation at the LiPON surface
- Deformation of the interfacial contact between the Li-metal layer and LiPON owing to the movement of the thin and flexible layer of Li-metal

The sulfur-carbon electrode does not play a significant role in fading the capacity of the *hybrid* cells. The symmetrical cells of the sulfur-carbon electrodes verify the low degeneration in the carbonaceous conductive matrix, since their resulting long-term cycleability is quite consistent.

The major challenge of lithium-sulfur batteries remains at the lithium metal electrode. Protection of the lithium metal is inevitable to achieve high capacity and stable cycleability of the batteries. New materials that are non-reactive to soluble sulfur and polysulfides have to be considered for the protective layer, which can be garnet-type or Ti-free phosphate-glass, i.e. LAGP. Futher investigations on the behavior of the Li-metal deposition and extraction at the solid electrolyte interface also have to be done in order to understand and to avoid the degrading phenomenon.

6 References

[Aizawa 2003] M. Aizawa, S. Lee, and S. L. Anderson, *Surf. Sci.*, 2003, **543**, 253 – 275.

[Akridge 2004] J. R. Akridge, Y. V. Mikhaylik and N. White, *Solid State Ionics*, 2004, 175, 243 – 245.

[Amiki 2013] Y. Amiki, F. Sagane, K. Yamamoto, T. Hirayama, M. Sudoh, M. Motoyama, and Y. Iriyama, *J. Power Sources*, 2013, **241**, 583 – 588.

[Aurbach 2000] D. Aurbach, *J. Power Sources*, 2000, **89**, 206 – 218.

[Aurbach 2009] D. Aurbach, E. Pollak, R. Elazari, G. Salitra, C. S. Kelley, and J. Affinito, *J. Electrochem. Soc.*, 2009, **156**, A694 – A702.

[Barrie 1975] A. Barrie, and F. J. Street, *J. Electron. Spectrosc.*, 1975, **7**, 1 – 31.

[Boukamp 2004] B. Boukamp, *Solid State Ionics*, 2004, **169**, 65 – 73.

[Boukamp 2008] B.A. Boukamp, "Electrochemical Impedance Spectroscopy", U. Leiden, 2008.

[Boukbir 1989] L. Boukbir, R. Marchand, Y. Laurent, P Bacher, and G. Roult, *Ann. Chim. Fr.*, 1989, **14**, 475.

[Bruce 2012] P. G. Bruce, S. A. Freunberger, L. J. Hardwick, and J. M. Tarascon, *Nat. Mater.*, 2012, **11**, 19 – 29.

[Canas 2013] N. A. Canas, K. Hirose, B. Pascucci, N. Wagner, K. A. Friedrich, and R. Hiesgen, *Electrochim. Acta*, 2013, **97**, 42 – 51.

[Cheon 2003]. S. E. Cheon, K. S. Ko, J. H. Cho, S. W. Kim, E. Y. Chin, and H. T. Kim, *J. Electrochem. Soc.*, 2003, **150,** A800 – A805.

[China Energy] http://en.cellithium.com/index.html.

[Choi 2008] Y. J. Choi, K. W. Kim, H. J. Ahn, and J. H. Ahn, *J. Alloy Compd.*, 2008, **449,** 313 – 316.

[Deng 2013] Z. Deng, Z. Zhang, Y. Lai, J. Liu, J. Li, and Y. Liu, *J. Electrochem. Soc.*, 2013, **160**, A553 – A558.

[Dudney 2000] N. J. Dudney, *J. Power Sources*, 2000, **89**, 176 – 179.

[EL cell] http://el-cell.com/products/test-cells/ecc-std.

[Elazari 2010] R. Elazari, G. Salitra, Y. Talyosef, J. Grinblat, C. S. Kelly, A. Xiao, J. Affinito, and D. Aurbach, *J. Electrochem. Soc.*, 2010, **157** A1131 – A1138.

[Elazari 2012] R. Elazari, G. Salitra, G. Gershinsky, A. Garsuch, A. Panchenko, and D. Aurbach, *Electrochem. Commun.*, 2012, **14**, 21 – 24.

[Ensling 2009] D. Ensling, M. Stjerndahl, A. Nytén, T. Gustafsson, and J. O. Thomas, *J. Mater. Chem.*, 2009, **19**, 82 – 88.

[Fu 1997] J. Fu, *J. Am. Ceram. Soc.*, 1997, **80**, 1901 – 903.

[Fujieda 1994] T. Fujieda, N. Yamamoto, K. Saito, T. Ishibashi, M. Honjo, S, Koike, N. Wakabayashi, S. Higuchi, *J. Power Sources*, 1994, **52**,.197 – 200.

[Guo 2011] J. Guo, Y, Xu, and C. Wang, *Nano Lett.*, 2011,.**11**, 4288 – 4294.

[Hassoun 2012] J. Hassoun, J. Kim, D. J. Lee, H. G. Jung, S. M. Lee, Y. K. Sun, and B. Scrosati, *J. Power Sources*, 2012, **202**, 308 – 313.

[Högström 2014] K. C. Högström, S. Malmgren, M. Hahlin, M. Gorgoi, L. Nyholm, H. Rensmo, and K. Edström, *Electrochim. Acta*, 2014, **138**, 430 – 436.

[Imanishi 2008] N. Imanishi, S. Hasegawa, T. Zhang, A. Hirano, Y. Takeda, and O. Yamamoto, *J. Power Sources*, 2008, **185**, 1392 – 1397.

[Illig 2010] J. Illig, T. Chrobak, M. Ender, J. P. Schmidt, D. Klotz, and E. Ivers-Tiffée, *ECS Trans.*, 2010, **28**, 3 – 17.

[Jeon 2002] B. H. Jeon, J. H. Yeon, K. M. Kim, and I. J. Chung, *J. Power Sources*, 2002, **109**, 89 – 97.

[Ji 2010] X. Ji, and L. F. Nazar, *J. Mater. Chem.*, 2010, **20**, 9821 – 9826.

[Knauth 2009] P. Knauth, *Solid State Ionics*, 2009, **180**, 911 – 916.

[Kolosnitsyn 2008-1] V. S. Kolosnitsyn, and E. V. Karaseva, *Russ. J. Electrochem.*, 2008, **44**, 506 – 509.

[Kolosnitsyn 2008-2] V. S. Kolosnitsyn, E. V. Karaseva, and A. L. Ivanov, *Russ. J. Electrochem.*, 2008, **44**, 564 – 569.

[Kolosnitsyn 2011] V. S. Kolosnitsyn, E. V. Kuzmina, E. V. Karaseva, and S. E. Mochalov, *J. Power Sources*, 2011, **196**, 1478 – 82.

[Levi 1999] M. D. Levi, G. Salitra, B. Markowsky, H. Teller, D. Aurbach, U. Heider, and L. Heider, *J. Electrochem. Soc.*, 1999, **4,** 1279 – 1289.

[Lux 2013] Lux Research Inc., “Beyond Lithium-Ion: A Roadmap for Next-Generation Batteries”, March 2013.

[Macdonald 1987] J. R. Macdonald, editor, “Impedance Spectroscopy Emphasizing Solid Materials and Analysis”, John Wiley and Sons, New York, 1987.

[Monroe 2003] C. Monroe, and J. Newman, *J. Electrochem. Soc.*, 2003, **150**, A1377 – A1384.

[Nasser 2000] S. A. Nasser, *Appl. Surf. Sci.*, 2000, **157**, 14 – 22.

[Nazar 2009] X. L. Ji, K. T. Lee, and L. F. Nazar, *Nat. Mater.*, 2009, **8**, 500 – 506.

[OHARA] OHARA flyer from http://www.ohara-gmbh.com/e/produkte/

licgc.html.

[Osaka 2000] T. Osaka, and M. Datta, editors, “Energy Storage Systems for Electronics”, Gordon and Breach Science Publishers, Singapore, 2010.

[Rao 1981] B. M. L. Rao, and J. A. Shropshire, *J. Electrochem. Soc.*, 1981, **128**, 942 – 945.

[Schroder 2012] K.W. Schroder, H. Celio, L.J. Webb, and K.J. Stevenson, *J. Phys. Chem. C*, 2012, **116**, 19737 – 19747.

[Sigma-Aldrich] http://www.sigmaaldrich.com/catalog/product.

[Smithhells 1983] Smithells Metals Reference Book, 6, ed. E.A. Brandes (London:Butterworths, 1983).

[Song 2004] M. S. Song, S. C. Han, H. S. Kim, J. H. Kim, K. T. Kim, Y. M. Kang, H. J Ahn, S. X. Dou, and J. Y. Lee ,*J. Electrochem.Soc.*, 2004, **151**, A791 – A795.

[Swagelok] http://www.swagelok.com/search/find_products_home.aspx?part=SS-200-3.

[Takada 2009] K. Takada, *Enc. Electrochem. Power Sources*, 2009, **5**, 328 – 336.

[Thangadurai 2003] V. Thangadurai, H. Kaack, and W. J. F. Weppner, *J. Am. Ceram. Soc.*, 2003, **86**, 437 – 440.

[Vetter 2005] J. Vetter, P. Novak, M. R. Wagner, C. Veit, K. C. Möller, J. O. Besenhard, M. Winter, M. Wohlfahrt-Mehrens, C. Vogler, and A. Hammouche, *J. Power Sources*, 2005, **147**, 269 – 281.

[Wang 2003] J. L. Wang, J. Yang, C. R. Wan, K. Du, J. Y. Xie, and N. X. Xu, *Adv. Func. Mater.*, 2003, **13**, 487 – 492.

[Wang 2008] J. Wang, S. Y. Chew, Z. W. Zhao S. Ashraf, D. Wexler, J. Chen, S. H. Ng, S. L. Chou, and H. K. Liu, *Carbon.*, 2008, **46**, 229 – 235.

[Weber 2014] V. Weber, T. Laino, A. Curioni, T. Eckl, C. Engel, J. Kasemchainan, and N. Salingue; Manuscript ID: jp-2014-105455 submitted to *J. Phys. Chem. C.*

[Wie 2011] W. Wei, J. L. Wang, L. J. Zhou J. Yang, B. Schumann, and Y. NuLi, *Electrochem. Commun.*, 2011, **13**, 399 – 402.

[Yu 1997] X. Yu, J. B. Bates, G.E. Jellison, and F. X. Hart, *J. Electrochem. Soc.*, 1997, **144**, 524 – 532.

Appendix

Table A.1 Summary of the bulk contributions from EIS measurement of all cell assemblies, represented by the fitting elements of the equivalent circuit

<table>
<tr><th>Cell</th><th colspan="5">Bulk Contributions</th></tr>
<tr><th></th><th>Liquid electrolyte phase</th><th>LATP: Grain</th><th>LATP: Grain boundaries</th><th>LiPON: Grain</th><th>LiPON: Grain boundaries</th></tr>
<tr><td rowspan="2">Au-LATP</td><td>---</td><td colspan="2">R_s</td><td>---</td><td>---</td></tr>
<tr><td>---</td><td>---</td><td>R_1//CPE_1</td><td>---</td><td>---</td></tr>
<tr><td rowspan="2">Liquid-LATP</td><td colspan="3">R_s</td><td>---</td><td>---</td></tr>
<tr><td>---</td><td>R_1//CPE_1</td><td></td><td></td><td></td></tr>
<tr><td>Li vs Li</td><td>R_s</td><td>---</td><td>---</td><td>---</td><td>---</td></tr>
<tr><td rowspan="2">Protective layer</td><td colspan="2">R_s</td><td></td><td>R_s</td><td></td></tr>
<tr><td>---</td><td>---</td><td>R_1//CPE_1</td><td>---</td><td>R_1//CPE_1</td></tr>
<tr><td>Standard SC vs Li</td><td>R_s</td><td>---</td><td>---</td><td>---</td><td>---</td></tr>
<tr><td>Hybrid SC vs. Li</td><td colspan="2">R_s</td><td>R_1//CPE_1</td><td>R_s</td><td>R_1//CPE_1</td></tr>
<tr><td>SC vs. SC</td><td>---</td><td>---</td><td>---</td><td>---</td><td>---</td></tr>
</table>

Table A.2 Summary of the interface contributions from EIS measurement of all cell assemblies, represented by the fitting elements of the equivalent circuit

Cell	Interface Contributions				
	Li metal foil| Liquid electrolyte	Liquid electrolyte| LATP	LATP| LiPON	LiPON| Li metal	Liquid electrolyte| C-black
Au-LATP	---	---	---	---	---
Liquid-LATP	---	$R_2//CPE_2$	---	---	---
Li vs Li	$R_1//CPE_1$	---	---	---	---
Protective layer	$R_2//CPE_2$				---
Standard SC vs Li	$R_1//CPE_1$	---	---	---	$R_2//CPE_2$
Hybrid SC vs. Li	$R_1//CPE_1$				$R_2//CPE_2$
SC vs. SC	---	---	---	---	---

Table A.3 Summary of the blocking-interface contributions from EIS measurement of all cell assemblies, represented by the fitting elements of the equivalent circuit

Cell	Blocking Interfaces		
	Au| LATP	Steel| Liquid electrolyte	Liquid electrolyte| C-black
Au-LATP	CPE_2	---	---
Liquid-LATP	---	CPE_3	---
Li vs Li	---	---	---
Protective layer	---	---	---
Standard SC vs Li	---	---	---
Hybrid SC vs. Li after assembly	---	---	CPE_3
SC vs. SC	---	---	---

Table A.4 Summary of the diffusion contributions from EIS measurement of all cell assemblies, represented by the fitting elements of the equivalent circuit

Cell	Diffusion of polysulfides in the liquid electrolyte phase
Au-LATP	---
Liquid-LATP	---
Li vs Li	---
Protective layer	---
Standard SC vs Li	CPE_3
Hybrid SC vs. Li after the 1st charge	CPE_3
SC vs. SC	---